Star Formation in Clumpy, Interacting Galaxies

by

Katherine Myers

A THESIS SUBMITTED IN PARTIAL FULFILMENT OF
THE REQUIREMENTS FOR THE DEGREE OF

BACHELOR OF SCIENCE

in

Honours Astrophysics

(Department of Astronomy and Physics, Dr. Marcin Sawicki supervising faculty,
with Dr. Vicente Estrada-Carpenter)

.....

.....

.....

.....

.....

SAINT MARY'S UNIVERSITY

April 22, 2024

Abstract

Star Formation in Clumpy, Interacting Galaxies

by *Katherine Myers*

submitted on April 22, 2024:

Galaxy mergers are one of the most important processes in the universe - they are a method of galaxy growth and mass assembly, and also the cause of internal dynamic changes in galaxies including star formation and quenching. In this thesis we examine two populations of interacting galaxies with data from the James Webb and Hubble space telescopes, and two equivalent populations of isolated galaxies, in order to examine the star formation trends, but also the presence of star-forming clumps of material in galactic disks. The analysis on star formation is based on a combination of the results from broadband spectral energy distribution (SED) fitting of imaging data, and Hα emission line maps from 2D slitless grism spectroscopy. We present the development and applications of a 'clump' detection algorithm, and examine the clumpiness of all galaxies in both samples. We find that within a narrow mass range (between $10^9 - 10^{10} M\odot$) that interacting galaxies are higher in both star formation rate and number of clumps, supporting common theories that mergers induce star formation, and that they are potentially tied to clump formation. Using emission line maps and the results of spectral energy distribution (SED) fitting, we investigate the clump contributions to galaxy star

formation rate (SFR), comparing these results to the literature and use their behaviour to explain overall star formation and clump trends in mergers.

Contents

List of Figures

List of Tables

Chapter 1

INTRODUCTION

Galaxies are some of the biggest building blocks in the makeup of our Universe. They are large accumulations of gravitationally-bound material, including stars, gas, dust, and dark matter. Studying the mechanisms in which they form, evolve, and interact with their environments is the key to understanding the composition and physical processes that govern the entire Universe and everything in it. Galaxies exist in the mass range of $10^{6-12} M_{\odot}$, and have been observed from redshift $z_{spec} = 0 - 13.2$ (Curtis-Lake et al., 2023). They can have many different morphologies, stellar populations, and evolutionary pathways. Galaxies are the hosts for star-forming regions, and thus are responsible for most of the stellar light we can observe, making them important laboratories for studying diverse astronomical phenomena.

Most galaxies fall into one of two major classes: star-forming and blue, or quiescent and red (Strateva et al., 2001). "Red and dead" (Merlin et al., 2019) galaxies have snuffed out (quenched) all of their star formation and are typically home to older stellar populations as a result. The various segments of galaxies, including dust and gas disks, central bulges, and stellar halos, undergo different evolutionary changes, and observing their chemical signatures can show us what they are made of and how they came to be. Most galaxies have a bulge, a dense region at their center containing

stars of varying ages (Jones et al., 2015) and at the very core a super massive black hole (SMBH) with $M_{SMBH} > 10^6 M_\odot$ (Kormendy and Richstone (1995); Kormendy and Ho (2013)) - though not all of the central SMBHs are actively accreting material. Some galaxies have disks, planes of orderly-orbiting clouds of gas and dust, that often take the form of star-forming spiral arms like those of our own Milky Way. Star formation in these disks is caused by the condensation of their cold molecular and atomic gas. In the disks of galaxies, we sometimes see irregular structure: bright, compact blobs called clumps (Elmegreen and Elmegreen, 2005). The origin of these clumps remains largely unknown. Tracking the properties of clumps and examining how they behave in different circumstances can illuminate how they are formed, their chemical makeup, and what impact they have on galaxy evolution.

1.1 Mergers and galaxy interactions

The currently favoured cosmological model, ΛCDM (described in Condon and Matthews (2018)), acknowledges that galaxies grow over cosmic time by hierarchical "bottom-up" growth (Jones et al., 2015). This means that a process of successive major mergers with other larger and larger galaxies (called a "merger tree" (Figure 1.2)) is the main mechanism for galaxies to quickly accumulate mass over cosmic time. The study of galaxy mergers (hereon just called mergers or interactions [1]) is crucial for the understanding of galactic and Universe evolution.

[1] In this thesis, the terms merger and interaction are used interchangeably. Typically, a merger is the most intense form of an interaction, where the galaxies actually combine as one. Interaction is more of an umbrella term for any two (or more) galaxies that are gravitationally affecting one another. However, the method of determining whether an interaction will also become a merger is nontrivial, therefore they will be unified in this presentation.

Figure 1.1: A nearby galay merger captured by the MIRI and NIRCam instruments on the JWST: II ZW 96. Source: ESA/Webb

Mergers (like that in Figure 1.1) can be divided in two sub classes depending on the masses of the participating galaxies, and the two classes have different effects. Minor mergers are between galaxies of dissimilar mass - in this scenario, the smaller galaxy is completely tidally disrupted and accreted by the larger galaxy which remains largely undisturbed. If either galaxy has gas, this can cause a burst of star formation that is concentrated in the outskirts of the surviving larger galaxy (Williams et al., 2024) as that gas is compressed. Major mergers are between galaxies of comparable mass (defined in this work as a maximum mass ratio of 1:4). Occasionally, major mergers are determined by the relative brightness of the two galaxies (Woods and Geller, 2007), or by a different mass threshold (1:3 in Williams et al. (2024), 1:2 in

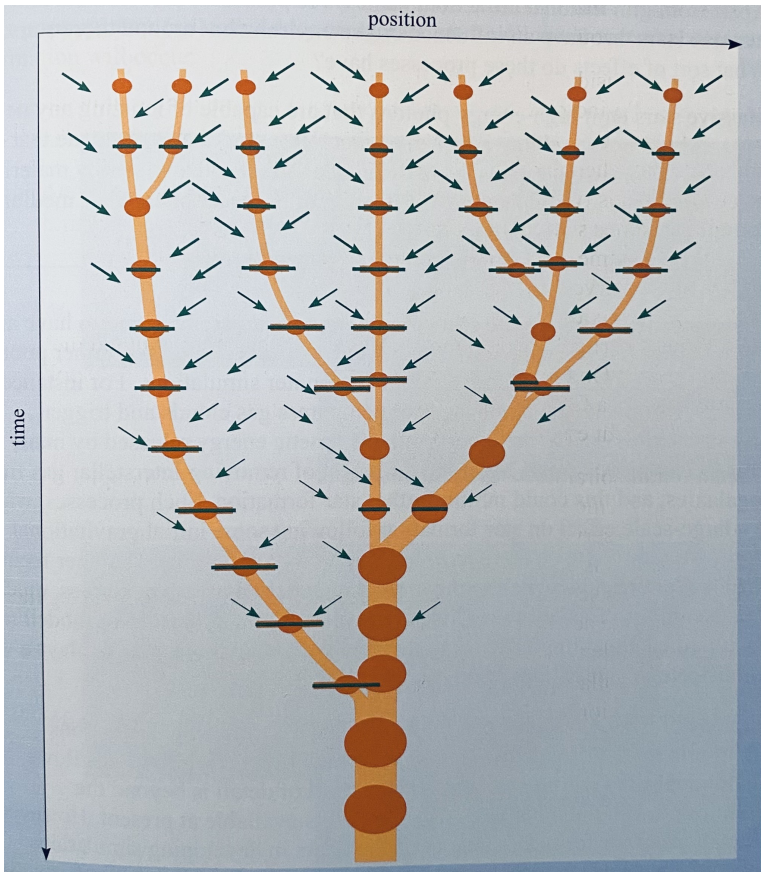

Figure 1.2: Figure 2.32 from Jones et al. (2015) that shows the cycle within which merging disk galaxies experience disk disruption and form progressively larger merged elliptical galaxies.

Ellison et al. (2008)). In this case, both galaxies' disks are disrupted and they eventually completely merge to form a large elliptical galaxy. Again, if there is gas present, this can cause a burst of star formation, but that star formation is more centrally concentrated than in minor mergers. In this project, only major mergers are studied.

Previous studies of mergers including Kennicutt et al. (1987); Ellison et al. (2008); Shah et al. (2022) and others find that galaxies in pairs exhibit stronger Hα emission than non-interacting galaxies, showing that overall star formation rates (SFR) increase in merging systems. The star formation in these galaxies is disk-dominated. It has also been shown, however, that star formation in interacting systems is highly variable, and that each galaxy behaves uniquely, likely based on case-by-case differences in their interaction environments (Kennicutt et al., 1987). This can result in some interacting galaxies experiencing no noticeable change to their SFR. It has also been suggested that because the timescale of a gravitational interaction is much longer than that of the observed Hα emission (Section 1.2), that an interacting galaxy will exhibit a range of behaviours as the interaction progresses. Ellison et al. (2008) considers galaxies to be interacting when they are within 80 kiloparsecs (kpc) of physical separation, but finds that interacting-related effects become most noticeable when the galaxies are within 30 kpc. These effects include visible tidal disruption, and augmented star formation that happens as a result of gas being compressed by the forces of the interactions.

1.2 Star formation

Aside from mergers, galaxies grow by forming stars. Stars are formed from condensing clouds of molecular and atomic gas (Inutsuka et al., 2015), which often happens in the intragalactic medium. Star formation emits specific signatures that appear in the observed spectra of the star-forming regions. These signatures are related to the variations of star masses that are formed, constrained by the initial mass function. The most massive stars (types O, B) burn through their material very quickly, and they live and die within ∼10 Myrs. Massive stars burn very hot, and the UV light from the hottest OB stars is capable of ionising the surrounding neutral hydrogen (HI) medium. The recombination of ionised hydrogen with the liberated electrons produces the Balmer series emission lines as electrons cascade down in energy levels. Hydrogen α (Hα) is the emission line resulting from the $n = 3$ to $n = 2$ transition, and it is very bright in star forming regions/galaxies, where these most massive stars are newly formed. Observing Hα emission indicates a region of "current" or instantaneous star formation, as opposed to the longer time scales of star formation that is observed with UV emission. This is advantageous for the time-dependent merger situations I am observing, as we are able to track changes in star formation on a shorter timescale.

Hα luminosity can easily be derived from the observed Hα flux, if the distance to the galaxy is known. In my work, I am analysing galaxies with known redshifts, either photometric (Brammer et al., 2010), spectroscopic, or both[2]. Using the redshift we

[2]Throughout this thesis, the redshift values reported will always be using the spectroscopic redshift if it is available, and if not, the photometric redshift. The redshifts for all galaxies are reported in Appendix B.

are able to find the comoving line-of-sight distance to the object ($dist[Mpc]$ (Astropy Collaboration, 2022)), allowing me to use the relation given by Kennicutt (1998) to determine the SFR of galaxies or clumps from their incident Hα flux (Equation 1.1).

$$SFR_{H\alpha}[M_{\odot}yr^{-1}] = F_{incident,H\alpha}[ergs/s/cm^2] \cdot (7.9 * 10^{-42}) \cdot dist[Mpc]^2 \cdot 4\pi \quad (1.1)$$

Star formation trends change in galaxies along the Hubble sequence (Kennicutt et al., 1987). Bluer galaxies (spirals, disk galaxies) have heightened star formation and more visible nebular emission. On the other hand, galaxies with no active star formation are called quiescent ("dead") galaxies, and elliptical galaxies are substantially more likely to be quiescent, and void of molecular gas, the fuel for star formation.

In addition to Hα, UV light is also a tracer of star formation. High-energy UV photons come from hot OB stars with lifetimes on the order of $\sim$100 Myrs. This makes UV light a tracer of longer-timescale star formation. It is possible to use a ration of Hα to UV light to trace rapid increases in star formation called bursts (Asada et al., 2024; Iglesias-Páramo et al., 2004; Guo et al., 2016); if the 'recent' star formation (Hα flux) is higher than the 'sustained' star formation (UV flux), the galaxy is increasing in star formation, and for the opposite relationship the galaxy is experiencing an episode of quenching star formation. This thesis derives the Hα SFR from grism emission line maps, but UV star formation rate is also used for galaxies without NIRISS data by performing SED fitting on broadband images. This process is outlined in Section 2.3.1.

1.2.1 DUST

Galaxy photons are susceptible to dust extinction; they will get scattered, or absorbed and re-emitted at longer wavelengths by dust particles in the interstellar medium (Kennicutt et al. (1987), Calzetti (2001)). This results in an overall reddening of the galaxy's light, as bluer photons have a higher cross section of interaction and are more likely to be lost to extinction (Divan, 1971). In order to restore the intrinsic flux from the Hα line from what we observe, we will perform a dust correction using the Calzetti dust law (Calzetti, 2001). This takes into account the distance to the galaxy (derived from redshift), and the galaxy's dust content, and raises the observed flux back to its pre-attenuation levels. Calculations are described in section 4.3. The dust content of the galaxies in this thesis is derived from spectral energy distribution (SED) fitting, as described in Section 2.3.1.

1.3 CLUMPS

Clumps are bright, discrete, and dense segments of galactic disks that are believed to be regions of heightened star formation (Elmegreen and Elmegreen, 2005). Clumps have most often been identified by their UV brightness (Elmegreen and Elmegreen, 2005) as they are in this thesis, which supports the theory of clumps as star-forming regions. In galaxies that host clumps, it has been found by Guo et al. (2015) that each clump contains on average $\sim$8% of the UV light of their host galaxy and $\sim$4-10% of the star formation rate in star-forming galaxies, has a mass between $10^{7-9}M_{\odot}$, and

is about ∼1kpc in size. Galaxies beyond $z = 0.5$ are more likely to be clumpy than galaxies below $z = 0.5$, and the fraction of clumpy galaxies also depends on galaxy mass; higher mass ($log_{10}(M_*/M_\odot) > 10.6$), lower redshift galaxies have the lowest clumpiness fraction at just 15% (Guo et al., 2015). For a galaxy to be considered clumpy according to Guo et al. (2015), it must contain 'at least one off-center clump', a definition that has also been adopted in this thesis.

The origin of clumps is not well understood. Guo et al. (2015) explain their origins may be a result of minor merger-induced disk instabilities that condense into clumps, but admit that their observationally-determined clump parameters do not require clumps to have been formed inside or by their current host galaxy.

1.4 This thesis

In this thesis, I will be using data from the James Webb Space Telescope's (Gardner et al., 2023) NIRCam and NIRISS instruments, as well as archival Hubble data to examine the effect of galaxy interactions on star formation in clumps. We will be testing the popular theory that mergers augment star formation by comparing star formation rates between a set of interacting galaxies with mass and redshift matched to isolated (non-interacting) control galaxies. In addition to testing overall galaxy star formation, we will be inspecting the star formation rate of clumps within interacting/isolated galaxies - this will show if clumps are experiencing more or less of a

star formation burst than the galactic disk. In addition, measuring the amount of detected clumps in interactions and mergers could potentially indicate whether clump formation could be merger-induced, if interacting galaxies tend to be more clumpy.

Chapter 2

DATA

This work was completed using both spectroscopy and imaging of galaxies in the cluster field of MACS0417, and imaging of galaxies in the cluster field MACS1423. This combination of techniques allowed for a more diverse and complete analysis of star formation and clumps in interacting systems.

2.1 THE MACS0417 AND MACS1423 CLUSTER FIELDS

Galaxy clusters are dense associations of gravitationally bound galaxies, and are ideal observational targets for studying galaxy evolution due to a phenomenon called gravitational lensing. This is where massive foreground intracluster masses bend the path of light from background sources and act as a magnifying glass for high-redshift sources that would otherwise be too faint to observe in detail (Willott et al., 2022).

The galaxies in this work are from the CANUCS clusters MACS J0417.5–1154 (known informally as MACS0417) (RA, Dec = 04h:17m:35.1s, -11^o:54m:38s, $z_{cluster}$ = 0.443) and MACS J1423.8+2404 (MACS1423) (RA, Dec = 14h:23m:47.8s, $+24^o$:04m:40s,

$z_{cluster} = 0.545$). The contaminating light from brightest cluster galaxies (BCGs) can be problematic when imaging in a cluster field. In the MACS0417 and MACS1423 images, the BCGs have been removed to facilitate studying the gravitationally-lensed background galaxies (Martis et al., 2024; Estrada-Carpenter et al., 2023).

2.2 NIRISS and NIRCam: The James Webb Space Telescope

This work was completed as part of the CAnadian NIRISS Unbiased Cluster Survey (CANUCS) collaboration. CANUCS is a James Webb Space Telescope Guaranteed Time Observation program, with a combined 200 hours of observations from five gravitationally-lensed galaxy cluster fields: MACS0417 and MACS1423 (section 2.1), MACS0416, MACS1149, and Abell 370. Each cluster field was imaged by the Near InfraRed Imager and Slitless Spectrograph instrument (NIRISS) (Doyon et al., 2023) operating in Wide Field Slitless Spectrscopy (WFSS) mode, with two orthogonal grisms in three filters: F115, F150, and F200 (Willott et al., 2022). Each NIRISS filter has an observation time of 2.3ks (Asada et al., 2024). These NIRISS observations are performed in parallel with NIRCam images of the cluster field. The NIRCam observations are in 8 wide and medium filters: F090W, F115W, F150W, F200W, F277W, F356W, F410M, and F444W (Willott et al., 2022), each with an exposure time of 6.4ks (Asada et al., 2024). Figure 2.1 shows the instrument configurations on each cluster field, and Figure 2.2 shows the wavelength coverage of each filter. The

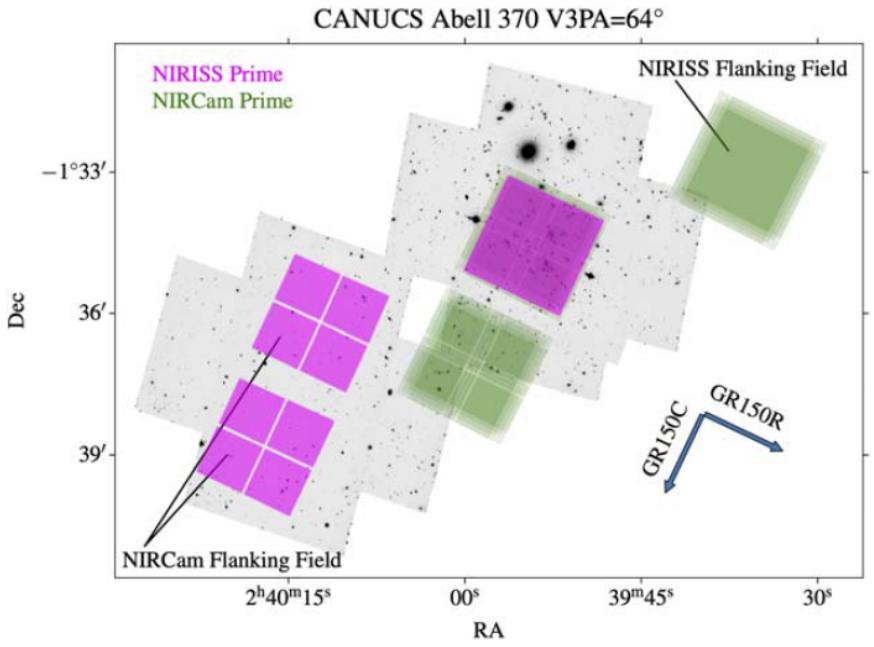

Figure 2.1: The layout of the CANUCS observations with NIRCam and NIRISS for Abell 370 (source: Willott et al. (2022)). The configuration is the same for all cluster fields, and all of my work is done using the main cluster field (NIRISS and NIRCam), and the adjacent cluster field (NIRCam only) in MACS0417 and MACS1423.

portion of MACS0417 with NIRISS data is a 2.2" × 2.2" field of view (Doyon et al., 2023) targeting the cluster center.

Studies of spatially resolved star formation properties in galaxies around cosmic noon have been picking up so far in the era of JWST/NIRISS (Estrada-Carpenter et al., 2023; Matharu et al., 2023). The JWST as a Near Infrared telescope presents the opportunity to study spatially-resolved Hα star formation rate (SFR) at higher redshifts than was previously possible.

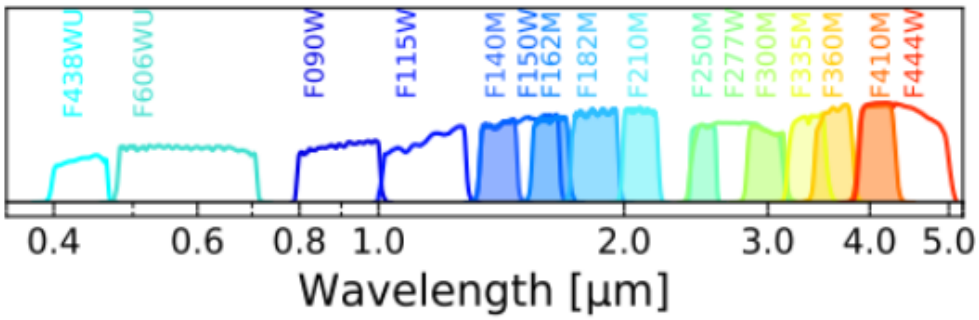

Figure 2.2: The filters used by CANUCS. Adapted from Figure 2.2 in Asada et al. (2024).

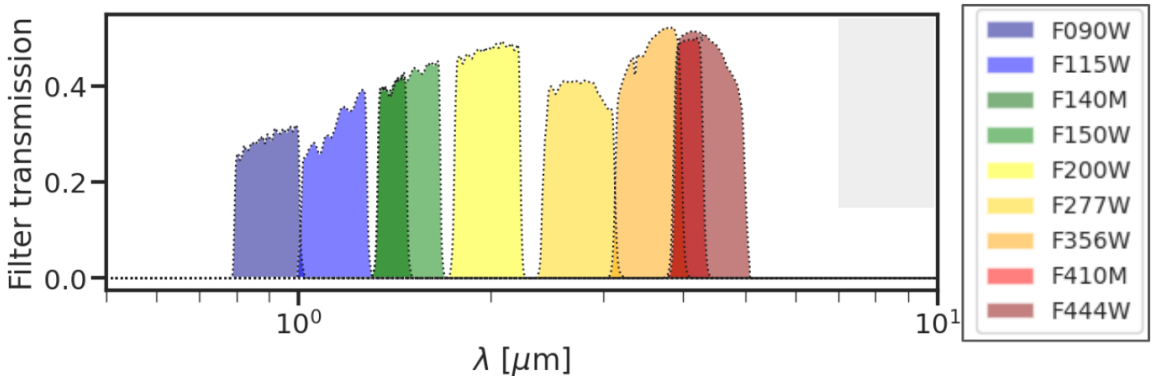

Figure 2.3: The NIRCam filter available in the CANUCS dataset for MACS0417. F115, 150, and 200 are also includes in the NIRISS spectra. Source: Shannon MacFarland (CANUCS)

2.3 NIRCam and HST imaging

During the CANUCS GTO program, NIRCam imaging was taken of the cluster field and two adjacent 'flanking' fields. The flanking fields are imaged only with the medium bands (F140M, F162M, F182M, F210M, F250M, F300M, F335M, F360M, and F410M) (Asada et al., 2024), while the central cluster field uses all the bands listed above. In this work, images are point spread function (PSF) smoothed to the F444W images (Sarrough et al. (in prep.)), and the contaminating light from brightest cluster galaxies have been removed to facilitate studying the gravitationally-lensed background galaxies (Martis et al., 2024).

For every galaxy in the (smaller) NIRISS field, there is coverage both from CANUCS NIRCam imaging, and the Reionization Lensing Cluster Survey (RELICS), a 2016/17 Hubble Space Telescope (HST) program (HST-GO-16667), P.I. Bradač (Mahler et al., 2019), or other archival Hubble Space Telescope (HST) observations. The availability of archival Hubble data for this work made it possible to analyse the galaxies and clumps in additional detail. From HST, we have the filters F435W, F606W, and F814W. Specifically, the F606W filter in HST was used to view the galaxies in the UV band in order to identify clumps, a method described in depth in section 4.1.

2.3.1 NIRCam Spectral Energy Distribution Fitting

While this thesis has focused on the star-forming clumps, there have been more in-depth analyses of the CANUCS fields done using only photometry from the 16

NIRCam filters. In this thesis, I make frequent use of the results obtained by a CANUCS collaborator using broadband photometry, including mass, dust, and star formation rate maps of each galaxy in my samples (MacFarland et al. (in prep.)). The broadbands in the CANUCS data are F090, F115, F150, F277, and F444. These galaxy property maps were obtained by performing pixel-by-pixel Spectral Energy Distribution (SED) Fitting with `dense_basis` (Iyer et al., 2019). SED fitting in this case is the process of fitting an observed galactic spectrum to a modelled one; this is done by creating an initial set of modelling parameters called priors that are based on the known (or assumed) properties of the galaxy. These priors include the stellar initial mass function, star formation history, dust content, as well as stellar population synthesis parameters such as the spectra and Herzsprung-Russel isochrones for different stellar types. These SED inputs are nicely summarised in Figure 1 of Conroy (2013).

With `dense_basis`, non-parametric star formation histories permit more flexibility when interpreting the observed SED. This includes allowing for the possibility that a galaxy has experienced multiple star-forming bursts during its lifetime. `dense_basis` SED fitting also incorporates several other physical parameters, such as inter-galactic medium absorption, nebular emission lines, and chemical enrichment (Iyer et al., 2019). During the SED fit, the observed spectrum is tested against many possible model spectra, and returns that with the best agreement (Conroy, 2013). The best-agreeing spectrum also comes with physical parameters that can explain its shapes and features, including pixel mass, star formation rate, dust content, and more. Each

pixel in the maps is created from the output of the combined SED fit done across all broadband images.

2.4 GRISM SPECTROSCOPY

The foundation for the second part of the analysis in this thesis, Hα star formation and burstiness in galaxies and clumps in merger scenarios, is based on the availability of 2D grism spectra from NIRISS. In the raw grism data (Figure 2.4), the spectrum is the smearing of a spatial image of the galaxy across the wavelength axis (x axis). NIRISS's 0.04"/pixel spatial resolution allows for detailed images showing intricate intragalactic features. When the galaxy is bright due to an emission feature (such as Hα, OIII, or any other), a picture of the galaxy appears at that wavelength in the spectra. From these spectra, we are able to extract images of the galaxy at particular emission lines, and see the spatial distribution of emission lines. This feature allows for the study of individual galaxy components like clumps or the bulge, as we can resolve where specific emission features originate. The method of extracting emission lines from grism spectra that is used in this work is described in section 4.2.

One of the substantial advantages of wide field slitless spectroscopy is the ability to take simultaneous spectra for hundreds of objects. Without needing long exposure times for each individual object, NIRISS is instead able to produce grism spectra for the entire cluster field in one observing session of 9.7ks (Willott et al., 2022). However, grism spectroscopy suffers from drawbacks including low spectral resolution (47Å/pix), smearing between objects, and self-contamination (van Dokkum et al.,

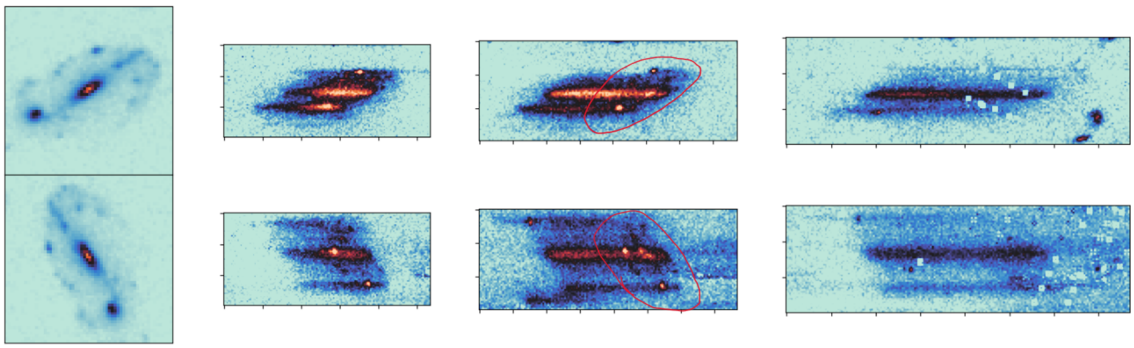

Figure 2.4: The two perpendicular orientations of the raw 2D grism spectra. The leftmost panel is a direct image of the galaxy, and the subsequent three panels are the grism filters F115, F150, and F200. An emission line is shown by the red outline in the F150 filter, where bright Hα emission lights up the shape of the galaxy.

2011; Estrada-Carpenter et al., 2019). Each galaxy and clump has a spatial size of at least five pixels in diameter. As the image of the galaxy is smeared over wavelength, neighbouring wavelengths will contain an overlap from the one beside it, owing to the galaxy's non-point source like nature. Figure 2.5 demonstrates how this results in self-contamination in the grism spectrum.

Similar contamination can happen from neighbouring objects along the path of the smearing - especially relevant in the study of mergers where we are deliberately targeting objects with spatially close companions. This contamination can make associating spectral features with a particular galaxy more complicated. Having the second grism orientation is usually sufficient to solve this issue, as the object is likely to only be a contaminant in one of the two orientations.

The spectral resolution of NIRISS is 47Å per pixel, meaning that emission lines

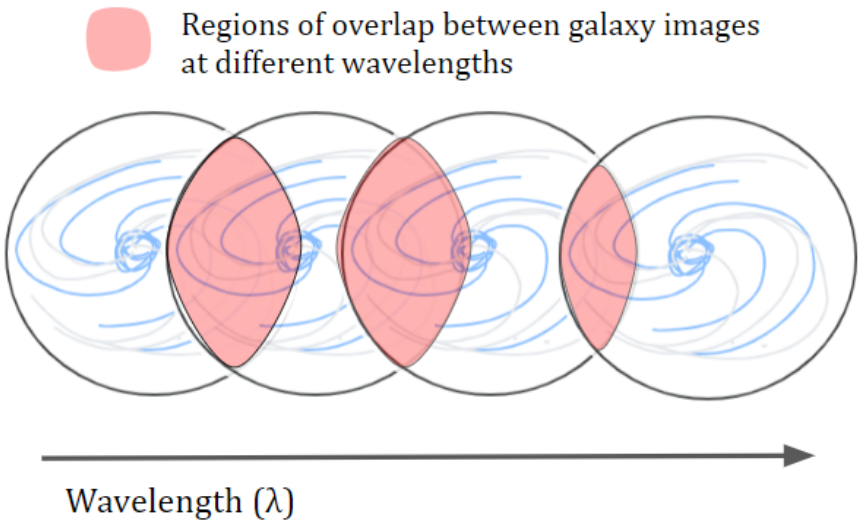

Figure 2.5: The self-contamination of grism spectra. When smearing in wavelength, the image of the galaxy extends into neighbouring wavelengths. Shown here in discrete intervals, this phenomenon happens continuously along the spectrum.

within separation of $\Delta\lambda < 47$Å will be unresolvable in the grism spectra. This includes notably the Hα line (6563Å) and the NII lines (6548Å and 6584Å). In the spectra used in this thesis, all of the Hα emission line maps will also contain flux from the NII line, but this fact is accounted for when Hα flux is converted to SFR.

Chapter 3

Sample selection

In this thesis, we aim to understand star-forming clumps in interacting galaxies, and compare merging galaxies to isolated, non-merging galaxies. We do so by defining separate samples: a the sample of interacting galaxies (henceforth the "sample" galaxies, or the "photometric" or "study" or "interacting" sample), and a mass and redshift equivalent sample of non-interacting galaxies (henceforth "controls" or "isolated" galaxies, or control sample). As this thesis covers galaxies across two cluster fields, MACS0417 and MACS1423, each cluster field has its own interacting sample and control sample, identified by the criteria described below. We are also investigating both photometric and grism spectroscopic properties of galaxies in MACS0417 specifically, so this galaxy cluster also has a subset of its interacting galaxies which appear in the NIRISS field and have spectral data - this subset is referred to as the "spectroscopic sample".

The details of the final samples are outlined below (Table 3; P for photometric sample, S for spectroscopic sample, C for the corresponding control sample), and the comparisons between the controls and the interacting galaxies can be see in Figures 3.1 to 3.3.

Table 3.1: Comparing the Mean Properties of the Samples

	# Gals	M range	mean logM	mean z
MACS0417 P	24	8.57-11.44	9.8362	1.1906
MACS0417 PC	41	8.51-11.21	9.8326	1.1610
MACS0417 S	9	8.78-11.44	9.8082	1.2944
MACS0417 SC	9	8.51-11.03	9.7294	1.3190
MACS1423 P	71	6.76-11.32	9.0063	0.8622
MACS1423 PC	71	6.57-11.65	9.1162	0.9074

In order to choose galaxies that are suitable for either the interacting sample or the control sample, we first are limited by the redshift range where Hα is visible with NIRISS. NIRISS's observational range is between 0.8-2.3μm (Willott et al., 2022). Hα has a rest frame wavelength of 656.43nm, and using equation 3.1, we find that the visibility range is between z=0.218-2.804. For this work, to avoid having emission lines on the edge of the grisms, all galaxies are within the redshift range of z ϵ 0.5-2.0.

$$1 + z = \frac{\lambda_{observed}}{\lambda_{emitted}} \tag{3.1}$$

For this work, galaxies brighter or equal to magnitude 24 (in the F200 filter) within the Kron aperture (Kron (1980)) were selected, as bigger/brighter galaxies are more likely to have the resolvable substructure needed to study clumps.

3.1 Identifying mergers

In order to identify galaxies that are interacting, we adopt three primary criteria modified from Ellison et al. (2008). An interacting galaxy must satisfy all of the

following:

1. Have a companion that falls within 80 kpc of distance on the sky.

2. That companion must be within $\Delta z = 0.1$ in photometric redshift, and within $\Delta z = 0.01$ in spectroscopic redshift (if it is available). This is a proxy for physical separation in the direction along the line of sight.

3. The mass ratio (see equation 3.2) must be less than 4. This is how a major merger is determined - the interacting pair must be of comparable mass, defined in this work as a maximum ratio of a factor of 4.

$$M_{frac} \leq 4 = \frac{M_{bigger}}{M_{smaller}} \tag{3.2}$$

The resulting merging candidates were visually inspected to further confirm that they were interacting. Galaxy pairs that were too diffuse, unresolved, contaminated, lacking HST data, at the edge of the field of view, or cluster members were weeded out at this stage. What remained were the 12 highest-quality interacting pairs in the MACS0417 cluster field, and 35.5 in the MACS1423 field (one pair had only one galaxy in the Hubble data field). These pairs and their controls make up the photometric samples. The RGB images of all of the pairs in MACS0417 and individual galaxy properties (mass, z) as well as the paired properties (separation, mass fraction, and Δz) can be found in Appendix C. All galaxy properties come from photometry catalogs done by collaborators (CANUCS Collaboration, in prep.). From these larger photometric samples, in MACS0417 we identified 9 galaxies in 4.5 pairs hav-

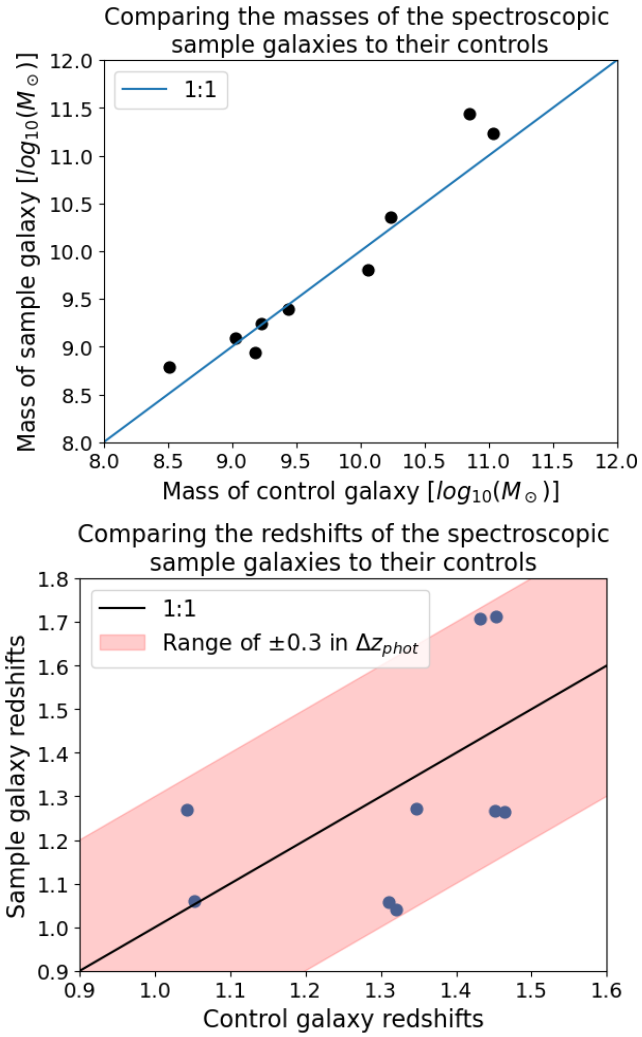

Figure 3.1: The ideal control galaxy is perfectly matched in both mass and redshift to its sample galaxy. Here is shown the spectroscopic sample (MACS0147 only) galaxies' alignment with their controls in mass and redshift.

ing NIRISS spectra, and these galaxies and their controls make up the spectroscopic sample.

3.2 IDENTIFYING CONTROLS

In accordance again to Ellison et al. (2008), the definition of a candidate control galaxy is simply any galaxy that is not interacting. In the case of my work, this is

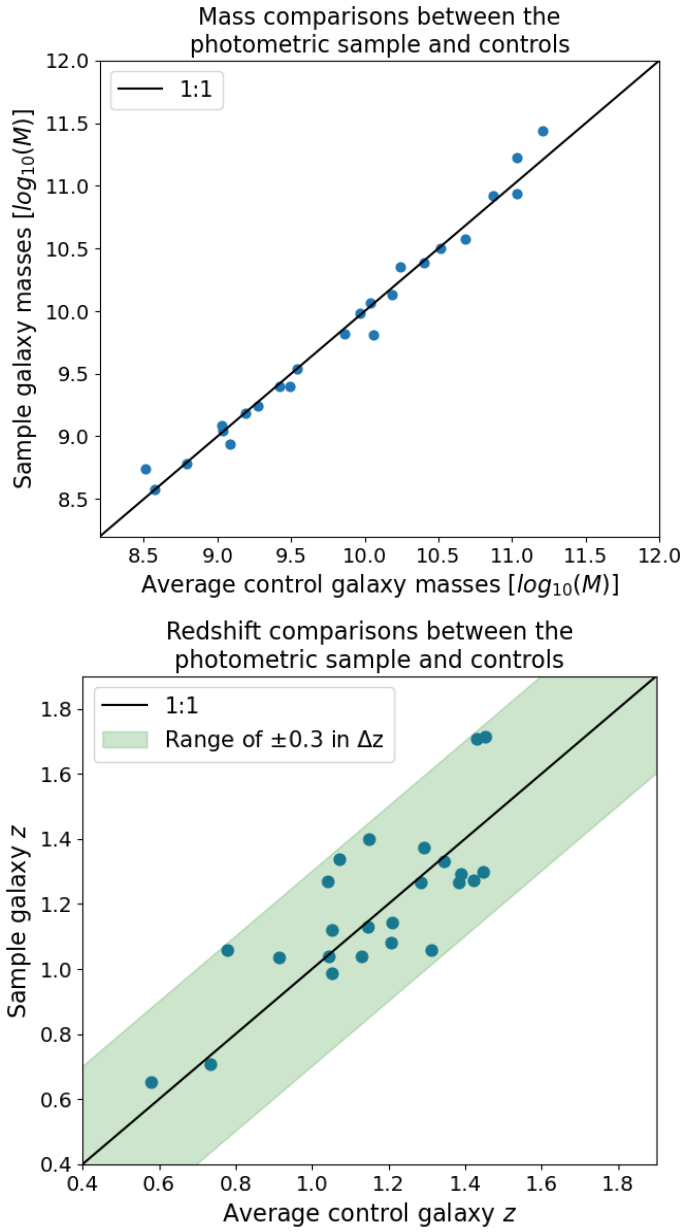

Figure 3.2: Here we see the alignment of the masses between control and photometric sample galaxies in MACS0417. Here, an averaged control galaxy is used for each photometric sample galaxy as to allow for 1:1 comparisons between sample and control galaxies.

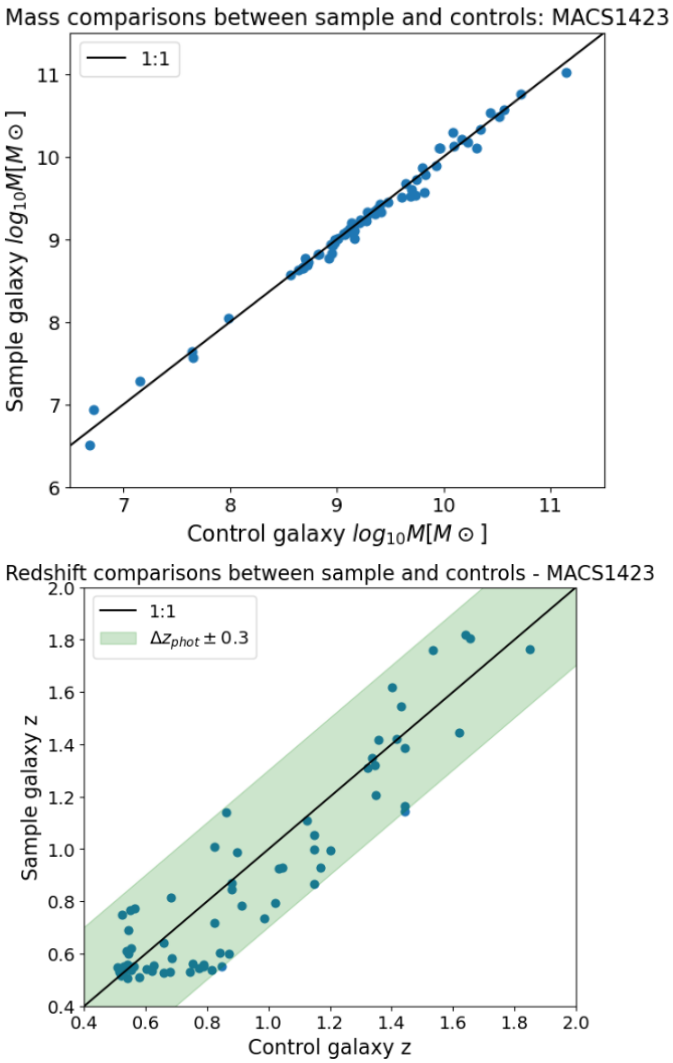

Figure 3.3: Here we see the alignment of the masses between control and photometric sample galaxies in MACS1423. Each sample galaxy is directly matched to one control galaxy allow for 1:1 comparisons.

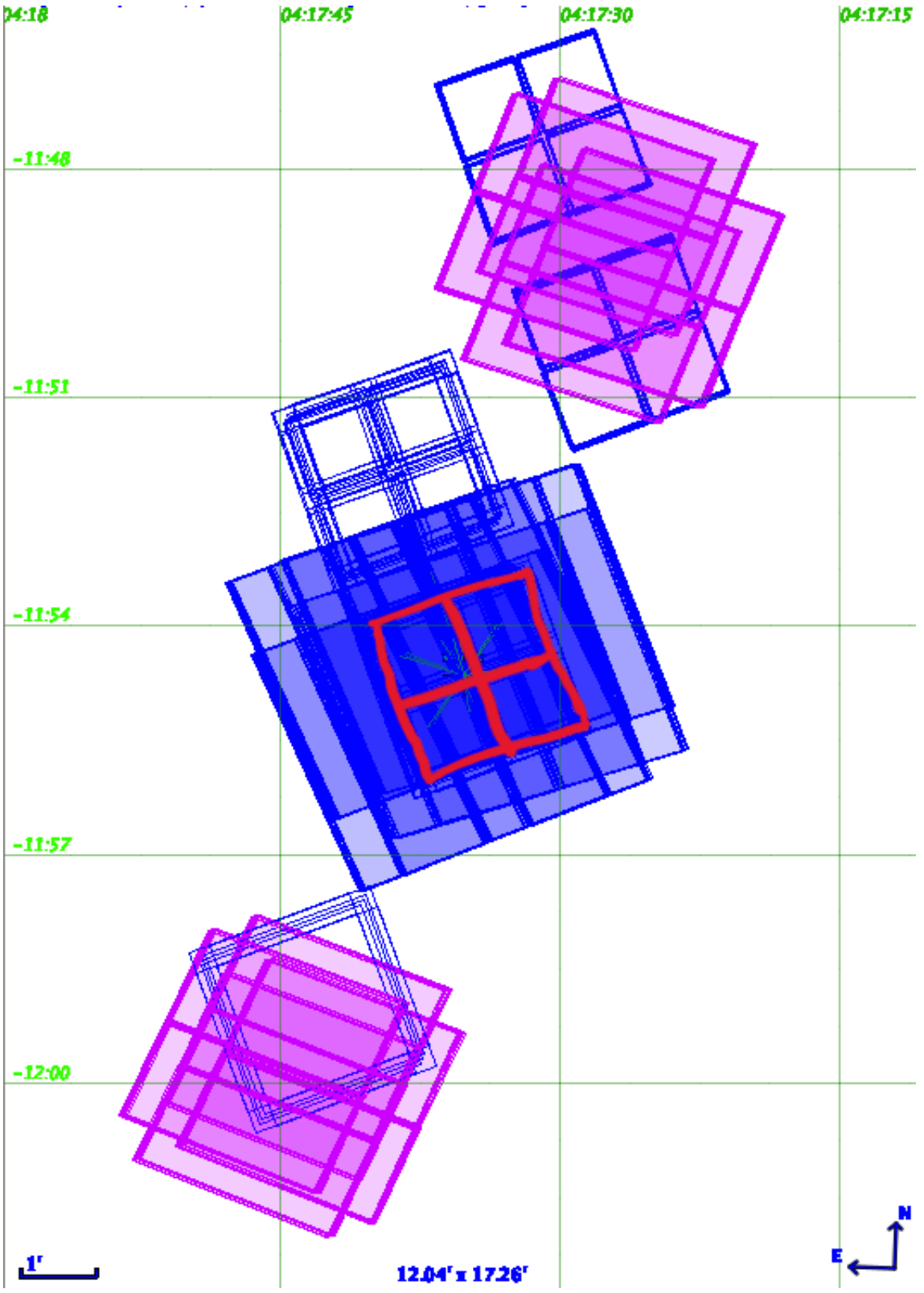

Figure 3.4: The fields of observation on MACS0417. The main cluster field is in the center of the image and the two flanking fields are above and below. Shaded blue: HST; Blue box outlines: NIRCam; Red: NIRISS (NIRCam overlapping but not visible). Source: Chris Willott (CANUCS).

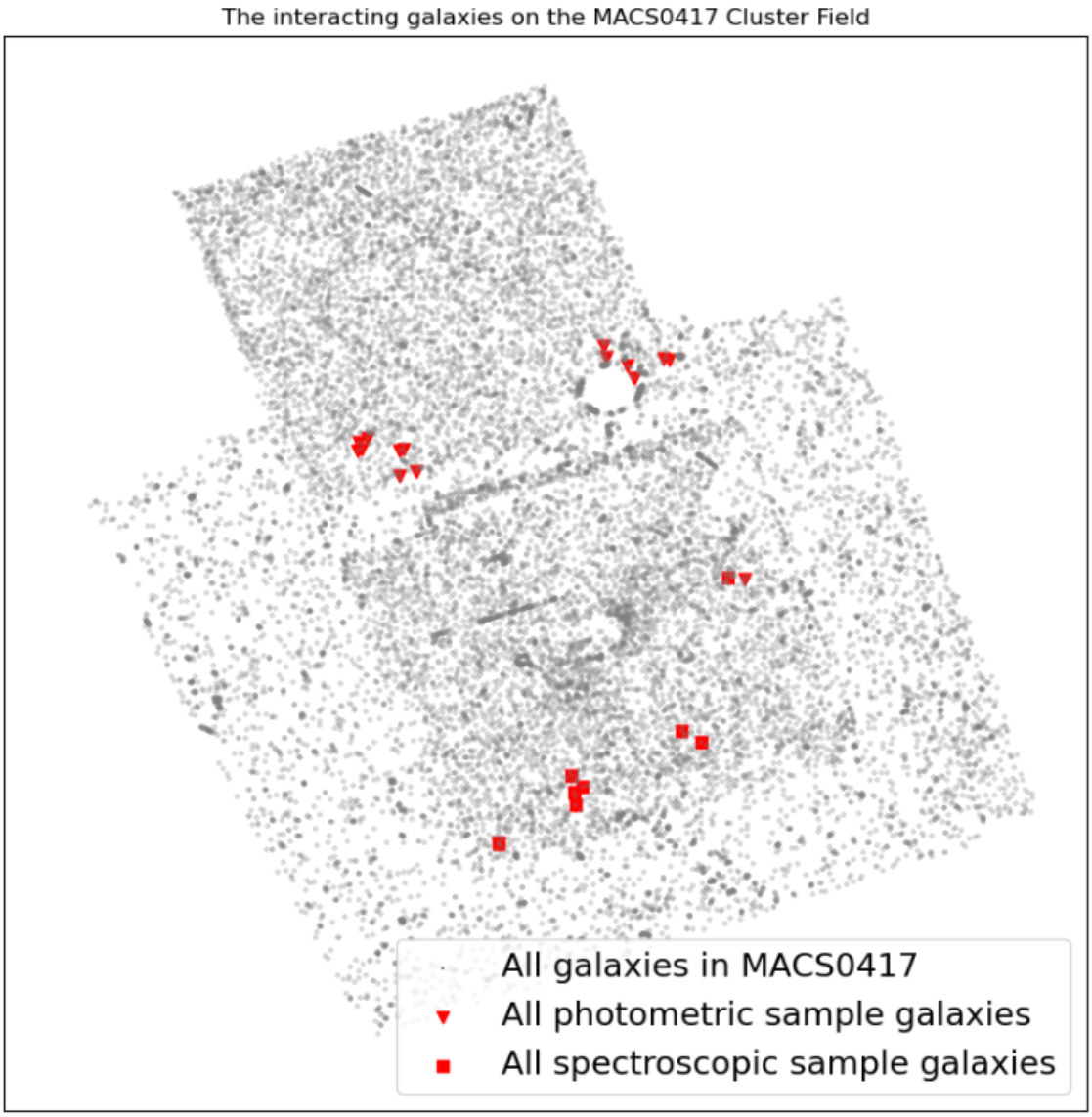

Figure 3.5: The interacting pairs in the MACS0417 cluster field.

a galaxy that has failed one of the three tests: It either has no close companions (in either redshift or spatial separation), or any nearby companions are not within a factor of 4 in mass. These properties are combined with the magnitude and redshift requirements for visibility of Hα emission.

The purpose of the control sample is to provide a frame of reference for the phenomena observed in interacting galaxies. For this to be effective, control galaxies must be similarly matched in mass and redshift to sample galaxies, as the mass and epoch will have substantial effects on the evolution mechanisms of a galaxy. The close matching in average mass and redshift between the samples and controls is shown in Table 3.1.

Each individual control galaxy is within a factor of 1.5 in mass and a difference of 0.3 in photometric redshift from its interacting sample galaxy. To improve our errors and increase sample size, in MACS0417, sample galaxies may have more than one matched control. In MACS1423, there is one control for each sample galaxy. The limits on MACS0417 spectroscopic data availability provide additional constraints on the spectroscopic control sample. Due to this, the spectroscopic control galaxies are matched 1:1 with the spectroscopic sample galaxies, while in the photometric sample, some of these same galaxies have more than one control to improve our uncertainties. Each control galaxy can only be used once per sample, and in most cases, they are matched to the interacting galaxy that is closest to them in mass.

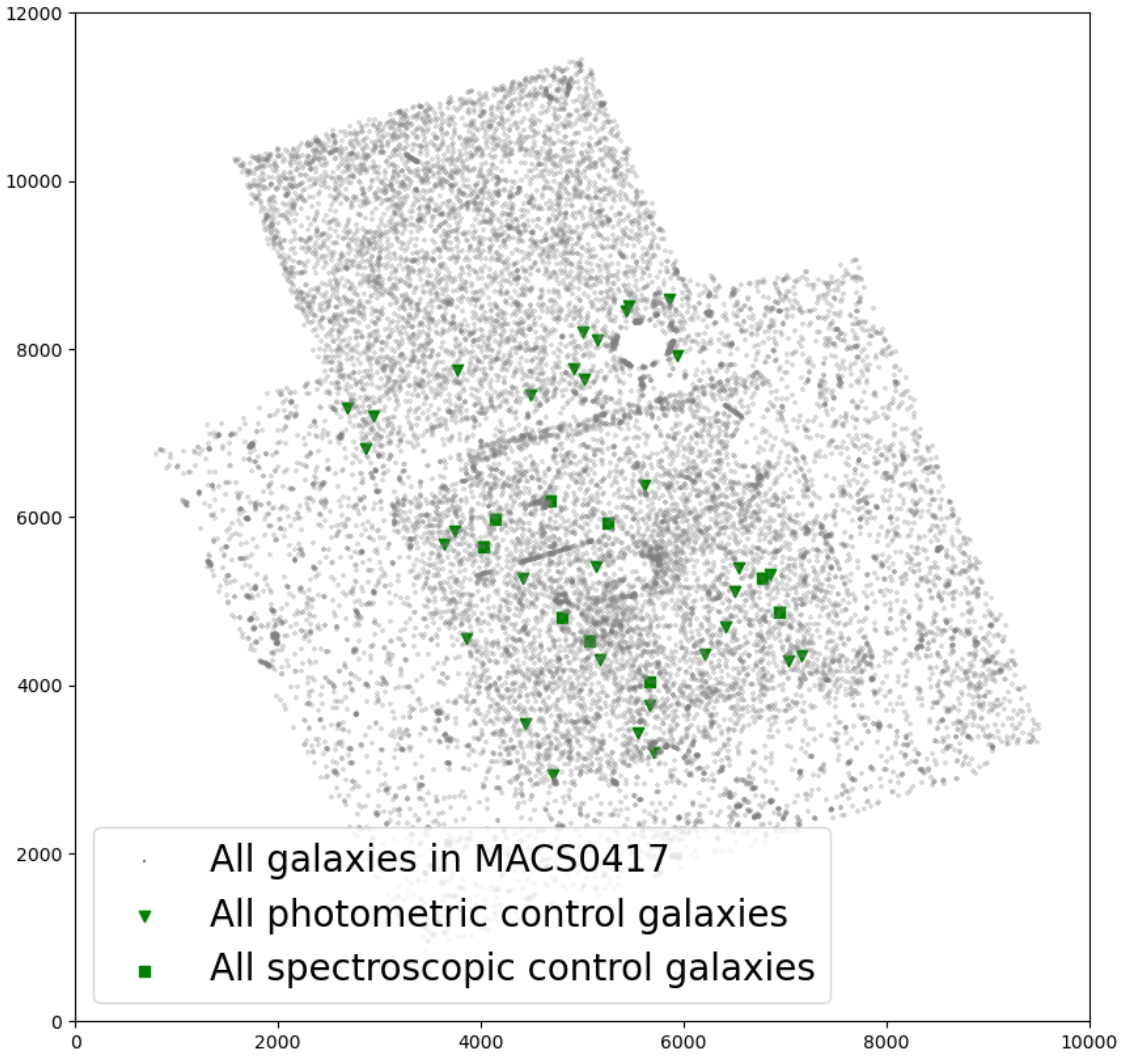

Figure 3.6: All of the control galaxies' locations in the MACS0417 cluster field.

Even galaxies that appear in both the photometric and spectroscopic samples do not necessarily have the same controls in both samples, as the photometric controls often do not have a NIRISS spectrum, even if their sample galaxy does. This necessitates restructuring of the controls that are available to assure that every galaxy has as many controls as possible, or at least one control in the spectroscopic sample case.

Chapter 4

Data analysis and methods

4.1 Pipeline for finding clumps

In order to study the star forming properties of clumps, they need to be identified and segmented out of the galaxy's disk. This process is fully automated for all galaxies studied in this thesis, and the pipeline for processing could be used to detect clumps in any image.

As clumps are believed to be bright areas of star formation (see above section 1.3), they should be brightest in the UV portion of the spectrum. This UV light is the result of hot, young, newly-formed stars that only exist in regions of star formation, due to their short lifespans (∼10 Myr). To identify clumps, we begin with photometric data from both the JWST and the HST in the MACS0417 and MACS1423 cluster fields. In all cases, the HST F606 filter is used to detect the clumps, from images in the RELICS survey (Mahler et al., 2019) and the Hubble archives. A rectangular image cutout of each galaxy is made in UV image based on the size of the galaxy's segmentation from the CANUCS photometry catalogue. All images used in this thesis have been PSF-corrected to the PSF of the F444 filter (Sarrough et al. (in prep.)).

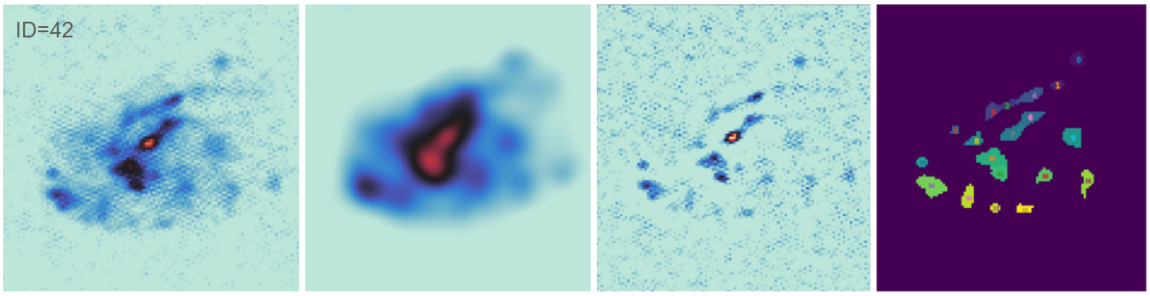

Figure 4.1: The clump detection process. Panel 1: The image of the galaxy how it appears in the HST F606 filter.
Panel 2: The image of the galaxy after it has been smoothed by a Gaussian filter.
Panel 3: Panel 1 subtract Panel 2.
Panel 4: The result of running `SExtractor` on Panel 3, all of the clumps are catalogued and segmented. The different colours indicated where the segmentations begin and end for discrete clumps.

To extract clumps, the UV cutout is first smoothed with a Gaussian kernel, whose width (σ) as a function of galaxy size is determined by the linear function $\sigma = 0.0091(size) + 2.712$ ($size$ in pixels, the average radius of the galaxy segmentation). This line was the best fit obtained from visually identifying and testing the width of Gaussian kernels to determine which gave the best result for clump visibility - based on a testing sample of 12 galaxies with various sizes. Once the image has been smoothed, the smoothed image is subtracted from the initial UV cutout, leaving behind the dense concentrations of signal/UV light. This image's (panel 3 of Figure 4.1) background is then modeled and subtracted, and a source detection algorithm called Source Extractor for Python, `SExtractor` or `sep` (Bertin and Arnouts, 1996; Barbary, 2016) is used to segment and catalogue any bright sources left in the image. The segmented regions are required to have a minimum of five pixels in order to be considered a true clump.

Once the segmentation map of the bright sources is made, the sample must be purified to truly focus on clumps embedded in the galaxy disk or halo. As the bulge of the galaxy is also often bright and compact, it will usually be identified by `SExtractor` and left in the clump segmentation map. The bulge will have a different stellar population and experience events differently than clumps in the galactic disk, so we aim to remove it from the segmentation map. This is done by using a mass map of the galaxy (created by a CANCUS collaborator from broad band SED fitting, described in Section 2.3.1). The mass map is smoothed by binning pixels in 3×3 segments, and then highest mass 9×9 pixel region is identified, the center of which is taken to be the galaxy's center of mass pixel, and the location of the bulge. Any clump segment that overlaps with this center of mass pixel is identified to be the bulge, and removed from the segmentation map (see Figure 4.2 for a visual display of the bulge removal). The remaining segmentation map is used to define the clumps throughout the analysis. These segmentation maps for the spectroscopic, photometric and control samples of MACS0417 are in Appendix F. Galaxies that do not have clumps identified from the UV image (be that the galaxy is not UV-bright or that the only signal segmented was from the bulge) will have completely flat segmentations and a 0% contributions from the clumps throughout the rest of the analysis.

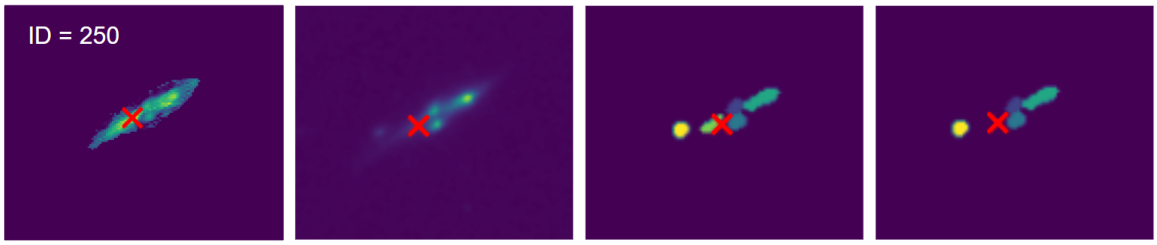

Figure 4.2: Identifying the center of mass and galaxy bulge from the clump segmentations.
Panel 1: The mass map of the galaxy from broad band photometry, with the center of mass indicated.
Panel 3: The direct image of the galaxy.
Panel 3: The center of mass overplotted on the clump segmentation map, seen to overlap with a central 'clump'.
Panel 4: The segmentation map without the bulge.

4.2 Emission line maps from grism data

In addition to identifying clumps, the other substantial processing part of this thesis revolves around extracting emission line maps and subsequently star formation rate maps. As described in section 2.4, from the raw 2D grism spectra we are able to extract snapshots of the galaxy at specific wavelengths, resulting in a map of the galaxy showing spatially-resolved emission line flux. In this thesis, the Hα emission line maps are created using `Sleuth` (described in depth in Estrada-Carpenter et al. (2023)), a newly-developed software for extracting high-quality emission line maps from grism data.

The fundamental model for emission line map extraction involves modelling the underling stellar population continuum and subtracting it from the spectrum, leaving behind excess flux from the emission lines that can be made into maps. In the standard method of emission line map creation, it has been assumed that the under-

lying stellar population that makes up the continuum is not varying throughout the galaxy. Practically, we know this not to be true (see Section 1 for a brief overview of the variations in stellar population among different segments of typical galaxies). By allowing the stellar continuum to be spatially variable, we are able to avoid over or undersubtraction of extra-continuum features such as emission line fluxes.

`Sleuth` uses both the NIRISS grism spectra and NIRCam imaging in the F115W, F150W, and F200W filters. In preparation for broadband SED fitting, the galaxies are segmented into collections of pixels with S/N $\geq$ 100 (in the F150W image) using a nearest neighbours algorithm. Each segment's SED is independently fit with six parameters: stellar metallicity, ionization, dust attenuation, specific star formation rate, nebular metallicity and time of half mass formation (non-parametric star formation histories are also used here as in section 2.3.1) (Estrada-Carpenter et al., 2023). The fit posteriors are used to create a model of the stellar continuum for that small galaxy segment, which will be used while fitting the grism spectra. At this stage, the grism data is forward-modelled (using the segmented SED fit as a prior) without the desired emission line, and then the results of this model are subtracted from the raw spectrum. The emission line flux is then left behind, creating the spatially-resolved emission line map.

Compared to the standard method, the difference is significant in emission map quality and usability. Figure 4.3 shows the same galaxy's (ID=1307) Hα map made with the standard method (panel 1), and with `Sleuth` (panel 2). In the `Sleuth`

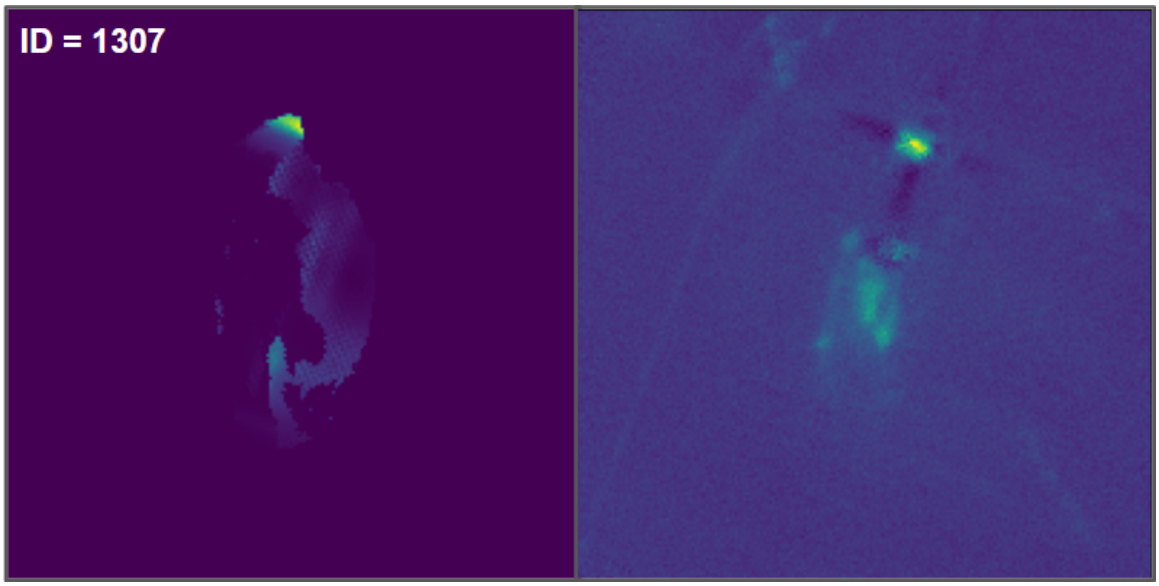

Figure 4.3: Hα emission line maps made with the standard method (left) and with `Sleuth` (right). Galaxy features are resolvable and emission features are visible when you consider a spatially varying stellar continuum. See Appendix E for the Hα emission maps for all galaxies in this thesis.

map, galaxy features are visible and the emission features can be spatially resolved. The standard model is subject to poorly-subtracted contamination and would not be usable for this clump analysis without significant extra attention.

4.3 Hα Star Formation Rate

Now with emission line maps in hand, we can convert Hα flux to star formation rate using the relation outlined in Kennicutt (1998), as described in section 1.2. Before converting to star formation rate, the Hα flux must be dust-corrected, to account for dust attenuation of high-energy photons by galactic dust along the line of sight. This correction is done pixel-by-pixel by the 1-component Calzetti dust law (Calzetti, 2001) in Equation 4.1, where A_v is the dust value at that particular pixel of the broadband

fitting dust map, and the emission line Hα flux at the same pixel is Hα_{obs}. The factor $f_{H/N}$ is used to compensate for the contamination of NII emission flux in the Hα emission line map (explained above), and has a value of $f_{H/N} = 0.828$, as 17.2% of the flux belongs to NII (Estrada-Carpenter et al., 2023).

$$H\alpha_{corrected} = H\alpha_{obs} \cdot 10^{0.4 \cdot f_{H/N} \cdot A_v} \tag{4.1}$$

The result is a value of Hα flux that has been corrected for attenuation and can now be converted to SFR using Equation 1.1. The star formation rate maps are the key ingredient to analysing interaction-induced star formation; these maps are used to calculate SFRs of entire galaxies, but also of clumps within galaxies, using the clump segmentations obtained in section 4.1 to highlight the SFR map sections that belong to clumps.

4.3.1 Galaxies without NIRISS data

For the galaxies outside of the NIRISS field (nearly all of those in the photometric samples) or those for whom the `Sleuth` fit failed (quiescent galaxies without emission lines to extract), in order to still asses their star formation, we again refer back to property maps obtained from broadband SED fitting (section 2.3.1); the SED posteriors include UV star formation rate (SFR) maps. While UV star formation does have slightly different properties and timescales than Hα star formation, it is suitable for evaluating star formation behaviour in this thesis when emission line maps

are not available.

Chapter 5

Results - Photometric Sample

The photometric sample consists of 24 sample galaxies in MACS0417 and 71 in MACS1423, all within $z \epsilon$ 0.5-2.0. Each sample galaxy has at least one (up to four) mass and redshift matched control galaxy[1] (average number of controls per sample galaxy is 1.7 in the MACS0417 photometric sample, and in all other samples, controls and sample galaxies are 1:1). Here we will outline the findings for how interacting galaxies compare to isolated ones in the photometric sample. As it is larger in numbers, this photometric sample is better as a population study than the subset spectroscopic sample that will be explored in Chapter 6.

5.1 Clumpiness of galaxies

For the MACS0417 photometric sample, when each sample and control galaxy is equally weighed, we find that the average number of off-center clumps in an interacting galaxy was 2.833, and for an isolated galaxy it was 2.561 - interacting galaxies in MACS0417 are slightly more clumpy when all mass ranges are considered. When the isolated galaxies are averaged for a 1:1 comparison with the sample galaxies, the

[1]In the case of multiple controls, the controls are averaged so as to facilitate 1:1 comparisons with their assigned sample galaxy.

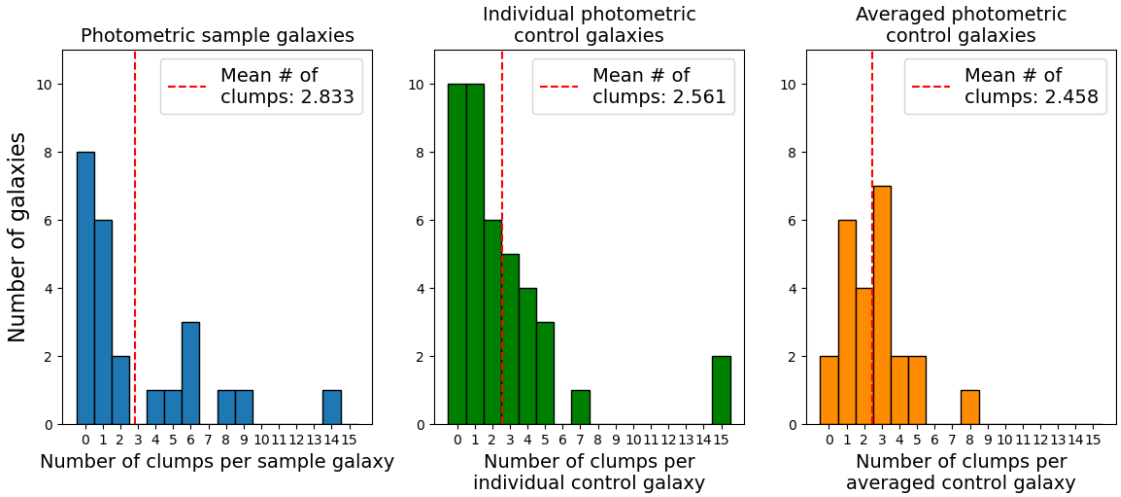

Figure 5.1: The number of clumps per galaxy in the MACS0417 photometric sample and control galaxies. There are 24 sample galaxies and 41 control galaxies. We can see that on average, interacting galaxies are more clumpy, but also experience larger variations in the amount of clumps.

average number of clumps drops to 2.458. These results are portrayed in Figure 5.1. When all mass ranges are considered, 33.3% (8/24) of interacting galaxies do not have off-center clumps, compared to 24.4% (10/41) of all isolated galaxies.

The same analysis was performed on the MACS1423 galaxies, and this cluster field also shows that interacting galaxies have slightly more clumps when all masses are considered. These results are shown in Figure 5.2.

5.2 STAR FORMATION

Using star formation rates and masses derived from SED fitting with `dense_basis`, we plot the star formation main sequence for the entire photometric sample and associated control sample, shown in Figure 5.5. Literature suggests that mergers cause star bursts, thus pushing interacting galaxies above the typical star formation main

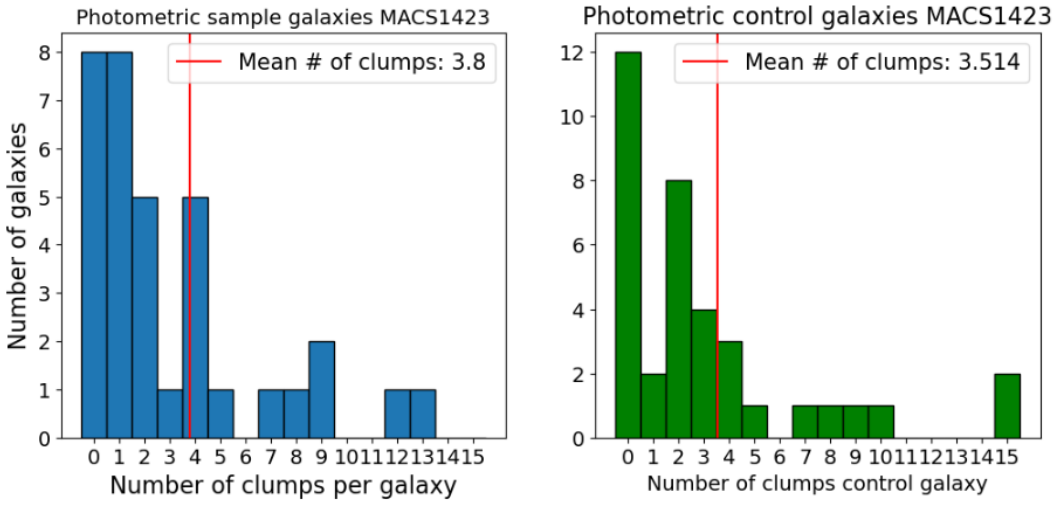

Figure 5.2: The number of clumps in interacting v.s. control galaxies in MACS1423. We see a trend in both cluster fields of more clumps in interacting galaxies.

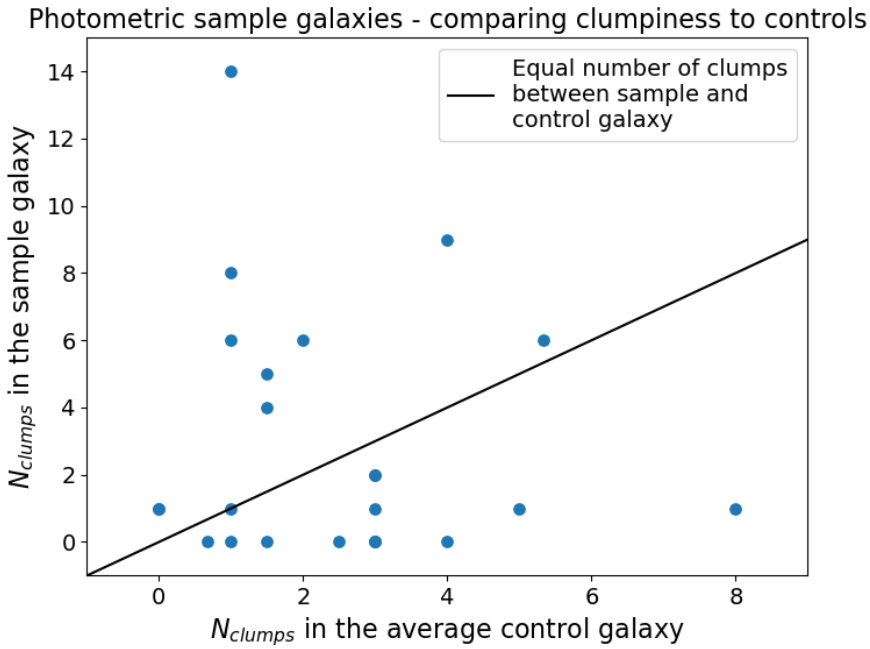

Figure 5.3: Comparing every MACS0417 photometric sample galaxy with its control counterparts: average number of clumps. There are 10 sample galaxies more clumpy than their controls, 12 that are less clumpy, and one where the clumpiness is equal.

Table 5.1: Mean star formation rates binned by mass for interacting and control galaxies ($log(SFR[M_\odot/yr])$).

	Sample	Controls
M<9	-2.6302±0.2698	-2.7982±0.3002
9<M<10	-0.3707±0.2945	-0.6165±0.2296
M>10	-0.4599±0.4842	0.0042±0.3416

sequence (Figure 5.4).

With the photometric sample, narrowing in on a lower-mass range of $log_{10}M = 9 - 10M_\odot$, we see that there is a noticeable offset between the median SFR values of the control and interacting samples at this mass range (Figure 5.6), by a factor of ∼2 in log SFR.

5.2.1 Where is the star formation

All galaxies in this thesis were run through the clump-detection pipeline to locate their off-center clumps. We find that the average number of clumps is consistently between 2-5 (Table 5.2). Other works (see Mandelker et al. (2014)) find an average of 3-4 clumps per galaxy in simulations. By identifying these clumps, we are also able to quantify the amount of star formation rate they contribute to their host galaxy (Table 5.2.1).

In the 9-10 $\log M_\odot$ region of the sample, we see the highest star formation rates

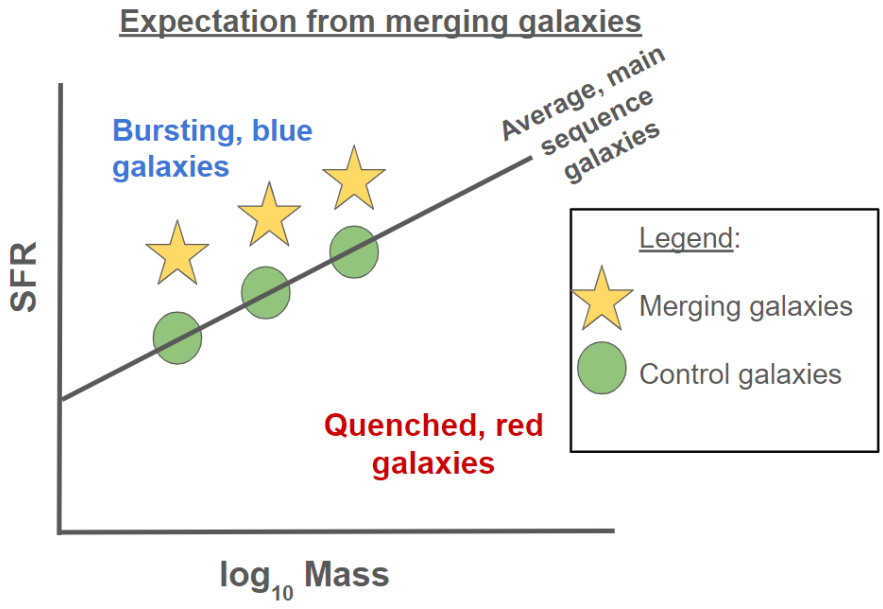

Figure 5.4: Expectations for merger galaxies on the star formation main sequence (SFMS). Mergers are known to induce star formation, so we anticipated seeing an offset in the sample and control populations on the SFMS.

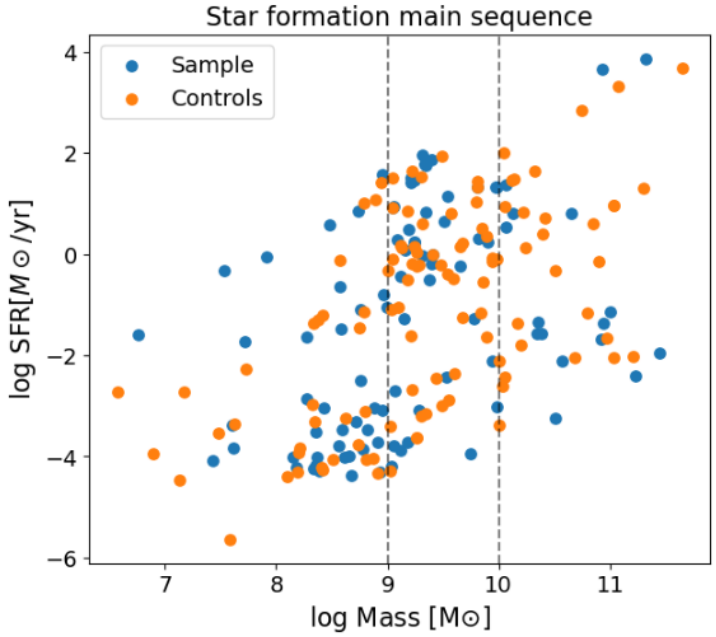

Figure 5.5: Star formation main sequence for photometric interacting and isolated galaxies of all masses, from both cluster fields. Mass ranges considered in interpretation marked with dashed lines. Within the mass range 9-10$M_{\odot}$, we see the main sequence offset we expect. Interacting galaxies are higher in log SFR by a factor of $\sim$2.

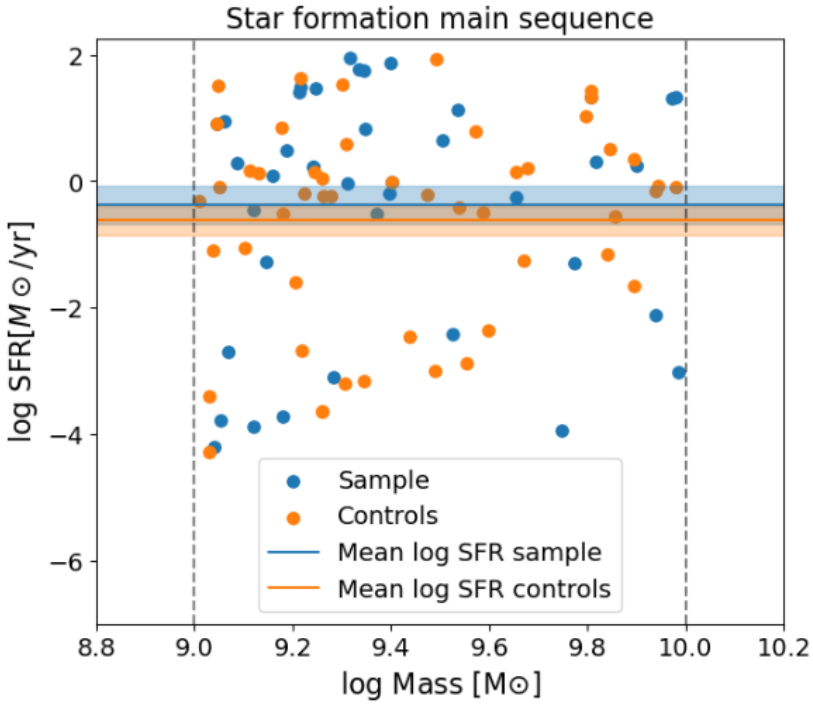

Figure 5.6: Star formation main sequence between $log_{10}M = 9 - 10M_{\odot}$. We see that interacting galaxies in this mass range are experiencing more star formation than the controls. Bootstrap resampling ($N_{resamples} = 200$) of the median values shows the separation between the two populations.

Table 5.2: Number of clumps across all samples

	# clumps
MACS0417 sample	2.833 ± 0.733
MACS0417 controls	2.561 ± 0.519
MACS1423 sample	2.944 ± 0.498
MACS1423 controls	4.324 ± 0.670
all samples	2.916 ± 0.411
all controls	3.679 ± 0.551

for both interacting galaxies and control galaxies (Table 5.2). When we look at these same mass bins and instead consider the number of clumps, we find that the interacting galaxies also have more clumps than the controls between 9-10 $\log M_{\odot}$. We note that at lower and higher masses we do not observe correlations between star formation rates and number of clumps, but do see a relationship at intermediate

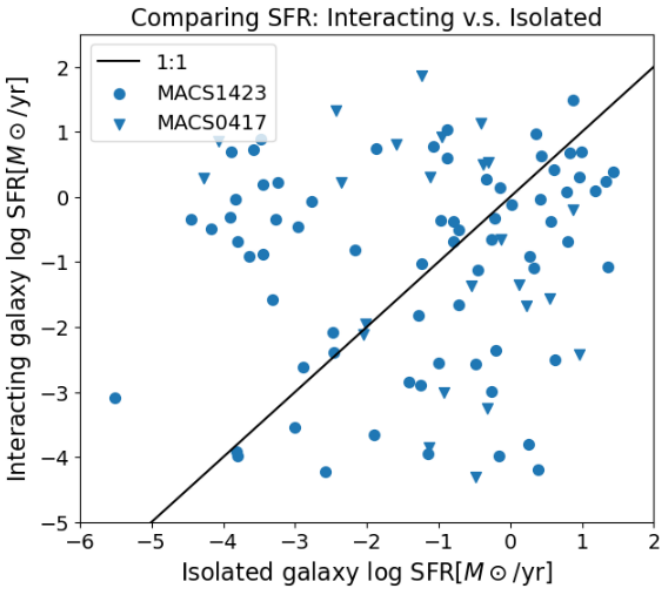

Figure 5.7: Comparing UV star formation rates between interacting and non-interacting galaxies. Based on the lack of points on the 1:1 line, we see that despite being similar in mass and redshift, it is unlikely that control galaxies and interacting galaxies have similar SFRs. This alludes to the situational irregularities mentioned by Kennicutt et al. (1987), and highlights the importance of population analysis instead of 1:1 comparisons of individual sample and control galaxy pairs.

Table 5.3: Percentage of UV SFR coming from the clumps (all masses)

	Mean % SFR in clumps
MACS0417 sample	2.317 ± 1.426
MACS0417 controls	9.844 ± 2.445
MACS1423 sample	4.019 ± 1.298
MACS1423 controls	2.030 ± 0.638
all samples	3.685 ± 1.057
all controls	4.458 ± 0.985

masses. The number of clumps in each mass bin is shown in table 5.4.

Table 5.4: The average number of clumps in three mass bins for each the sample and control galaxies. We see a trend in the 9-10$M_\odot$ range, where interacting galaxies are higher in both star formation rate and number of clumps.

	Sample	Controls
M<9	1.852±0.372	5.846±1.710
9<M<10	3.489±0.661	3.121±0.558
M>10	3.043±0.782	2.821±0.670

Chapter 6

Results - Spectroscopic Sample

The subset of MACS0417 galaxies that have NIRISS data allows us to take a closer look at some of the interacting systems from the photometric sample. While the sample is limited in number with only 9 sources and not ideal for a population study, we are able to investigate individual cases of interacting galaxies compared to control galaxies.

6.1 Clumpiness of galaxies

For the spectroscopic sample, where each sample galaxy is matched 1:1 with a control of equivalent mass and redshift, the average number of clumps for interacting galaxies is 3.111, while the average number of clumps for an isolated galaxy is 4.444. 22.2% (2/9) of interacting galaxies are without off-center clumps, compared to an interesting 0% of isolated galaxies. See Figure 6.1. The average offset in number of clumps between sample and control is 2.667. See Figure 6.2.

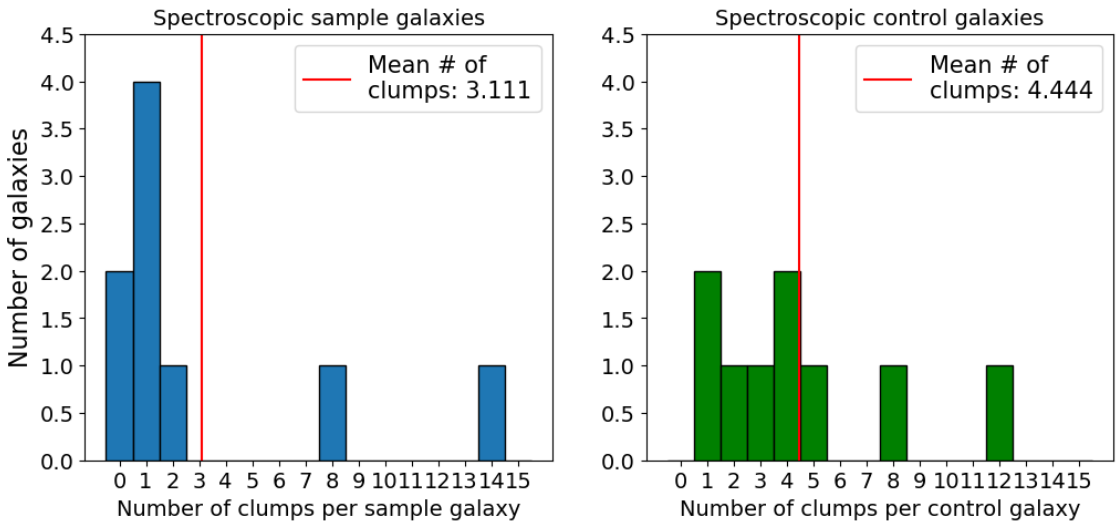

Figure 6.1: The number of clumps per galaxy in the spectroscopic sample and control galaxies. There are 9 of each sample and control galaxies. We can see that on average, in this small sample of 9 galaxies, control galaxies are more clumpy.

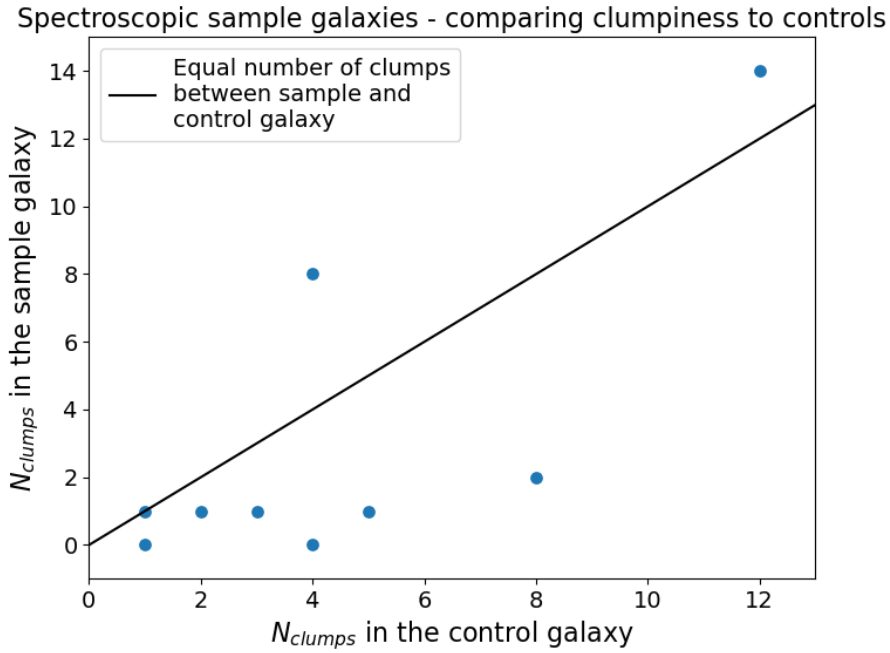

Figure 6.2: Comparing every spectroscopic galaxy with its control counterpart: number of clumps. Most (save two) control galaxies are more clumpy than their partner sample galaxy.

6.2 Star formation

The spectroscopic sample is a subsection of the larger photometric sample for the interacting galaxies in MACS0417 that have NIRISS spectra, and newly assigned control galaxies who also fall in the NIRISS field. The star formation main sequence is shown in Figure 6.3, where sample galaxies tend to fall lower than the controls. The star formation is examined further in the clumps - it was found that the clumps in interacting galaxies contribute 8.966% of the galaxy's Hα SFR, while in the control sample this percentage was 27.662%. Control galaxies had an average of 4.444 clumps, and interacting galaxies an average of 3.111 (Figure 6.1). Using this information, we can derive the percentage of Hα SFR in each average clump. For controls, the average clump contributes 6.225% to the SFR, and for interacting galaxies the average clump contributes 2.882% of the galaxy's SFR. Comparing to results from Guo et al. (2015), where they find that the average clump contributes 4-10% of the SFR, we see that in our spectroscopic sample, the control galaxies' clumps are within this expected range, but the interacting galaxy clumps are below what we would expect.

6.2.1 Burstiness

In the spectroscopic sample, we have the unique opportunity to calculate "burstiness": a metric for tracking the timescales of star formation events. Burstiness ($log_{10}(\eta_{UV})$) is the ratio of the Hα flux to the UV flux (Estrada-Carpenter et al., 2023; Asada et al., 2024). Because the Hα flux is sensitive to shorter-timescale changes in a galaxy or clump's star formation than the UV flux (due to Hα's origin in the hottest short-

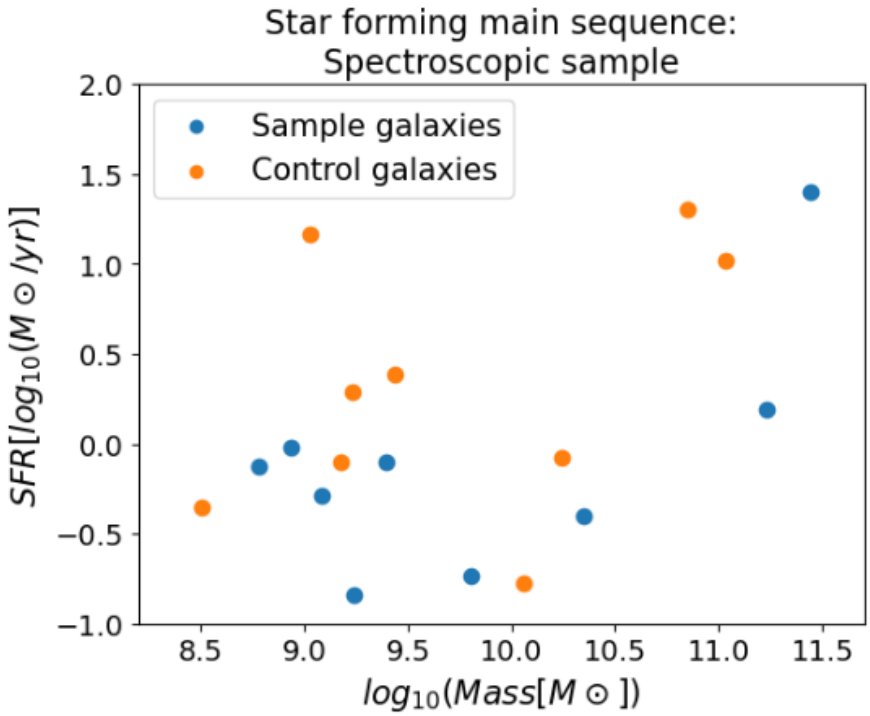

Figure 6.3: The Hα star formation main sequence, obtained from NIRISS emission line maps.

lived OB stars), the ratio of the two gives a quantitative representative of when the observed star formation is taking place. If η_{UV} >1, then we are seeing more Hα emission than UV, meaning that the hottest, youngest stars are present, and this region is experiencing an active starburst. Likewise, if $\log_{10}\eta_{UV} < 1$, there is more UV star formation flux, indicating that the galaxy has ceased to make new, hot stars, and is quenching. For each galaxy and control with both UV (HST F606) and Hα (NIRISS F150 or F200) flux data, we are able to make spatially resolved burstiness maps. One example of this is Figure 6.4, and all images are shown in Appendix D. These images show that the bright, clumpy regions of the spectroscopic galaxies show significant correlation to the bursting regions in the burstiness maps.

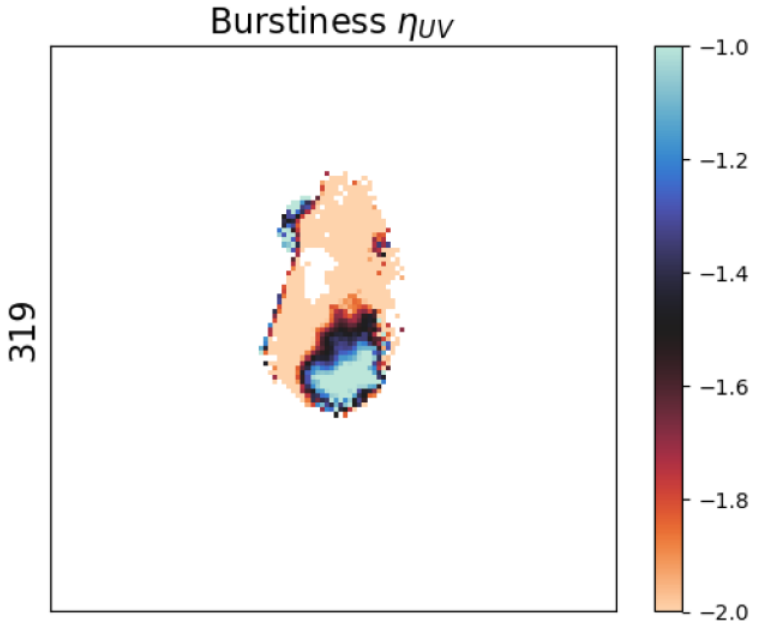

Figure 6.4: $log_{10}(\eta_{UV})$ for the control galaxy ID=319. We can see clumpy regions near the bottom of the galaxy that show clearly heightened star formation burstiness compared to the rest of the galaxy.

Chapter 7

Discussion

7.1 Effect of interactions on star formation rates in interacting galaxies and clumps

In this thesis we test the theory that interactions and mergers cause augmented star formation (Ellison et al., 2008) in participating galaxies due to merger-induced gas compression. In the photometric sample, we do see augmented star formation (with respect to non-interacting galaxies) in interacting galaxies with masses between $log_{10}M = 9 - 10M_{\odot}$. The star-formation main sequence (Figures 5.5 and 5.6) shows the offset between the median SFR of interacting and isolated galaxies.

When we delve deeper into this sub-sample mass range, we also find that interacting galaxies are more likely to be clumpy. Interacting galaxies between $log_{10}M = 9 - 10M_{\odot}$ have the highest amount of clumps among all the interactions, and have more clumps than their mass-matched controls. This suggests a link between increased star formation, increased clump presence, and interactions. We note that higher and lower mass galaxies do not follow these trends, a discrepancy that warrants further study beyond this thesis.

Interacting galaxies being more clumpy suggests that merger scenarios and clumpiness go hand-in-hand; many have proposed that clumpy disks are the result of gravitational instabilities caused by galaxy-galaxy interactions (Guo et al., 2015; Messa et al., 2022), specifically minor mergers (Kalita et al., 2024), as they are less destructive to the massive galaxy's overall structure, but still cause considerable perturbations to the system. The results in this work come from exclusively major mergers - suggesting than major mergers may also cause clumps. We observe most of our major-merger galaxies in their early, pre-destructive stages (as confirmed by the infrequency of strong tidal features), so it is possible that these clumps we have observed will not survive the rest of the interaction.

Alternatively, these observed clumps may not be a produce of condensed material after a merger, they may instead be an accreted relic of past minor mergers, not formed within their host galaxies at all. Recent studies (Estrada-Carpenter, 2024) and simulations (Mandelker et al., 2014) have shown that this is possible; clumps often differ significantly in metallicity from the surrounding disk material, indicating that they were not formed from the disk. Having lower metallicities than the disk means that there must have been a source of pristine gas present during their formation. This could mean they are remnants of previously accreted satellite galaxies or minor merger remnants.

7.2 Effect of interactions on clump star formation rate contributions

While we observe an increase in star formation rate and in number of clumps for interacting galaxies in the mass range $log_{10}M = 9 - 10M_{\odot}$, we do not see an increase in percentage of star formation in the clumps of interacting galaxies (Table 5.2.1). There are a few possible explanations for this. Firstly, if star formation is induced due to interactions, it may be only induced in the diffuse disk or halo material of the interacting galaxies, while the already-dense clump regions do not experience additional gas condensation. If the clumps maintain their SFR while the disk SFR raises around them, they will experience a reduced contribution to the overall SFR, as shown in the last row of Table 5.2.1. Similarly, if the surroundings experience additional star formation, the interaction may induce quenching in the clumps. The burstiness maps in Section 6.2.1 would allow this theory to be tested with a larger sample of galaxies with spectroscopic data.

In comparing to the literature on clump contributions to star formation rates, it is found that on average, each individual clump contributes ∼4-10% of the SFR of its host galaxy (Guo et al., 2015). In the spectroscopic sample, the clump SFR percentages are reported in Section 6.2 (8.995% in the sample, 27.662% in the controls), and the mean number of clumps from the spectroscopic sample and control galaxies from Section 6.1 (3.111 for the sample, 4.444 for the controls), this leads to average individual clump SFR percentages of 2.882% per clump for the sample, and 6.225%

per clump for the controls. Within the margin specified by Guo et al. (2015), this tells us that our sample clumps are below average. This leads back to the conclusions that a larger sample of spectroscopic data is needed to overcome these fluctuations. There are multiple possible explanations for this, but further spectroscopic analysis is required before we are able to conclusively identify specific theories.

7.3 Gravitational Lensing

In this thesis, we benefit from the gravitational lensing effect that comes from observing in a galaxy cluster field - distant background galaxies that are magnified due to the cluster mass in the foreground are resolvable in more detail than otherwise would have been possible. However, in addition to magnification, lensing causes distortion in the appearances and light distributions of galaxies, which are less desirable (for this thesis) lensing effects, and can cause shear and image duplication. To account for lensing, we would have had to perform lensing corrections on all observations and property maps of each galaxy in all samples. Lensing, as it can distort the galaxy's appearance from the source plane to the lensed plane, can result in over-estimated values for both mass and star formation (Gledhill et al., 2024). Correcting for lensing effects would reduce uncertainties and increase confidence in these results, and is a topic for future work.

Chapter 8

Conclusions

Using spectroscopic grism data from the NIRISS instrument on the JWST, and imaging data from NIRCam and HST, we conduct a study on star formation trends and clumps in interacting galaxies. This study includes two samples, the photometric sample consisting of 24 interacting galaxies and 41 isolated galaxies in MACS0417, and 71 interacting galaxies and 71 isolated galaxies in MACS1423, and the spectroscopic sample, a subset of 9 galaxies in interacting pairs that have NIRISS data, and their controls. The main conclusions from this thesis are summarized below.

1. In the photometric sample, within the mass range of $log_{10}M = 9 - 10M_{\odot}$, we find that interacting galaxies show more star formation, a result that agrees with literature on merging systems. We note that high and low mass galaxies do not follow this trend and experience significant variations in both number of clumps and SFR.

2. The interacting galaxies at this mass range also have more clumps than the controls. This suggests that clumps are linked to interactions (at least at this mass range), and we theorize that clumps may be the result of interaction-induced disk collapse, or the artifacts of previous minor mergers.

3. In the spectroscopic sample, the per-clump percentage of galaxy SFR is as

expected in the control galaxies, but below average in the sample galaxies. This, and the fact that in inteacting galaxies we see an overall decrease in clump contribution to SFR leads us to believe that this is due to one of two possible scenarios: Either mergers cause an overall increase in disk-based star formation while clumps remain consistent, or clumps are stifled by interactions. Either scenario would explain why the clumps are more prominent/make up a larger percentage of the galaxy SFR in the non-interacting galaxies.

All in all, we were able to complete both a photometric population study and a smaller-sample spectroscopic study of star formation and clumps in interacting and non-interacting galaxies. This is a field with a bright future and many avenues still to be explored.

Chapter 9

Acknowledgments

This work was completed with the help and data preparation of the CANUCS collaboration and its members. Special thanks goes to Shannon MacFarland for her work on broadband imaging and SED fitting - it was instrumental to the completion of this thesis.

This research was conducted with the computing resources supported by the Canadian Advanced Network for Astronomy Research (CANFAR), operated with The Digital Research Alliance of Canada and the Canadian Astronomy Data Centre. These facilities are supported by the Canada Space Agency, the Canadian Foundation for Innovation, Canada's National Research and Education Network, and the National Research Council of Canada.

Appendix A

Abbreviations/Symbols

- CANUCS: the CAnadian NIRISS Unbiased Cluster Survey
- Dec: Declination
- HST: the Hubble Space Telescope
- JWST: the James Webb Space Telescope
- kpc: kiloparsecs
- $M_{\odot}$: Units of solar mass
- NIRCam: the Near InfraRed Camera
- NIRISS: the Near InfraRed Imager and Slitless Spectrograph
- RA: Right Ascension
- SED: spectral energy distribution
- SFR: star formation rate
- sSFR: specific star formation rate
- UV: Ultraviolet

Appendix B

Sample and control galaxies - properties

All star formation and mass quantities are from CANUCS collaboration photometry catalogues.

Table B.1: Average star formation quantities - all samples MACS0417

	Average SFR $[log_{10}(M_{\odot}/yr)]$	Average sSFR $[log_{10}(yr^{-1})]$
P Sample	-0.7892 ± 0.3453	-10.6253 ± 0.4328
P Controls	-0.9255 ± 0.2533	-10.7437 ± 0.2394
S Sample	-1.1283 ± 0.6535	-10.9364 ± 0.8222
S Controls	-1.105 ± 0.7149	-10.8347 ± 0.5343

Table B.2: Average star formation quantities - all samples MACS1423

	Average SFR $[log_{10}(M_{\odot}/yr)]$	Average sSFR $[log_{10}(yr^{-1})]$
P Sample	-1.4742 ± 0.2702	-10.4805 ± 0.2298
P Controls	-1.1817 ± 0.2501	-10.2979 ± 0.2082

Table B.3: Star Formation - Spectroscopic Sample Galaxies

ID	log SFR	log sSFR	# Clumps	Clump SFR %
43	-0.734	-10.540	0	0
47	-0.402	-10.753	1	21.302
100	-0.103	-9.501	2	3.287
121	-0.841	-10.082	2	26.242
172	-0.121	-8.905	1	1.515
196	-0.291	-9.377	1	0.936
535	-0.02	-8.958	1	0.082
1265	0.191	-11.038	9	24.876
1270	1.402	-10.038	14	2.3483

Table B.4: Star Formation - Spectroscopic Control Galaxies

ID	log SFR	log sSFR	# Clumps	Clump SFR %
545	-0.773	-10.829	1	19.224
1326	-0.074	-10.313	2	5.315
319	0.388	-9.050	5	50.503
1274	0.287	-8.945	8	23.246
531	-0.353	-8.863	3	53.600
299	1.167	-7.862	4	5.254
571	-0.104	-9.280	1	20.236
250	1.017	-10.018	4	55.426
1307	1.299	-9.549	12	15.556

Table B.5: General Properties - Spectroscopic Sample Galaxies

ID	log M	z	RA	Dec	NIRISS or broadband	Control ID
43	9.807	1.7127	64.40550	-11.93381	N	545
47	10.352	1.7069	64.40539	-11.93358	N	1326
100	9.399	1.2645	64.39671	-11.92671	N	319
121	9.242	1.2658	64.39777	-11.92533	N	1274
172	9.784	1.0590	64.38421	-11.92110	N	531
196	9.087	1.0583	64.38617	-11.91978	BB	299
535	8.937	1.0394	64.38144	-11.90077	N	571
1265	11.229	1.2700	64.39739	-11.92903	BB	250
1270	11.441	1.2725	64.39749	-11.92741	N	1307

Table B.6: General Properties - Spectroscopic Control Galaxies

ID	$log_{10}M$	z	RA[^{o}]	Dec[^{o}]	NIRISS or Broadband	Paired to:
545	10.057	1.4530	64.41031	-11.90052	N	43
1326	10.240	1.4310	64.41162	-11.90417	N	47
319	9.439	1.4640	64.37851	-11.91280	N	100
1274	9.233	1.4516	64.39304	-11.92196	N	121
531	8.510	1.0524	64.39764	-11.90105	BB	172
299	9.030	1.3106	64.40282	-11.91352	N	196
571	9.177	1.3196	64.40408	-11.89812	N	535
250	11.035	1.0416	64.39977	-11.91654	N	1265
1307	10.848	1.3471	64.38033	-11.90834	N	1270

Table B.7: General Properties - Photometric Sample Galaxies MACS0417

ID	log M	z	RA	Dec	Control IDs
47	9.807	1.7127	64.40550	-11.93381	1326
43	10.352	1.7069	64.40539	-11.93358	545
100	9.399	1.2645	64.39671	-11.92671	319, 929
121	9.242	1.2658	64.39777	-11.92533	58, 790, 212
172	9.784	1.0590	64.38421	-11.92110	809
196	9.087	1.0583	64.38617	-11.91978	299
535	8.937	1.0394	64.38144	-11.90077	754, 867
537	8.739	0.9877	64.37958	-11.90090	531
698	8.575	0.7070	64.41578	-11.88812	906
705	9.046	0.6538	64.41407	-11.88761	665, 729
755	10.937	1.1215	64.42008	-11.88395	804
764	10.918	1.1302	64.41917	-11.88341	84, 1307
875	9.188	1.2919	64.39129	-11.87591	571, 607
1389	9.537	1.2975	64.39201	-11.87443	414
904	10.132	1.3740	64.39413	-11.87345	210, 382
922	9.817	1.3316	64.39447	-11.87206	256, 514, 1316
1265	11.229	1.2700	64.39739	-11.92903	250
1270	11.441	1.2725	64.39749	-11.92741	838
1369	10.385	1.0395	64.42024	-11.88499	41, 920
1370	10.069	1.0341	64.41985	-11.88486	285, 1382
1371	9.398	1.0804	64.41589	-11.88501	429, 93
1372	9.984	1.1417	64.41539	-11.88481	123, 408, 488, 1278
1398	10.573	1.3993	64.38815	-11.87362	1285
1397	10.504	1.3360	64.38753	-11.87376	718

Table B.8: General Properties - Photometric Control Galaxies MACS0417

ID	$log_{10}M$	z	RA^o	Dec^o	Paired to:
545	10.0565	1.4530	64.41031	-11.90052	43
1326	10.2395	1.4310	64.41162	-11.90417	47
319	9.4385	1.4640	64.37851	-11.91280	100
929	9.4015	1.3027	64.39073	-11.87147	100
58	9.2585	1.3860	64.39253	-11.93129	121
790	9.2615	0.9851	64.40027	-11.88193	121
212	9.3055	1.4779	64.39852	-11.91909	121
809	8.7925	0.7793	64.40144	-11.88054	172
299	9.0295	1.3106	64.40282	-11.91352	196
754	9.0365	0.9727	64.40628	-11.88414	535
867	9.1295	1.1116	64.39879	-11.87675	535
531	8.5095	1.0524	64.39764	-11.90105	537
906	8.5705	0.7340	64.39561	-11.87296	698
665	9.0475	0.6403	64.42475	-11.89117	705
729	9.0295	0.5172	64.42688	-11.88574	705
804	11.0305	1.0615	64.41453	-11.88071	755
84	10.8985	0.9465	64.39436	-11.92874	764
1307	10.8475	1.3471	64.38033	-11.90834	764
571	9.1765	1.3196	64.40408	-11.89812	875
607	9.2065	1.4608	64.39363	-11.89598	875
414	9.5385	1.4483	64.37953	-11.90783	1389
210	10.1965	1.2661	64.37740	-11.91922	904
382	10.1705	1.3209	64.38353	-11.91003	904
256	9.8395	1.2681	64.41354	-11.91633	922
514	9.8935	1.4464	64.41476	-11.90210	922
1316	9.8545	1.3235	64.38306	-11.90694	922
250	11.0345	1.0416	64.39977	-11.91654	1265
838	11.2075	1.4224	64.38992	-11.87881	1270
41	10.3945	1.1033	64.40377	-11.93436	1369
920	10.4135	1.1539	64.39539	-11.87226	1369
285	10.0445	0.8325	64.38454	-11.91471	1370
1382	10.0345	0.9937	64.40042	-11.87581	1370
429	9.6775	1.0465	64.39905	-11.90667	1371
93	9.3015	1.3662	64.40685	-11.92753	1371
123	10.0005	1.3355	64.39306	-11.92514	1372
408	9.9395	1.3708	64.40727	-11.90837	1372
488	9.9785	1.2792	64.41601	-11.90376	1372
1278	9.9425	0.8519	64.37600	-11.91844	1372
1285	10.6845	1.1481	64.38685	-11.91842	1398
718	10.5105	1.0707	64.42392	-11.88681	1397

Table B.9: First Half - General Properties - Photometric Sample Galaxies MACS1423

ID	log M	z	RA[^{o}]	Dec[^{o}]	Control IDs
636	10.104	1.4162	215.93892	24.09200	32
721	9.359	0.9301	215.95163	24.09745	43
664	10.217	0.7336	215.94074	24.09355	58
546	9.776	0.5356	215.93862	24.08683	69
1335	10.326	0.7730	215.96603	24.09559	82
9345	6.504	0.7170	215.92678	24.09220	97
700	9.335	0.7658	215.96513	24.09543	101
1325	9.861	1.4191	215.94070	24.08999	115
634	9.095	1.1412	215.94673	24.09191	120
643	9.669	0.6016	215.94269	24.09238	135
1272	9.127	0.5554	215.94287	24.06979	136
356	9.073	0.5348	215.94237	24.07668	141
121	11.019	0.5170	215.95190	24.06389	142
660	9.007	0.7846	215.94161	24.09315	146
1343	9.887	0.8141	215.96434	24.09732	157
357	8.733	1.3851	215.93444	24.07665	178
1243	9.453	1.3493	215.93854	24.05782	186
402	9.384	0.5370	215.93355	24.07875	189
64	9.057	1.4454	215.93847	24.05953	228
806	9.429	0.9272	215.92988	24.10734	238
647	7.641	0.5491	215.94639	24.09269	243
92	9.307	0.5613	215.94161	24.06189	249
559	10.099	0.6223	215.94347	24.08759	287
604	6.943	0.6911	215.92608	24.09024	290
566	8.648	1.6197	215.95446	24.08810	292
1339	9.569	0.9882	215.94910	24.09636	305
11791	7.570	1.5463	215.93332	24.10982	313
388	8.965	0.5405	215.94072	24.07801	339
119	10.488	0.5988	215.95077	24.06373	353
385	9.330	1.3097	215.93526	24.07806	387
843	7.277	0.5060	215.92720	24.11036	409
163	8.632	0.5449	215.93975	24.06662	476
580	9.302	1.7611	215.94171	24.08883	499
563	8.938	0.6432	215.94058	24.08779	508
582	9.719	0.5322	215.93910	24.08906	556
932	8.571	0.8650	215.95944	24.11849	557
309	8.684	0.5518	215.93010	24.07456	609
625	10.106	0.5585	215.94615	24.09159	622
925	9.229	1.0532	215.95022	24.11768	663
929	8.667	0.6041	215.96354	24.11818	683
1290	9.330	0.9250	215.92813	24.07699	697

Table B.10: Second half - General Properties: Photometric Sample Galaxies MACS1423

IDs	log M	z	RA[^{o}]	Dec[^{o}]	Control IDs
927	9.007	0.5526	215.96274	24.11793	705
1289	10.568	0.6092	215.95613	24.07665	739
247	9.224	0.5288	215.93974	24.07101	740
693	8.646	0.5305	215.95626	24.09491	781
1337	9.070	0.9984	215.94941	24.09631	784
369	8.816	1.1435	215.94177	24.07729	788
192	9.101	1.1101	215.93875	24.06798	799
1338	8.726	1.0078	215.94975	24.09630	807
1317	9.382	0.5166	215.96818	24.08568	816
4414	8.922	1.8047	215.93622	24.06509	826
28	10.170	0.5812	215.93172	24.05658	828
699	10.295	0.7941	215.94078	24.09513	833
384	10.130	0.5475	215.95649	24.07799	837
579	9.604	0.5261	215.94285	24.08891	850
603	8.830	1.8180	215.94116	24.09011	858
334	9.000	1.3195	215.93457	24.07579	861
105	9.531	0.5410	215.94273	24.06242	865
649	8.774	0.7496	215.93705	24.09274	868
7316	9.012	0.8453	215.96002	24.08061	893
433	9.094	0.5103	215.96255	24.08063	897
354	9.514	0.8706	215.92889	24.07673	901
365	10.759	0.5572	215.95422	24.07715	1260
50	9.524	0.5504	215.94046	24.05812	1262
288	8.043	0.9936	215.96346	24.07333	1263
158	8.823	1.7626	215.93667	24.06628	1299
596	8.767	1.1627	215.94973	24.08975	1319
390	9.097	1.2058	215.94333	24.07824	1323
1249	10.533	0.5391	215.93208	24.05886	1332
66	9.205	0.5515	215.94055	24.05956	1334
1271	9.196	0.5302	215.94326	24.06967	1345

Table B.11: First Half - General Properties: Photometric Control Galaxies MACS1423

ID	log M	z	RA[^{o}]	Dec[^{o}]	Paired to:
32	10.3065	1.3585	215.92936	24.05692	636
43	9.3655	1.0434	215.93002	24.05780	721
58	10.1655	0.9849	215.95258	24.05921	664
69	9.8295	0.5185	215.96608	24.05965	546
82	10.3405	0.5654	215.93896	24.06071	1335
97	6.6835	0.8238	215.97154	24.06199	9345
101	9.3355	0.5490	215.95180	24.06213	700
115	9.7955	1.4157	215.93364	24.06351	1325
120	9.0895	0.8630	215.97226	24.06407	634
135	9.6445	0.5426	215.94446	24.06517	643
136	9.1175	0.6264	215.96354	24.06516	1272
141	9.0785	0.6198	215.93511	24.06558	356
142	11.1415	0.5204	215.94194	24.06534	121
146	9.0065	0.9133	215.93713	24.06572	660
157	9.9245	0.6808	215.93378	24.06632	1343
178	8.7105	1.4430	215.94536	24.06725	357
186	9.4805	1.3366	215.95932	24.06761	1243
189	9.3835	0.8133	215.96512	24.06808	402
228	9.0675	1.6210	215.95768	24.07031	64
238	9.4075	1.1698	215.93913	24.07090	806
243	7.6385	0.5458	215.95860	24.07103	647
249	9.2955	0.7538	215.95780	24.07122	92
287	9.9515	0.5515	215.93412	24.07312	559
290	6.7205	0.5420	215.94099	24.07337	604
292	8.6865	1.4013	215.92775	24.07380	566
305	9.8195	0.8976	215.94581	24.07420	1339
313	7.6505	1.4324	215.92684	24.07485	11791
339	8.9835	0.6015	215.92686	24.07620	388
353	10.5145	0.8718	215.96983	24.07675	119
387	9.4135	1.3221	215.96351	24.07797	385
409	7.1515	0.5398	215.93272	24.07910	843
476	8.6355	0.7746	215.92573	24.08311	163
499	9.3555	1.5355	215.96861	24.08421	580
508	8.9455	0.6590	215.92469	24.08468	563
556	9.7485	0.5143	215.93230	24.08744	582
557	8.5605	1.1487	215.96696	24.08774	932
609	8.7195	0.5272	215.96570	24.09056	309
622	9.9695	0.7880	215.93581	24.09134	625
663	9.2145	1.1467	215.92819	24.09330	925
683	8.6845	0.8420	215.93084	24.09440	929

Table B.12: Second Half - General Properties: Photometric Control Galaxies MACS1423

ID	log M	z	RA[^{o}]	Dec[^{o}]	Paired to:
697	9.285	1.0341	215.94293	24.09513	1290
705	9.005	0.7874	215.95963	24.09593	927
739	10.568	0.5371	215.95953	24.09901	1289
740	9.274	0.5252	215.96531	24.09939	247
781	8.675	0.6796	215.92641	24.10526	693
784	9.061	1.1480	215.92905	24.10515	1337
788	8.823	1.4417	215.92677	24.10590	369
799	9.167	1.1251	215.92570	24.10693	192
807	8.727	0.8248	215.92320	24.10742	1338
816	9.392	0.5188	215.95551	24.10826	1317
826	8.960	1.6564	215.92223	24.10915	4414
828	10.222	0.6841	215.92153	24.10928	28
833	10.087	1.0208	215.93568	24.10966	699
837	10.097	0.5077	215.96018	24.10997	384
850	9.703	0.6579	215.94306	24.11099	579
858	8.948	1.6392	215.94958	24.11134	603
861	8.979	1.3468	215.92745	24.11164	334
865	9.731	0.5439	215.93007	24.11208	105
868	8.705	0.5214	215.96111	24.11264	649
893	9.160	0.8811	215.96459	24.11528	7316
897	9.132	0.5775	215.93977	24.11566	433
901	9.606	0.8802	215.95758	24.11618	354
1260	10.717	0.5393	215.95836	24.06405	365
1262	9.686	0.5611	215.97169	24.06468	50
1263	7.981	1.2014	215.97145	24.06472	288
1299	8.828	1.8490	215.94119	24.07957	158
1319	8.920	1.4419	215.94278	24.08735	596
1323	9.123	1.3484	215.93191	24.09001	390
1332	10.434	0.5530	215.94718	24.09424	1249
1334	9.212	0.8474	215.94794	24.09658	66
1345	9.132	0.7430	215.96202	24.09905	1271

Appendix C

RGB Images of the Interacting Pairs (MACS0417)

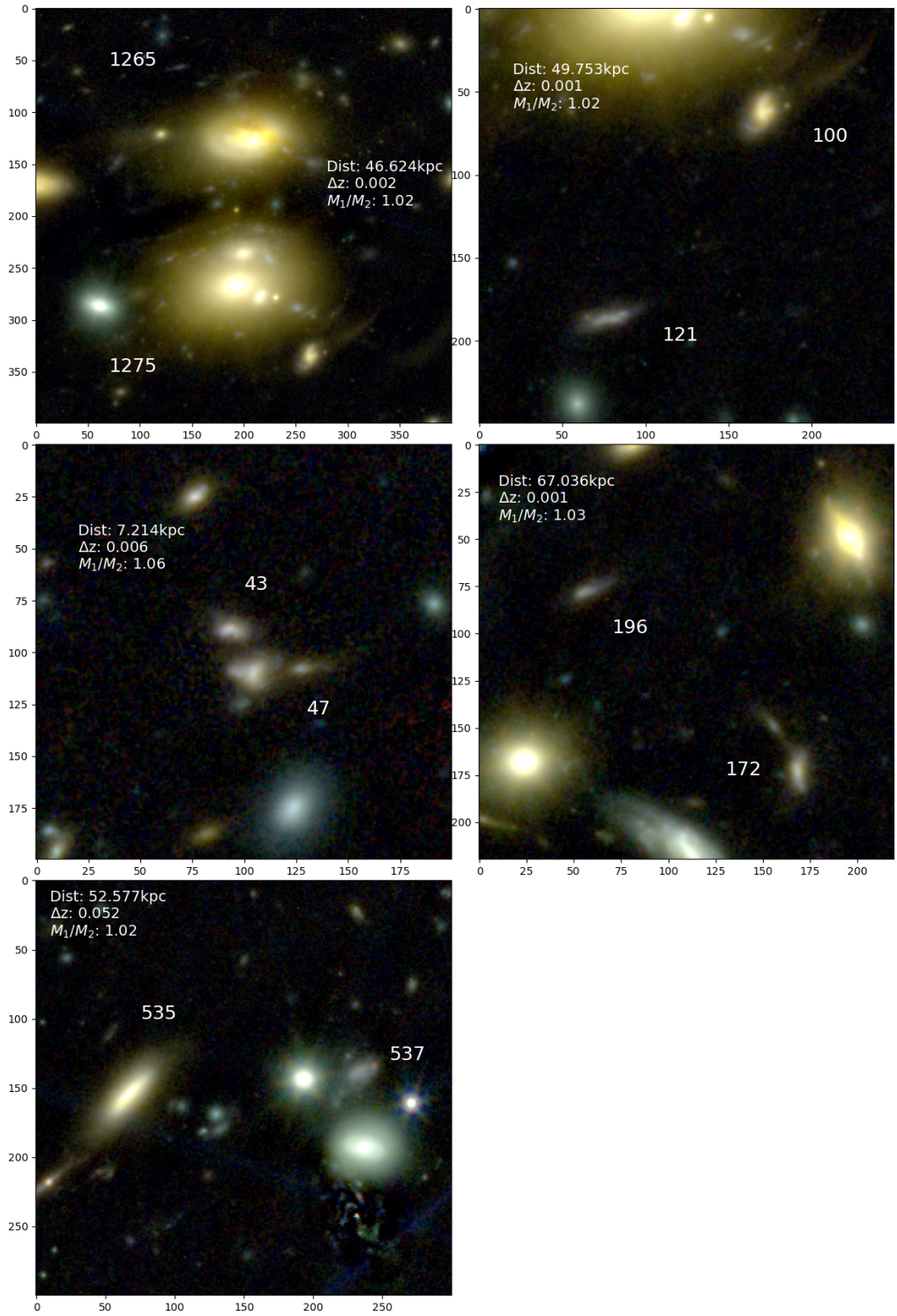

Figure C.1: RGB images of all the spectroscopic pairs in this work (ID=537 does not have NIRISS data and is therefore not included in the sample).

Figure C.2: Photometric Interacting Pairs

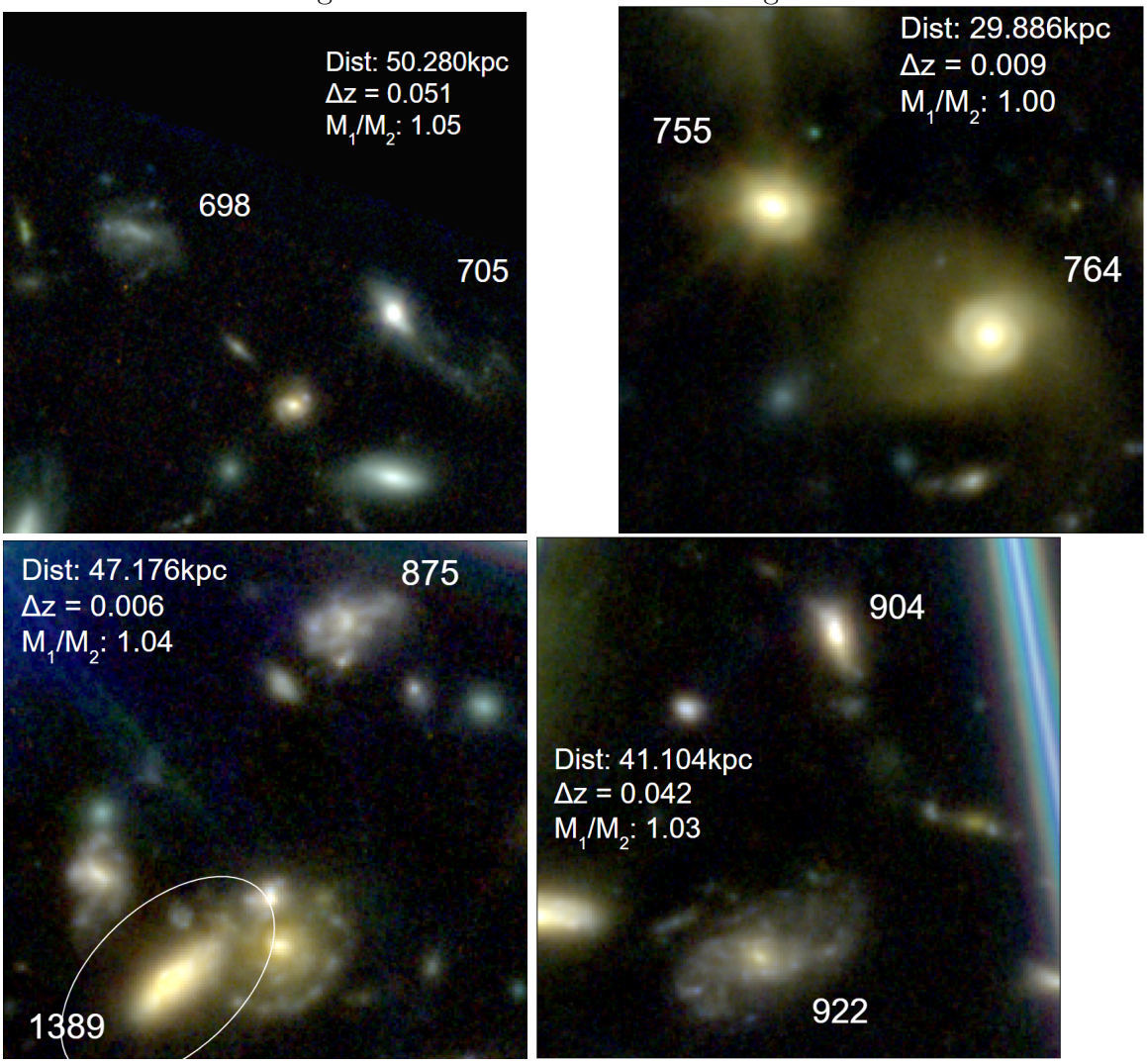

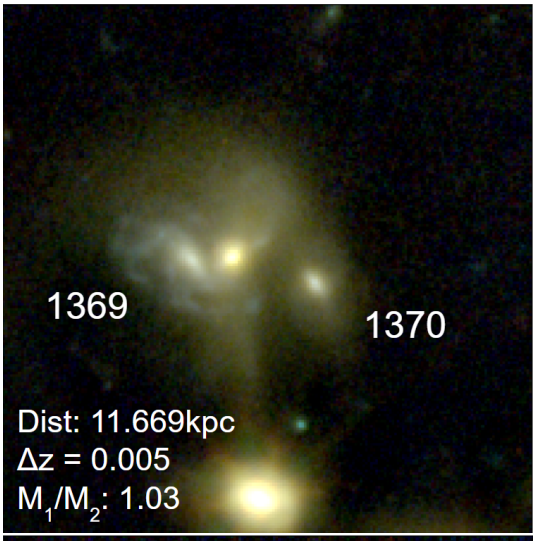
1369
1370
Dist: 11.669kpc
Δz = 0.005
M1/M2: 1.03

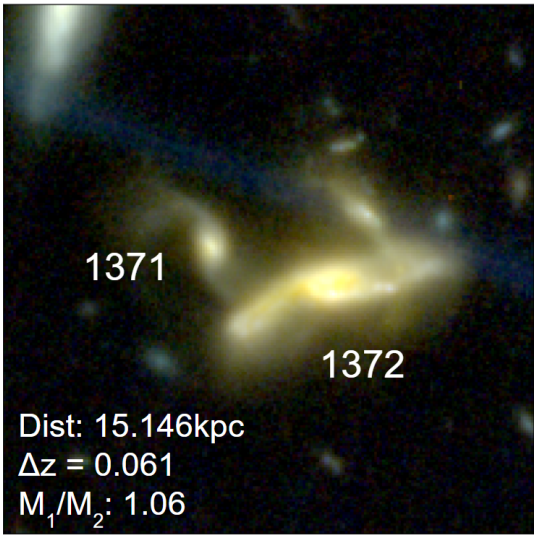
1371
1372
Dist: 15.146kpc
Δz = 0.061
M1/M2: 1.06

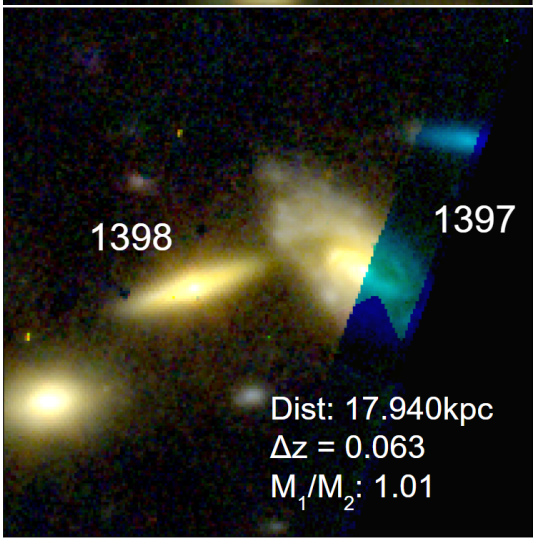
1398
1397
Dist: 17.940kpc
Δz = 0.063
M1/M2: 1.01

Appendix D

Burstiness Maps

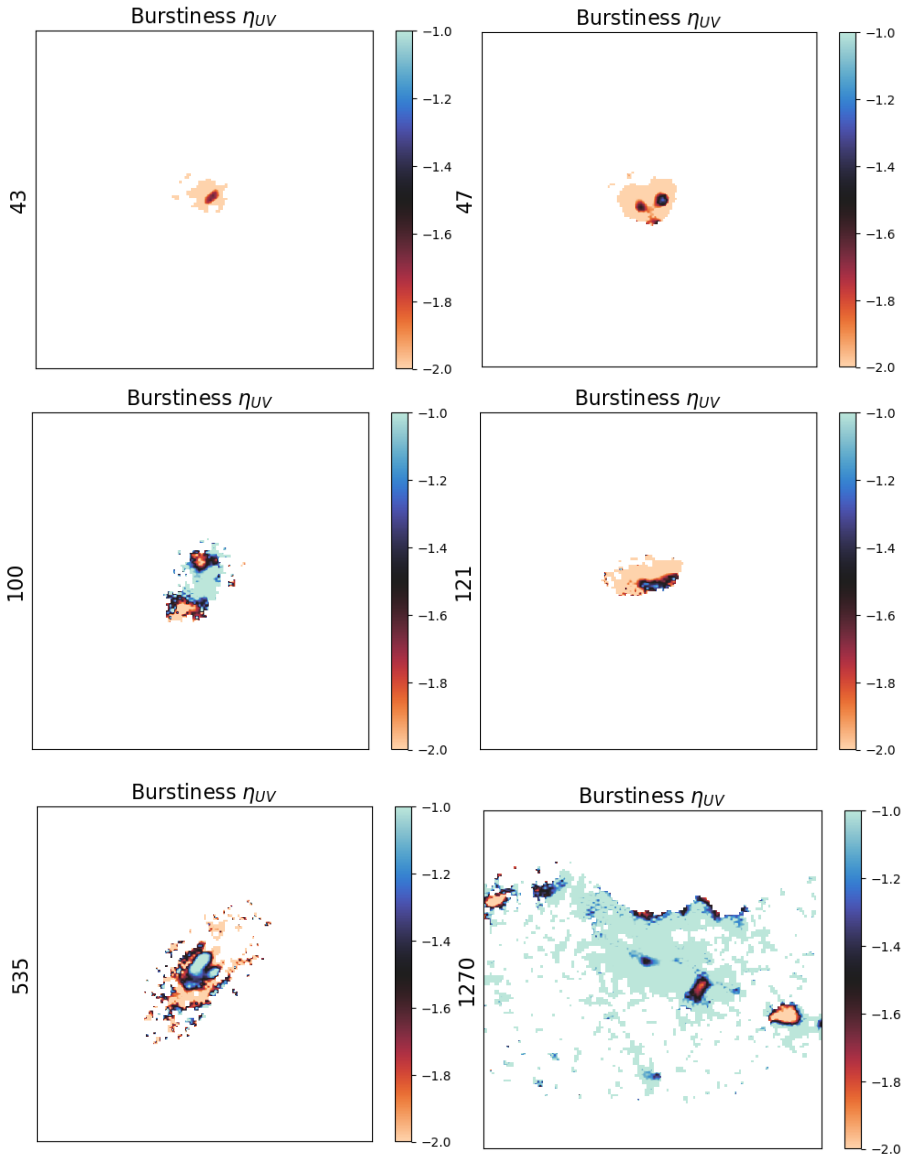

Figure D.1: Spectroscopic interacting sample MACS0417 (140 pixels x 140 pixels)

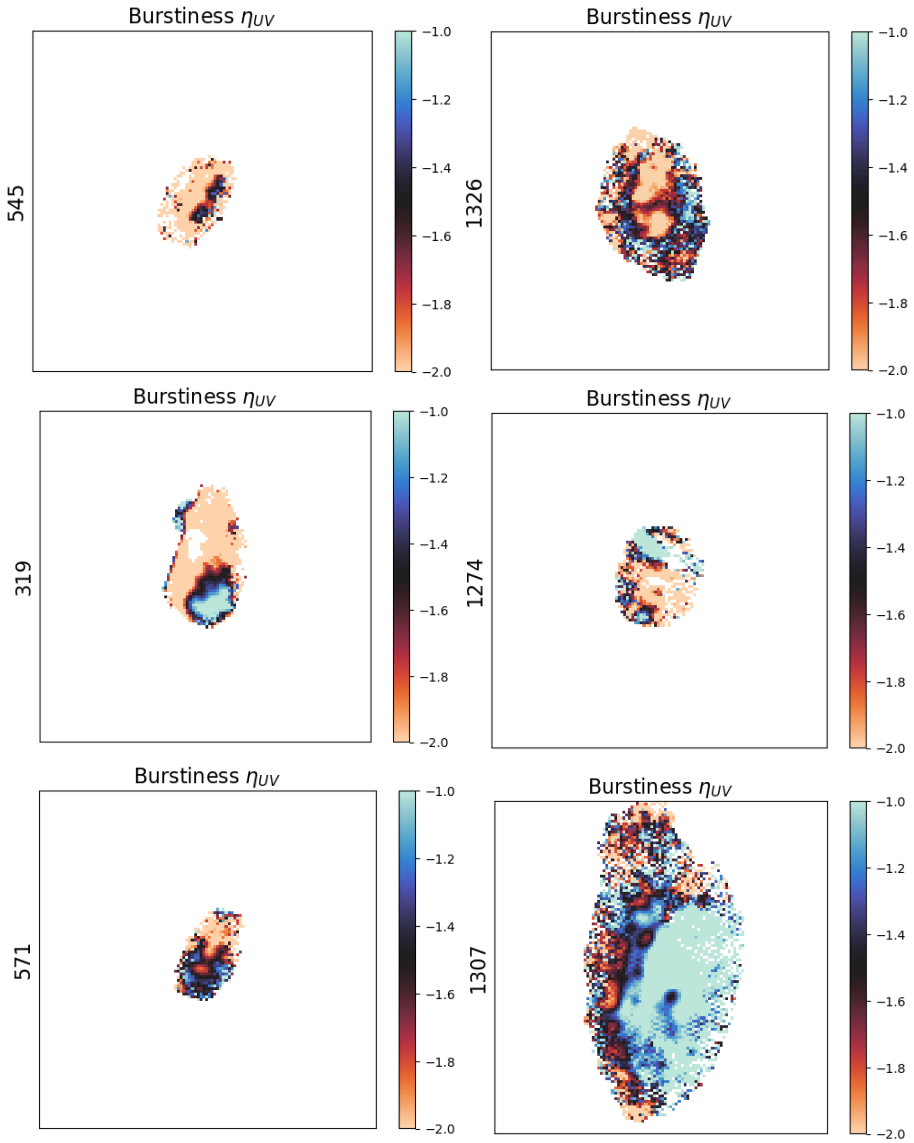

Figure D.2: Spectroscopic control sample MACS0417 (120 pixels x 120 pixels)

Appendix E

Hα Emission Line Maps

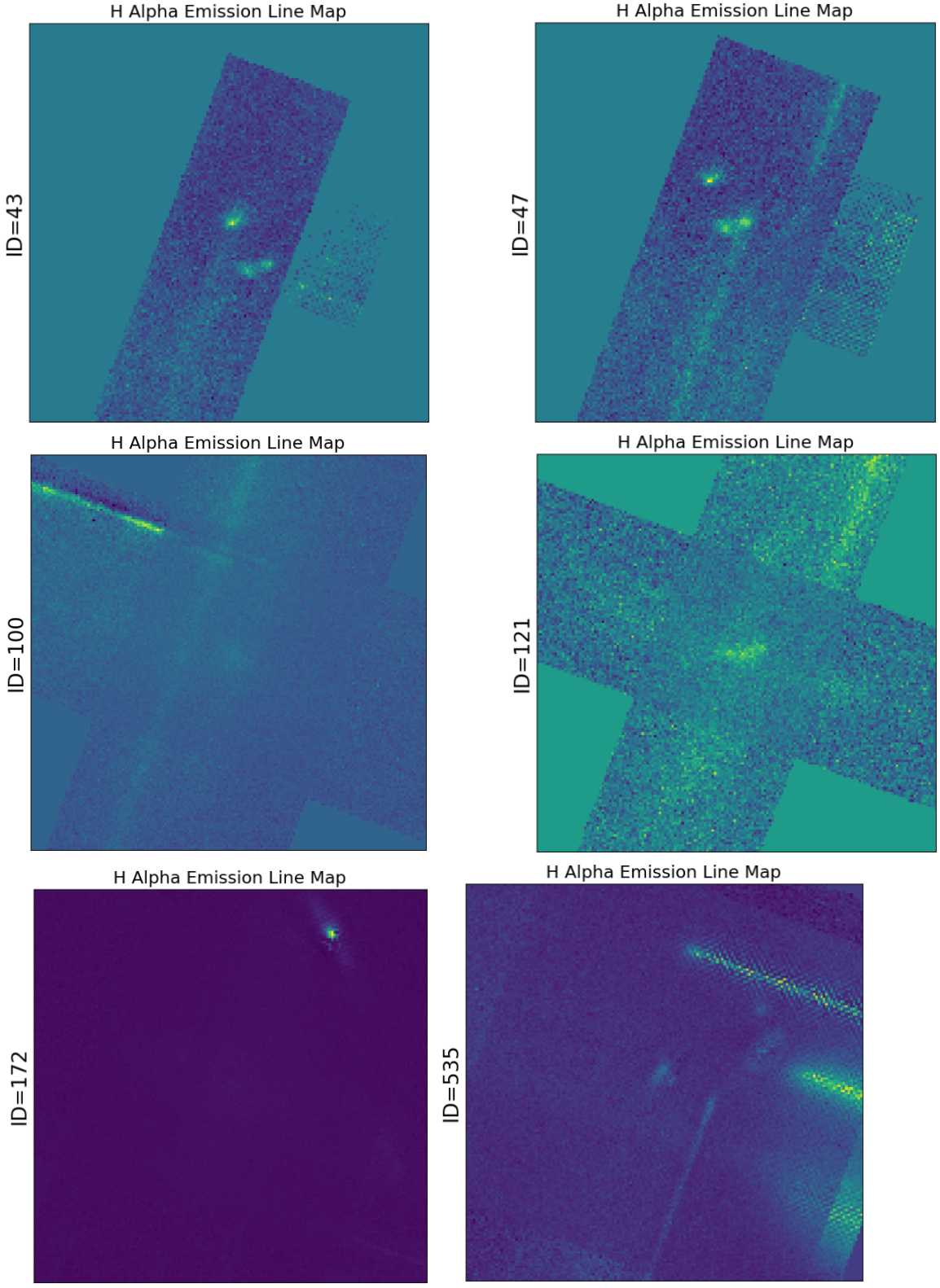
H Alpha Emission Line Map
ID=43
H Alpha Emission Line Map
ID=47
H Alpha Emission Line Map
ID=100
H Alpha Emission Line Map
ID=121
H Alpha Emission Line Map
ID=172
H Alpha Emission Line Map
ID=535

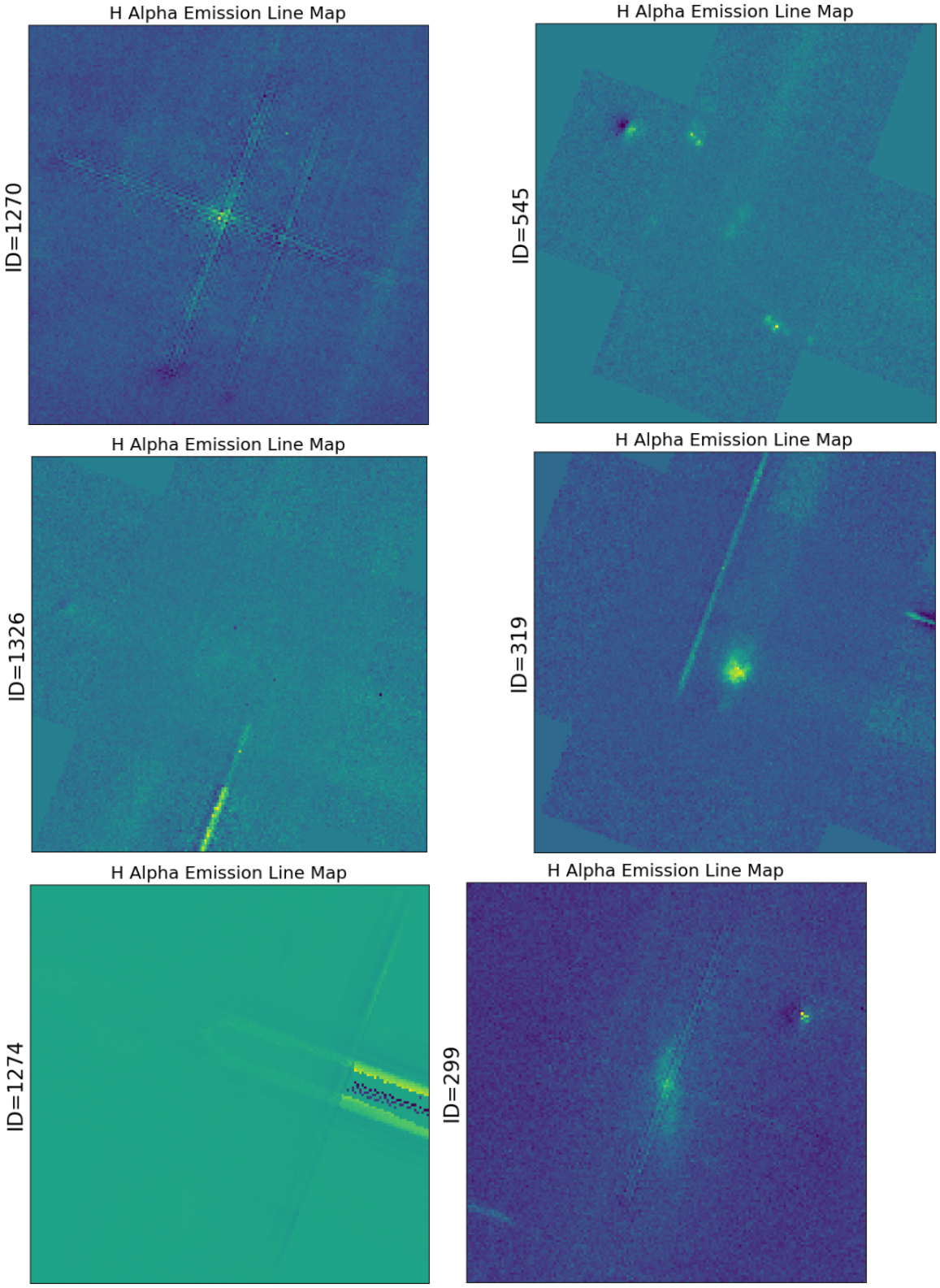
H Alpha Emission Line Map
ID=1270
H Alpha Emission Line Map
ID=545
H Alpha Emission Line Map
ID=1326
H Alpha Emission Line Map
ID=319
H Alpha Emission Line Map
ID=1274
H Alpha Emission Line Map
ID=299

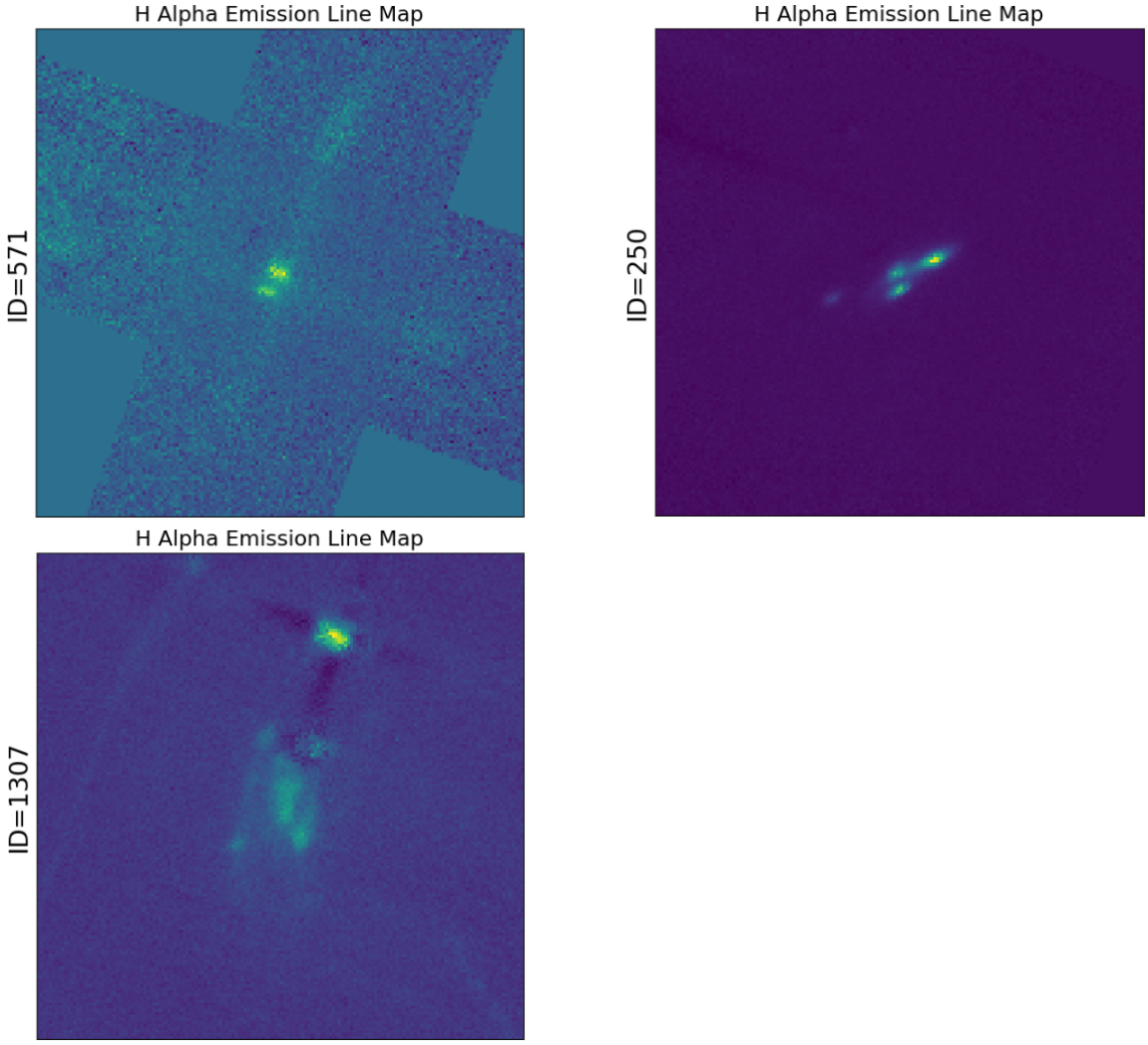
H Alpha Emission Line Map
ID=571
H Alpha Emission Line Map
ID=250
H Alpha Emission Line Map
ID=1307

Appendix F

UV Cutouts and Clump Segmentation Maps - Part One

Spectroscopic Sample and Controls: MACS0417

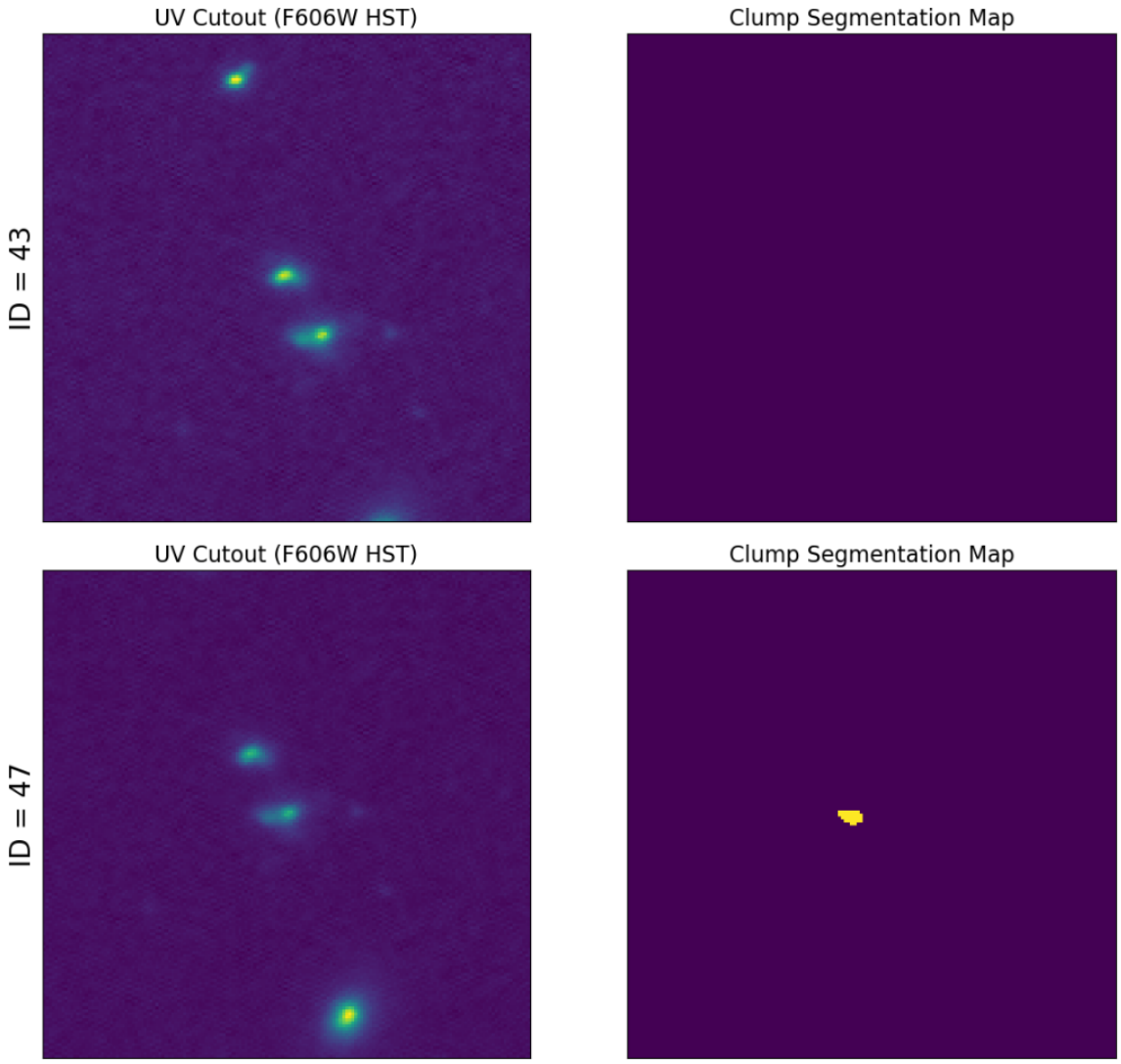
UV Cutout (F606W HST)
Clump Segmentation Map
ID = 43
UV Cutout (F606W HST)
Clump Segmentation Map
ID = 47

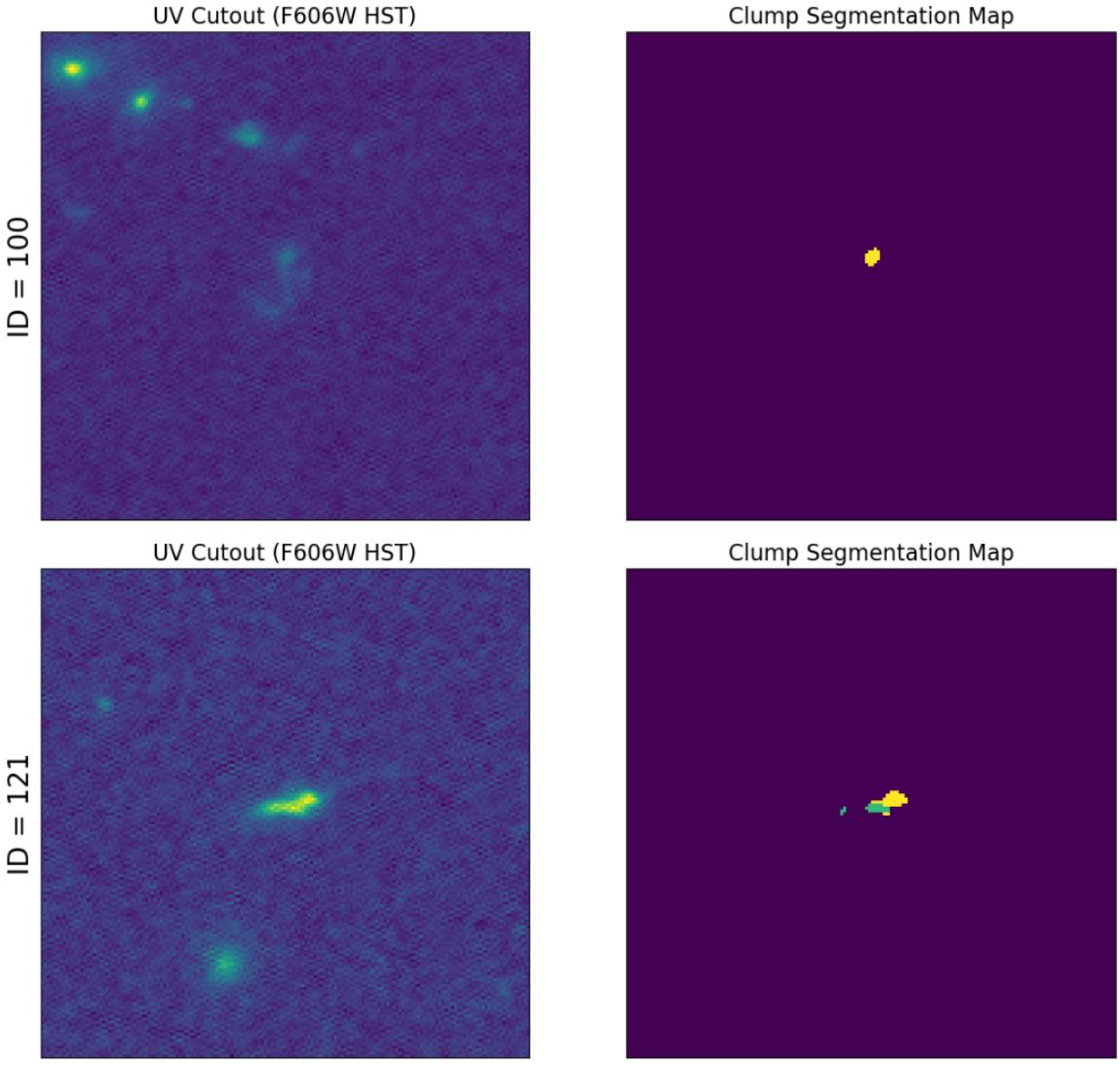
UV Cutout (F606W HST)
Clump Segmentation Map
ID = 100
UV Cutout (F606W HST)
Clump Segmentation Map
ID = 121

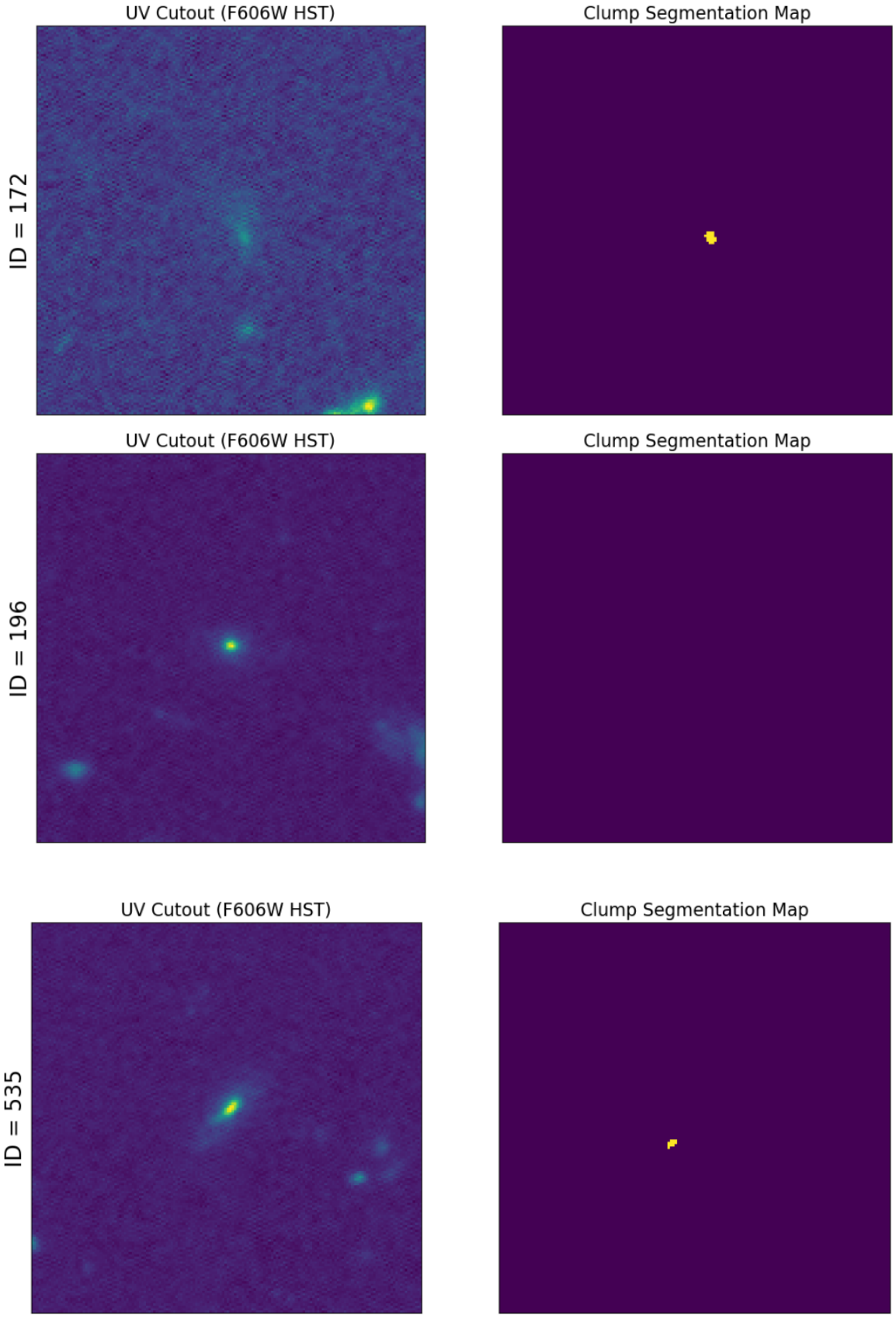
UV Cutout (F606W HST)
Clump Segmentation Map
ID = 172
UV Cutout (F606W HST)
Clump Segmentation Map
ID = 196
UV Cutout (F606W HST)
Clump Segmentation Map
ID = 535

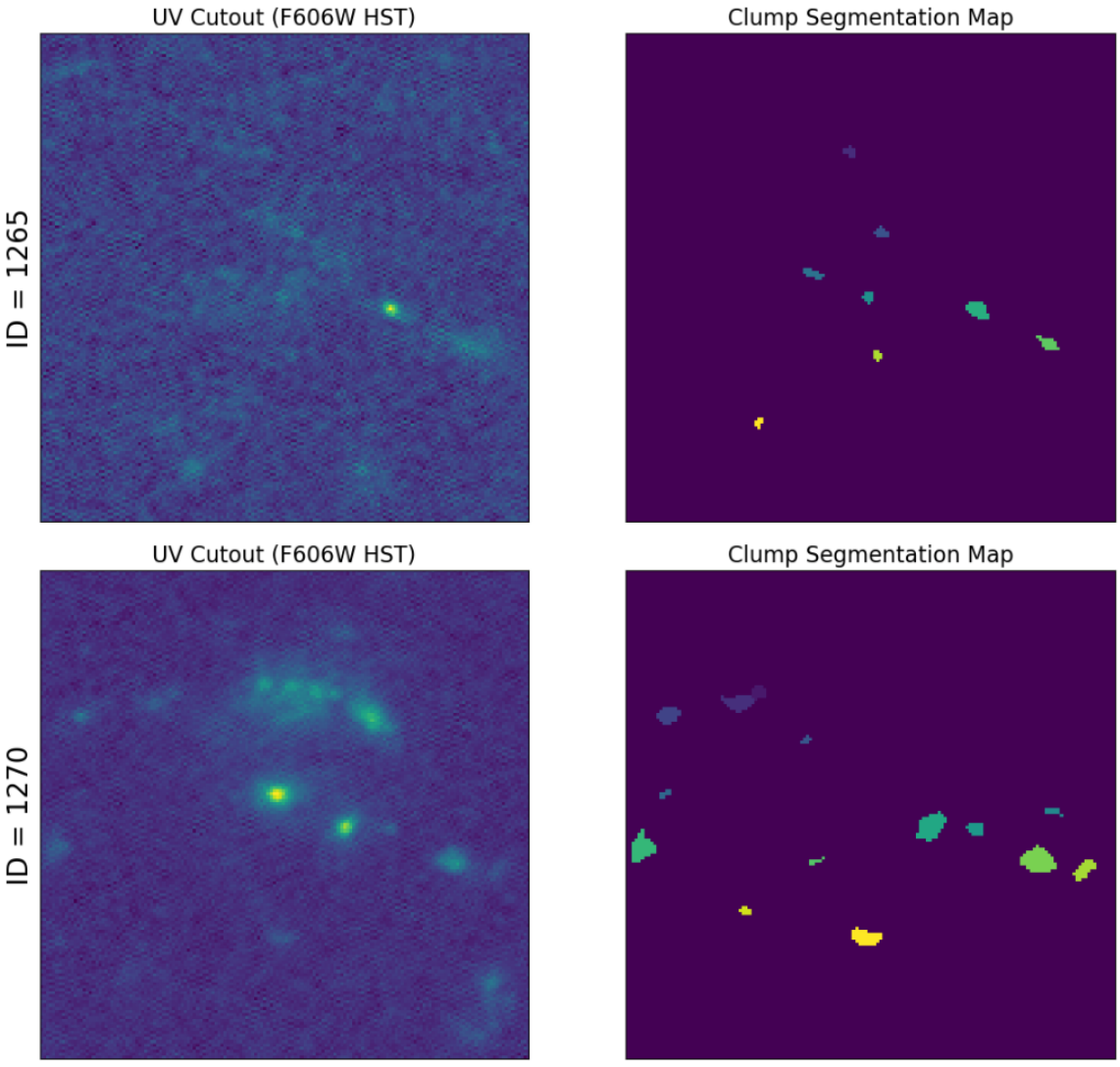
UV Cutout (F606W HST)
Clump Segmentation Map
ID = 1265
UV Cutout (F606W HST)
Clump Segmentation Map
ID = 1270

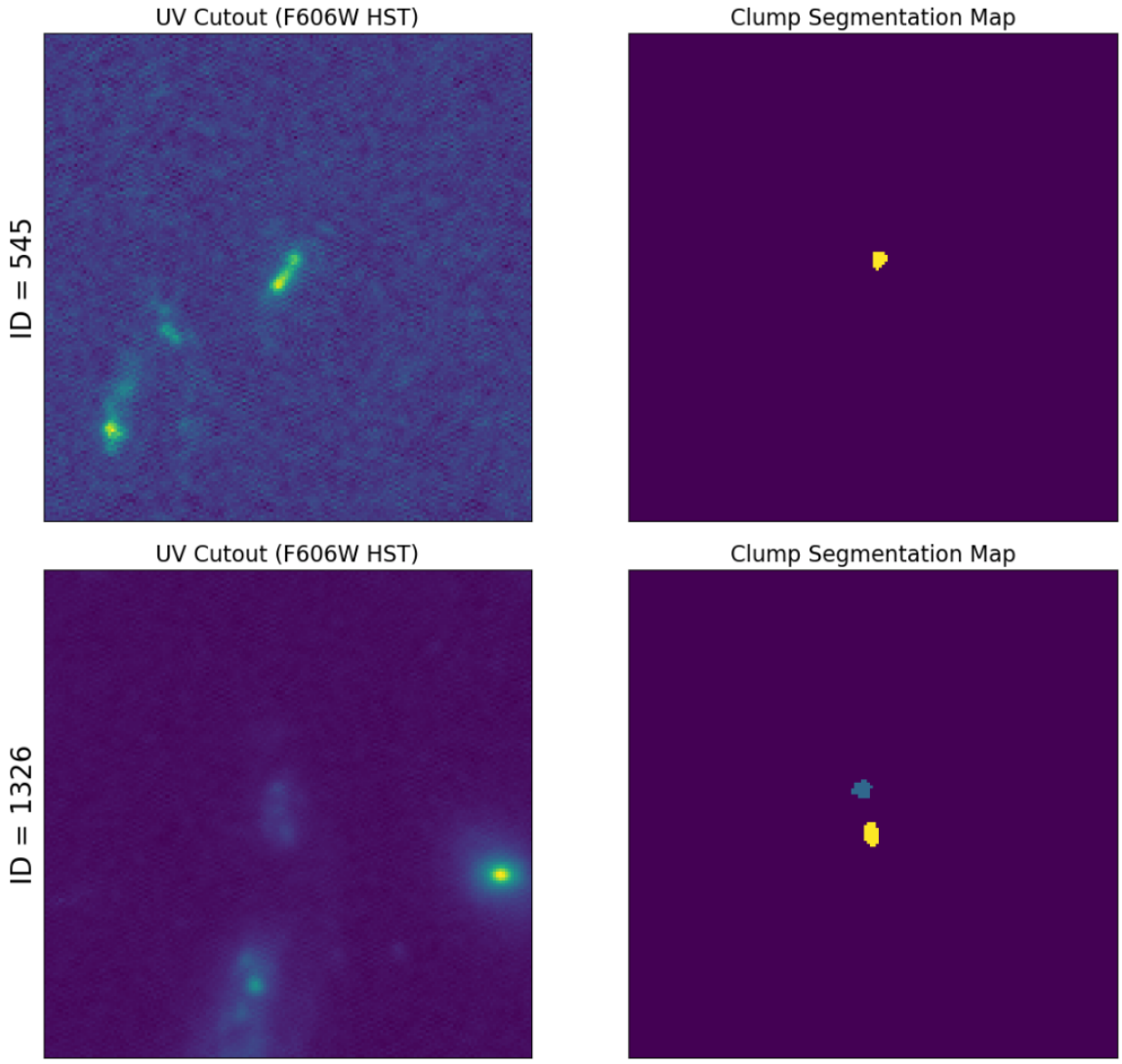
UV Cutout (F606W HST)
Clump Segmentation Map
ID = 545
UV Cutout (F606W HST)
Clump Segmentation Map
ID = 1326

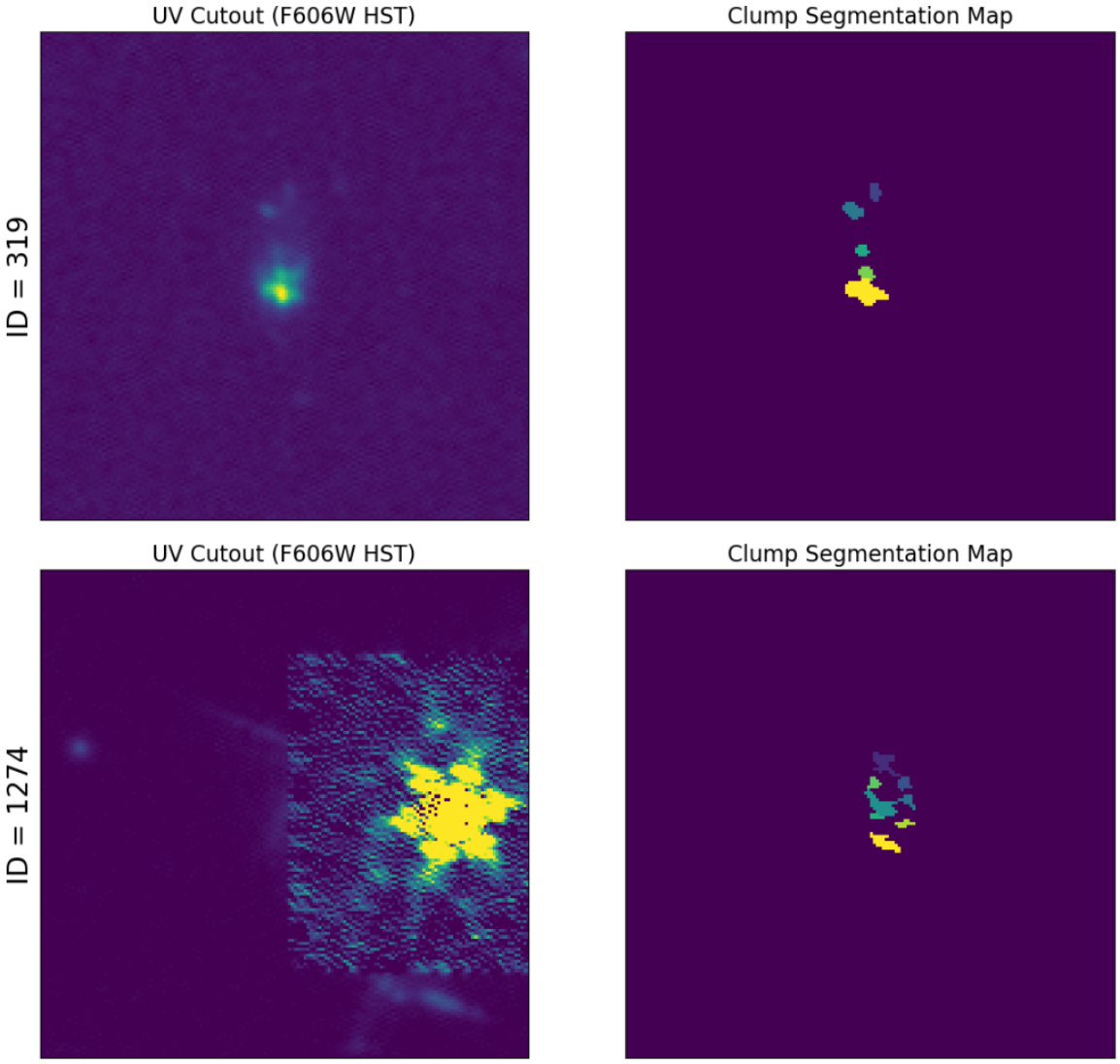
UV Cutout (F606W HST)
Clump Segmentation Map
ID = 319
UV Cutout (F606W HST)
Clump Segmentation Map
ID = 1274

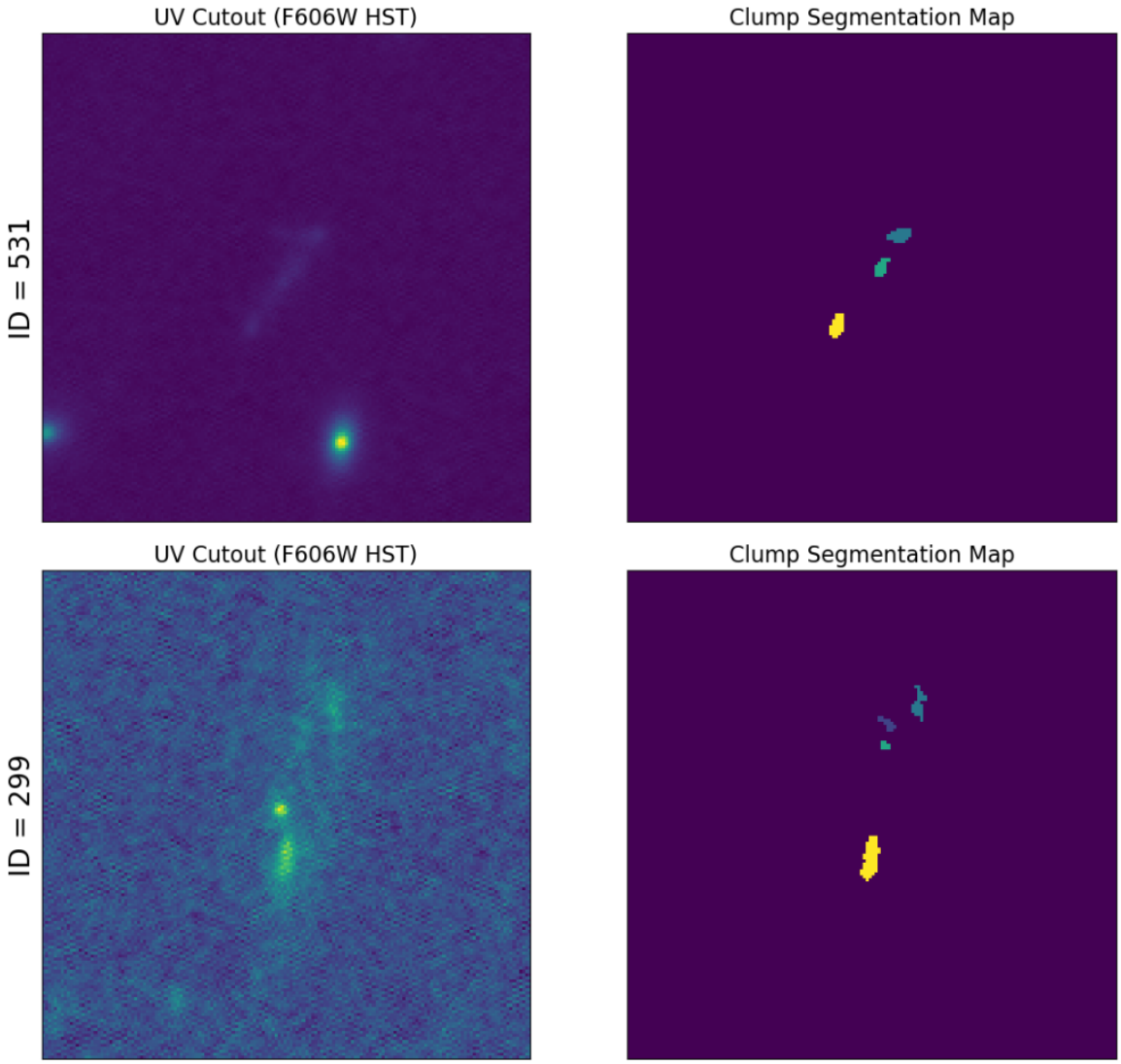
UV Cutout (F606W HST)
Clump Segmentation Map
ID = 531
UV Cutout (F606W HST)
Clump Segmentation Map
ID = 299

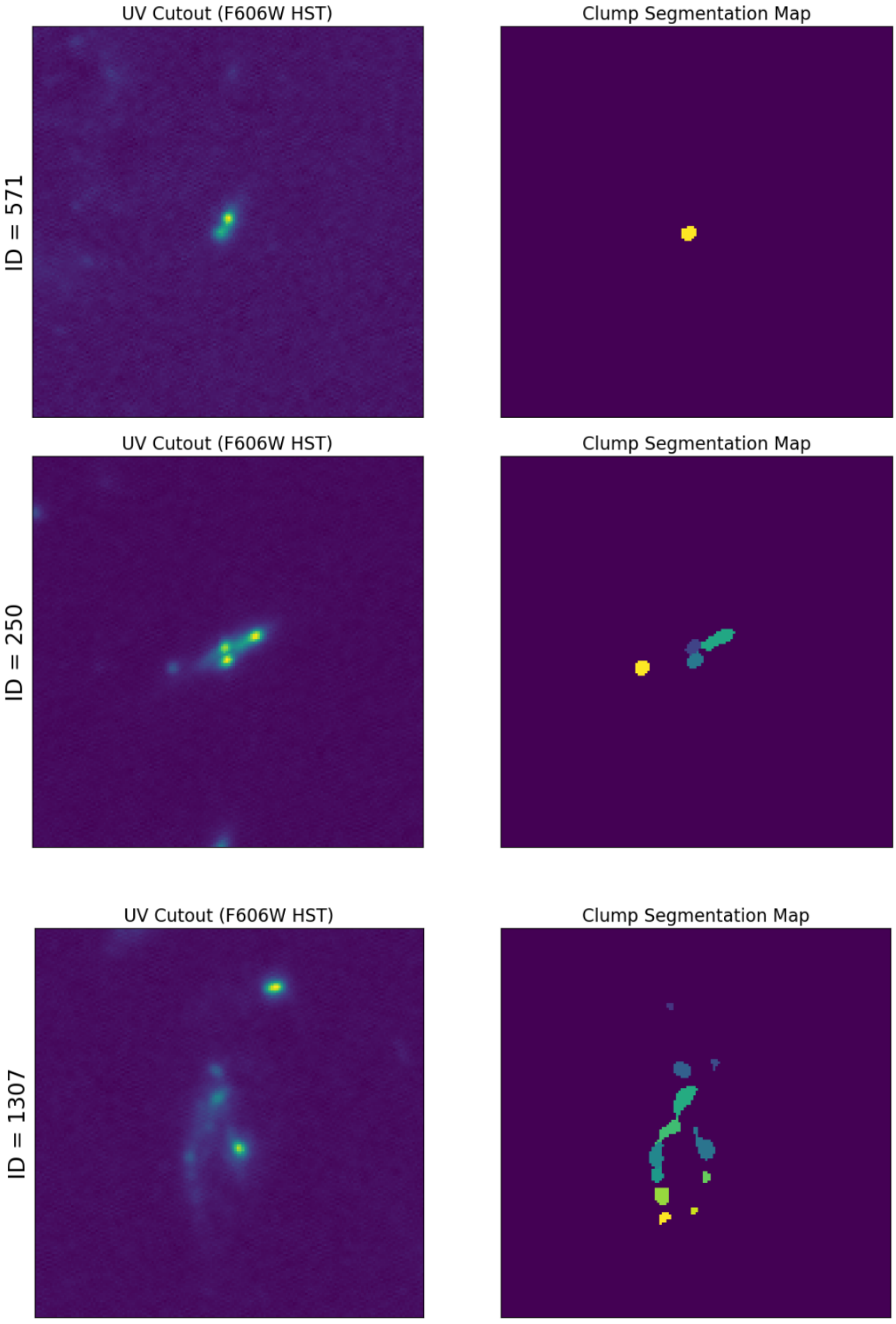
UV Cutout (F606W HST)
Clump Segmentation Map
ID = 571
UV Cutout (F606W HST)
Clump Segmentation Map
ID = 250
UV Cutout (F606W HST)
Clump Segmentation Map
ID = 1307

Appendix G

UV Cutouts and Clump Segmentation Maps - Part Two

Photometric Sample and Controls: MACS0417

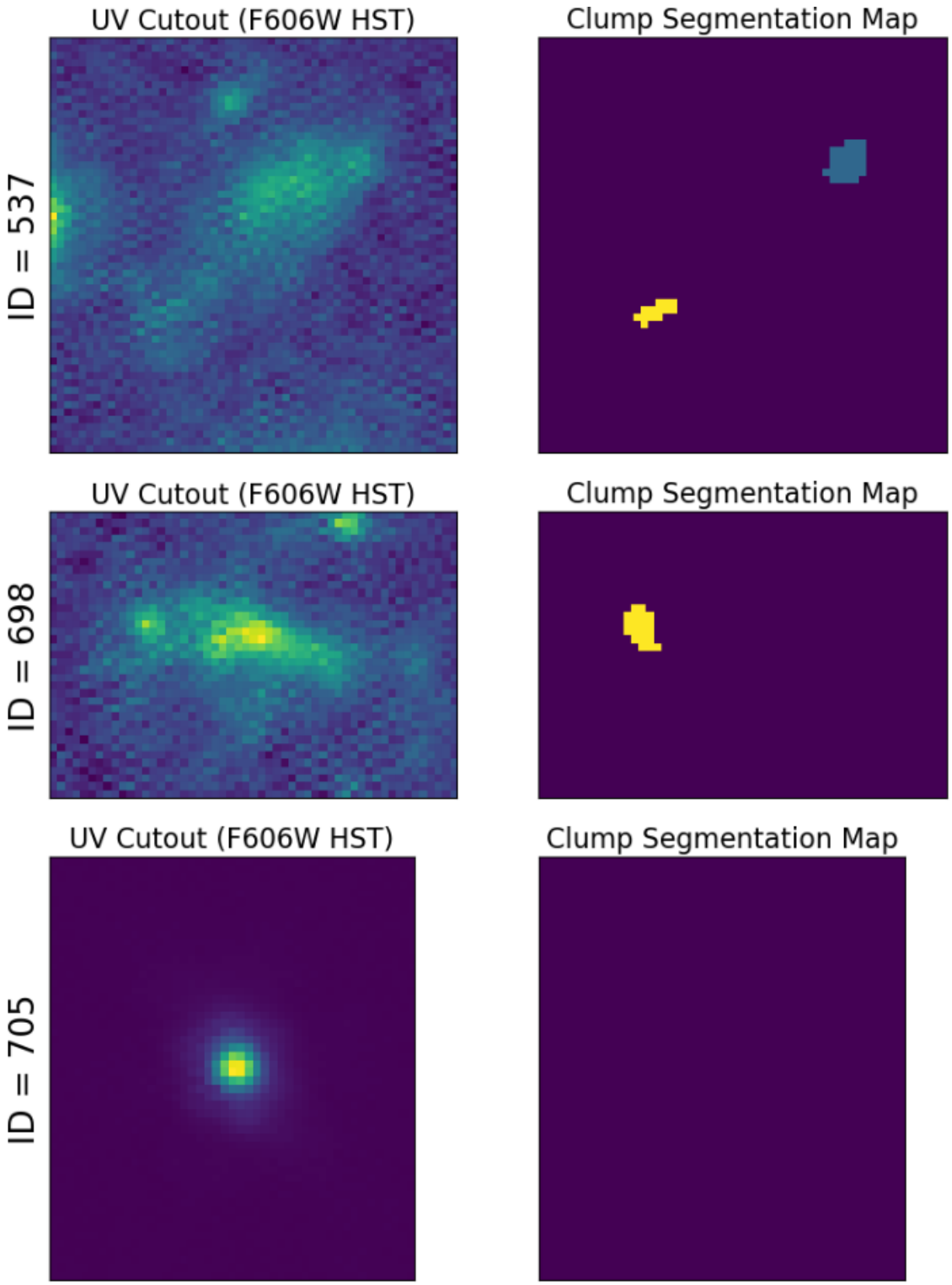
UV Cutout (F606W HST)
Clump Segmentation Map
ID = 537
UV Cutout (F606W HST)
Clump Segmentation Map
ID = 698
UV Cutout (F606W HST)
Clump Segmentation Map
ID = 705

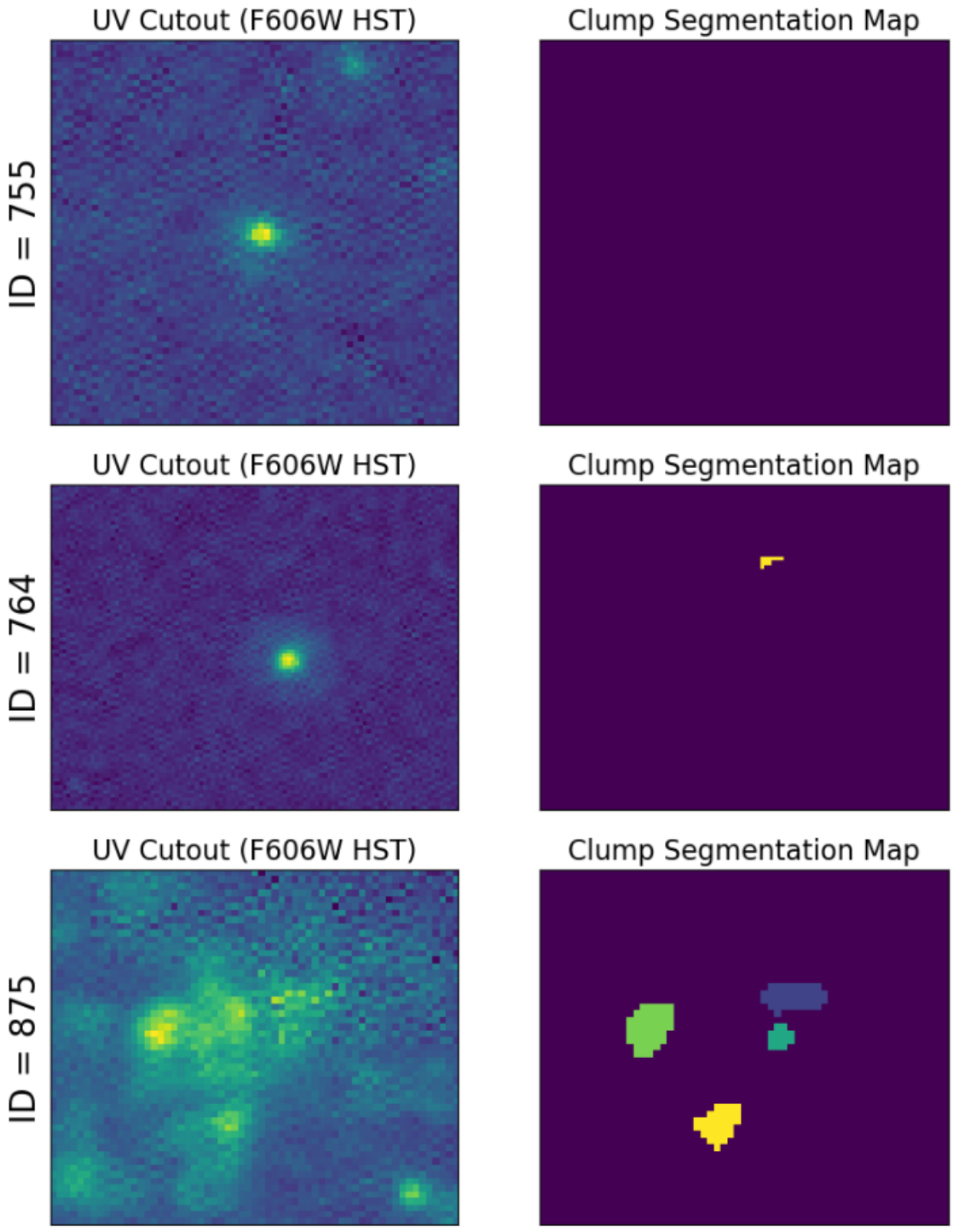
UV Cutout (F606W HST)
Clump Segmentation Map
ID = 755
UV Cutout (F606W HST)
Clump Segmentation Map
ID = 764
UV Cutout (F606W HST)
Clump Segmentation Map
ID = 875

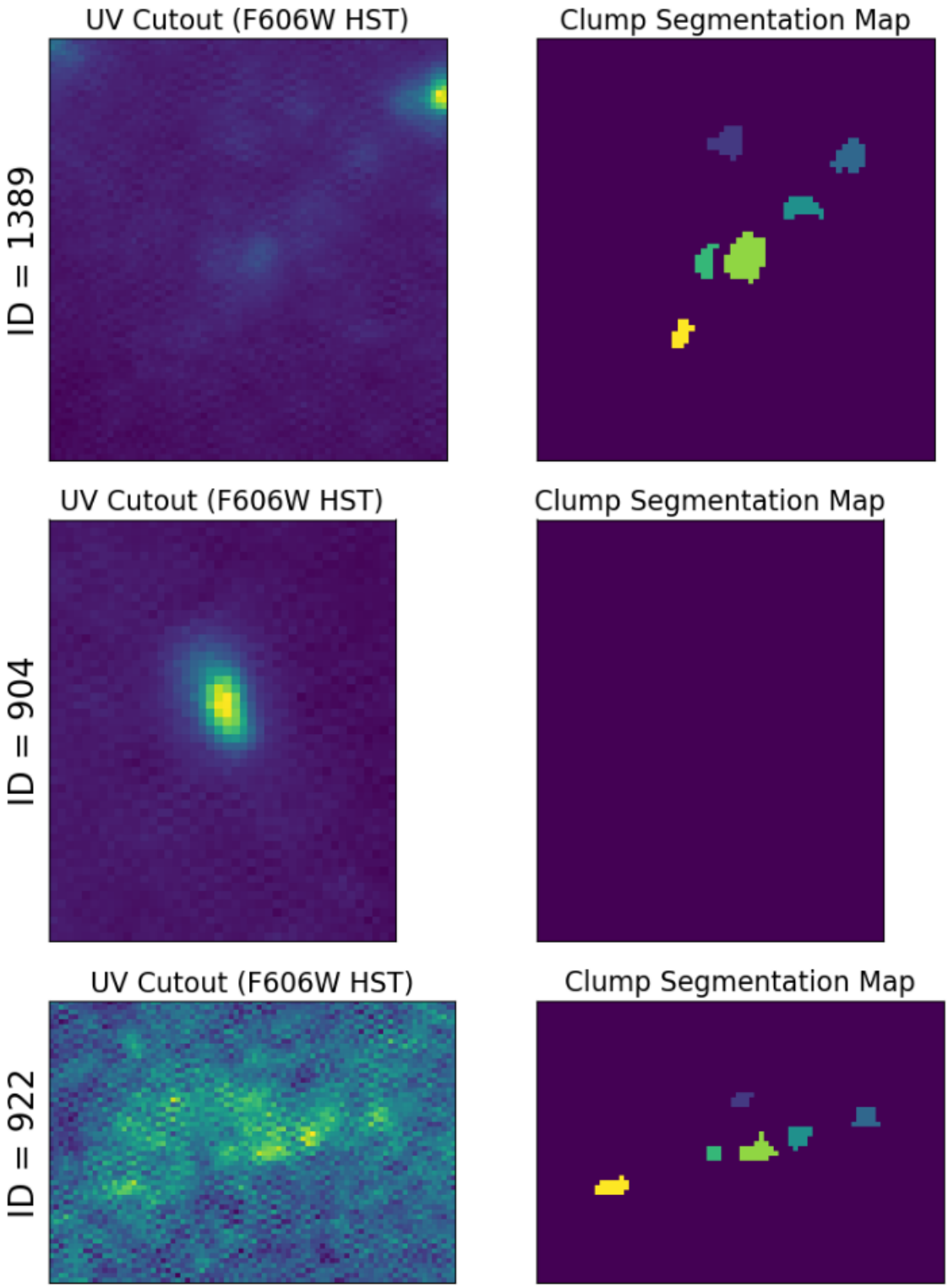
UV Cutout (F606W HST)
Clump Segmentation Map
ID = 1389
UV Cutout (F606W HST)
Clump Segmentation Map
ID = 904
UV Cutout (F606W HST)
Clump Segmentation Map
ID = 922

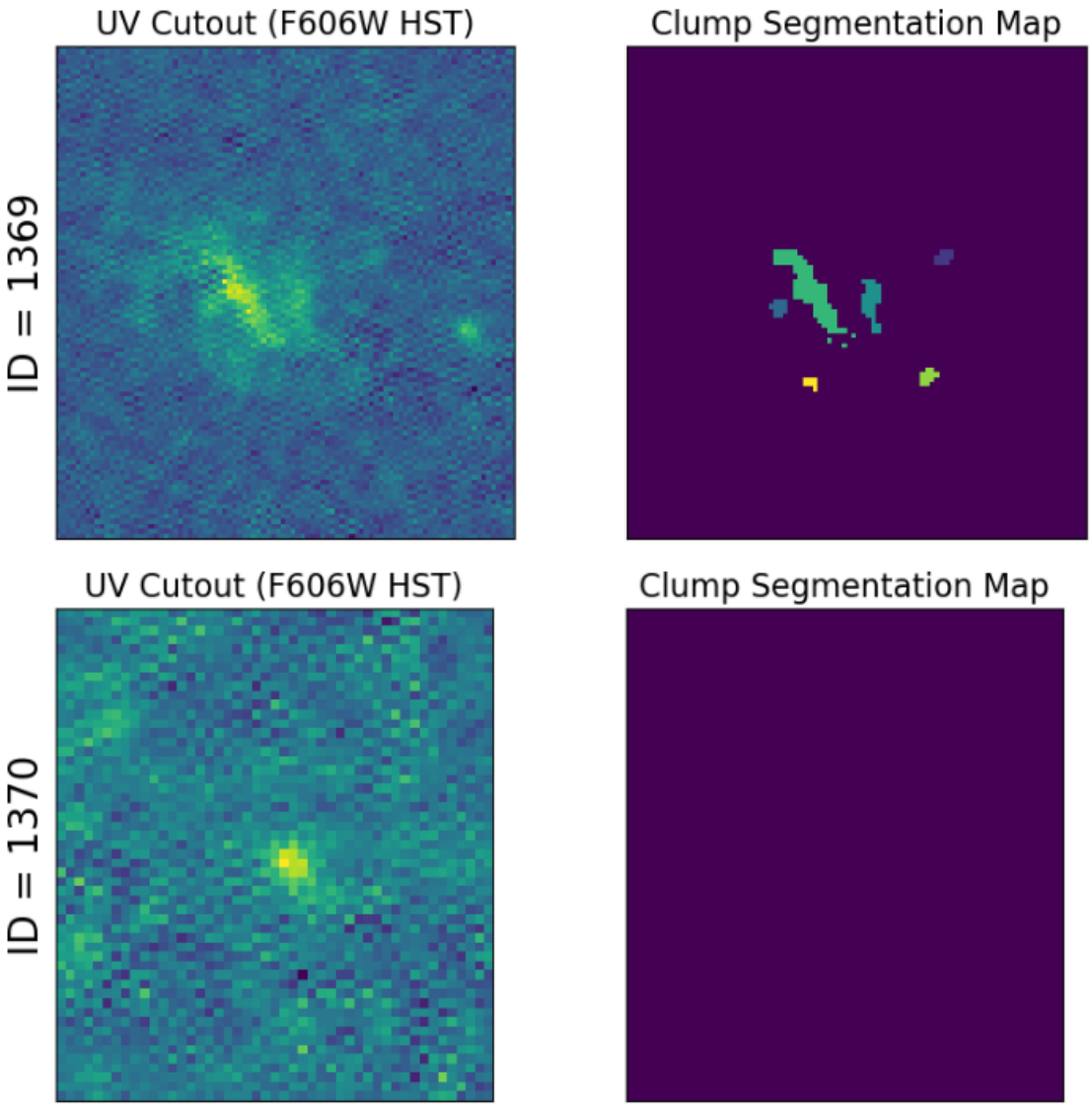
UV Cutout (F606W HST)
Clump Segmentation Map
ID = 1369
UV Cutout (F606W HST)
Clump Segmentation Map
ID = 1370

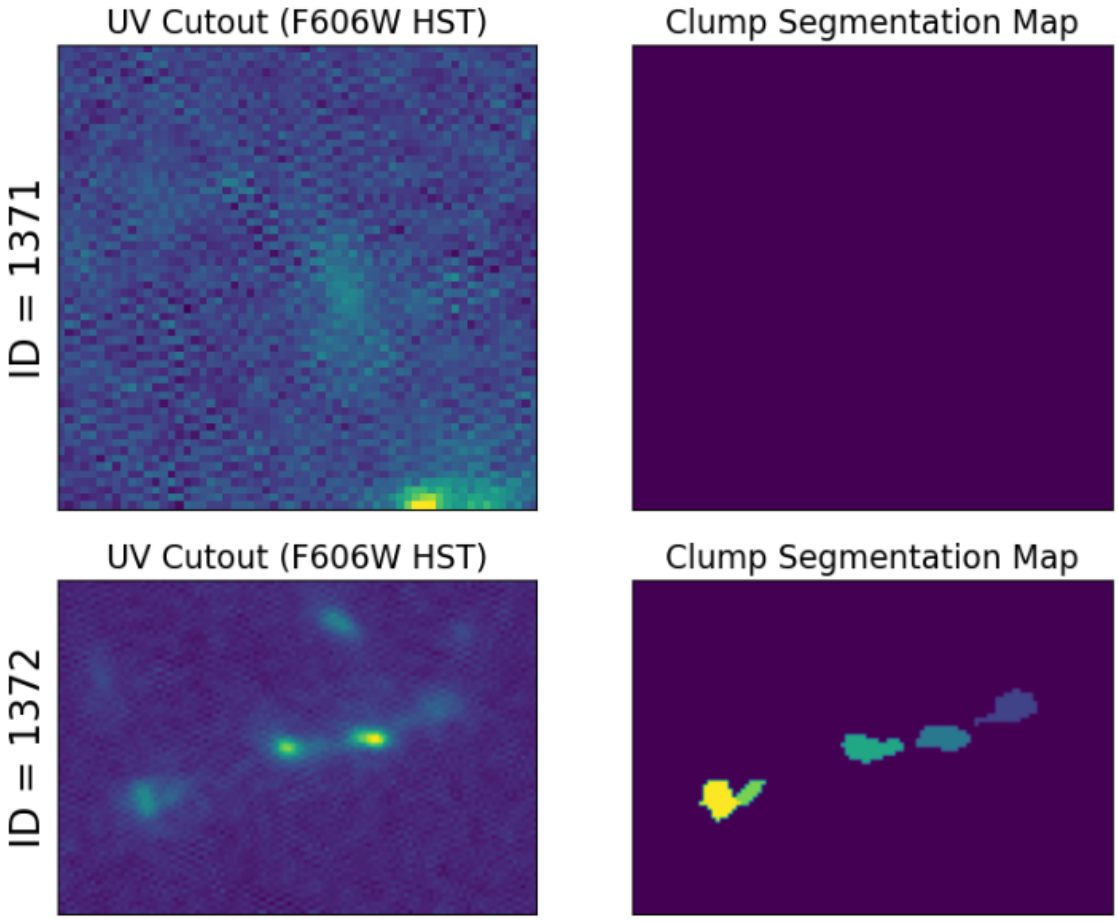
UV Cutout (F606W HST)
Clump Segmentation Map
ID = 1371
UV Cutout (F606W HST)
Clump Segmentation Map
ID = 1372

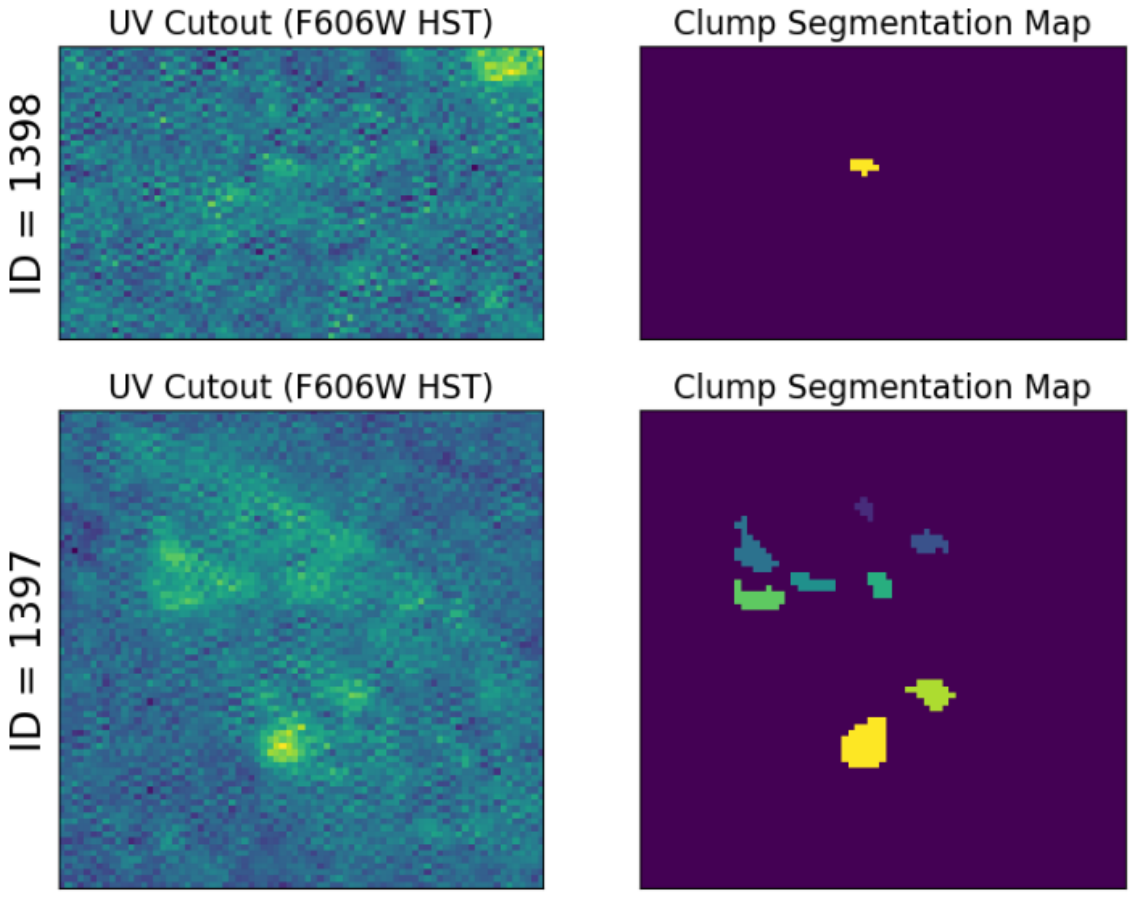
UV Cutout (F606W HST)
Clump Segmentation Map
ID = 1398
UV Cutout (F606W HST)
Clump Segmentation Map
ID = 1397

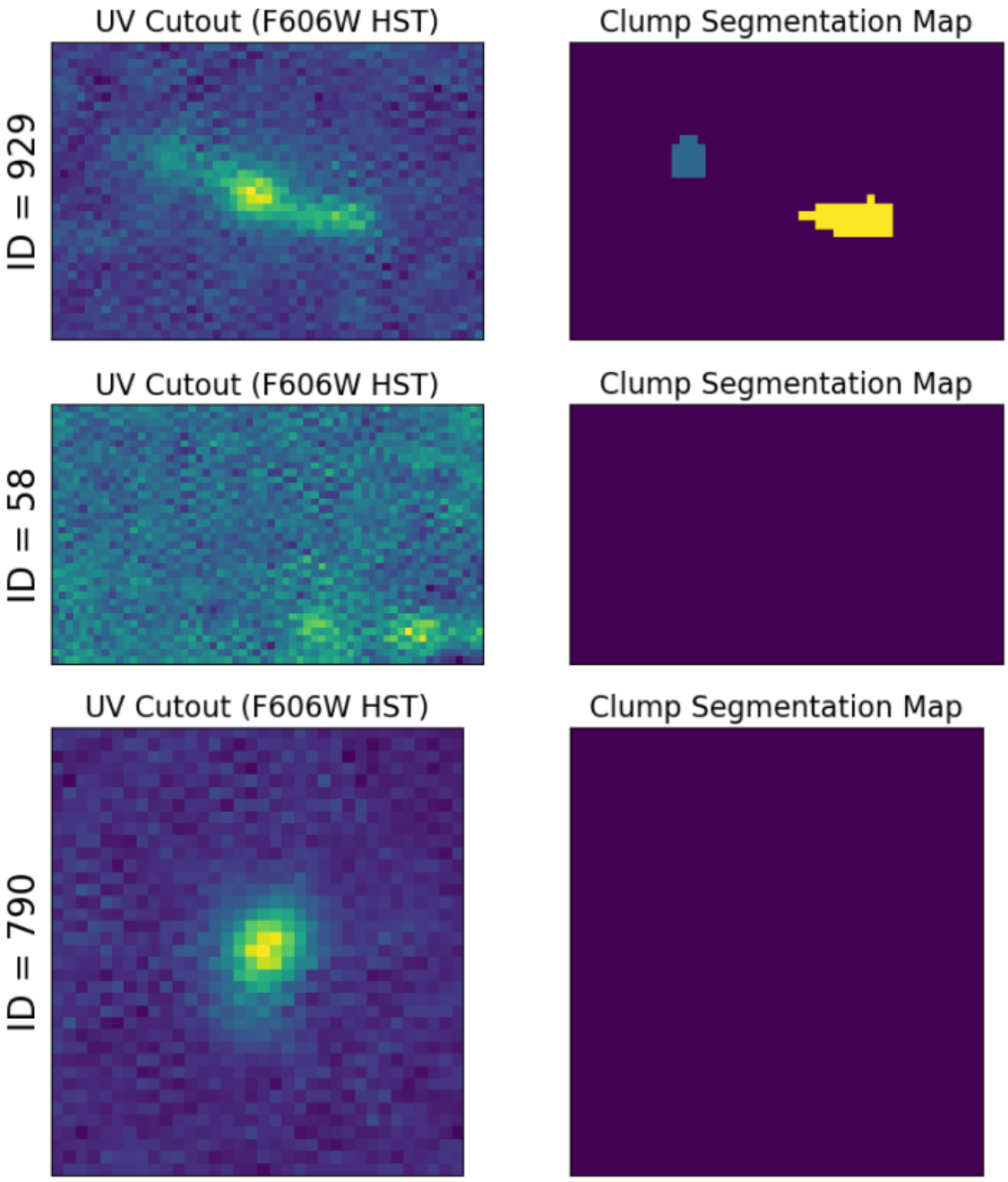
UV Cutout (F606W HST)
Clump Segmentation Map
ID = 929
UV Cutout (F606W HST)
Clump Segmentation Map
ID = 58
UV Cutout (F606W HST)
Clump Segmentation Map
ID = 790

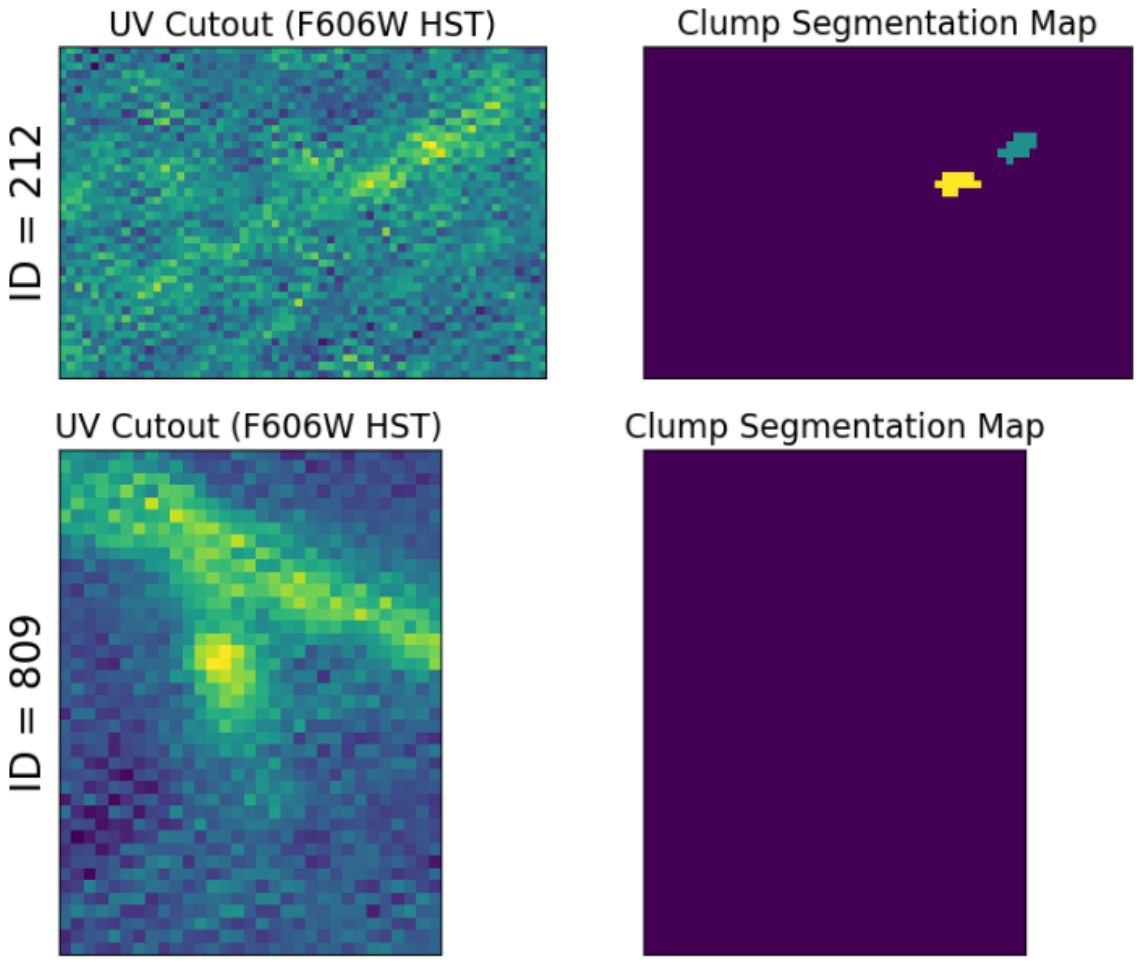
UV Cutout (F606W HST)
Clump Segmentation Map
ID = 212
UV Cutout (F606W HST)
Clump Segmentation Map
ID = 809

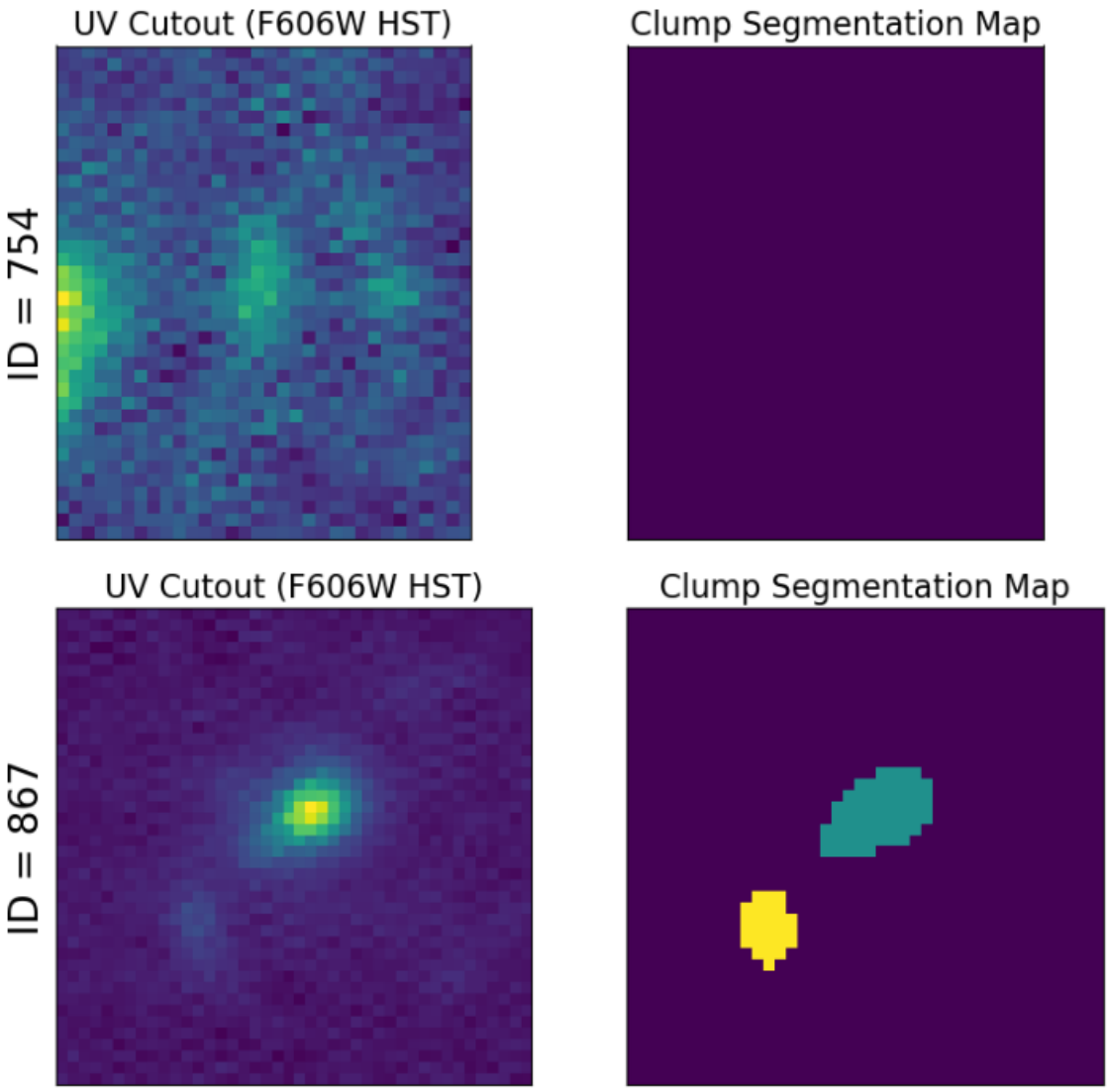
UV Cutout (F606W HST)
Clump Segmentation Map
ID = 754
UV Cutout (F606W HST)
Clump Segmentation Map
ID = 867

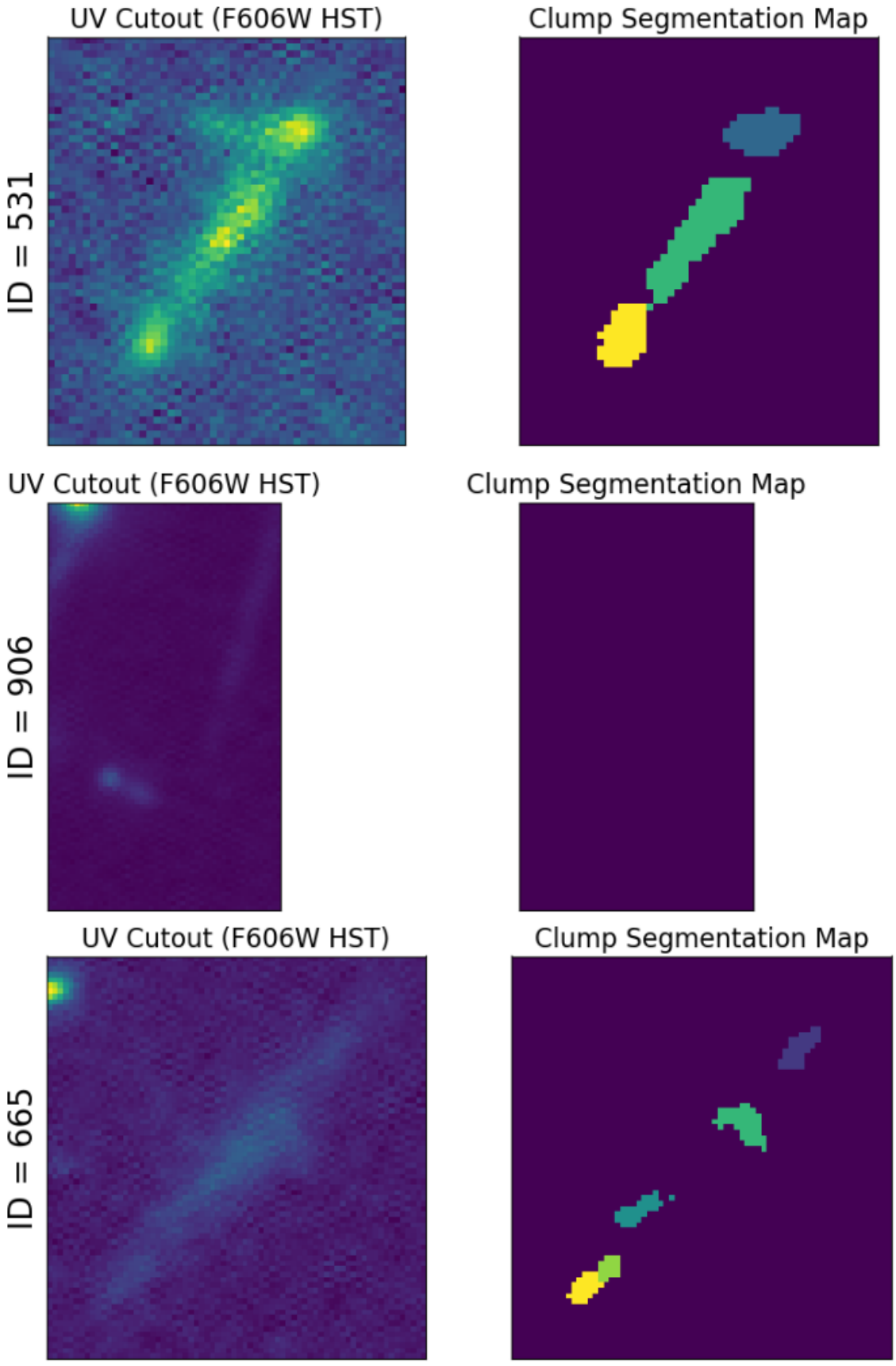
UV Cutout (F606W HST)
Clump Segmentation Map
ID = 531
UV Cutout (F606W HST)
Clump Segmentation Map
ID = 906
UV Cutout (F606W HST)
Clump Segmentation Map
ID = 665

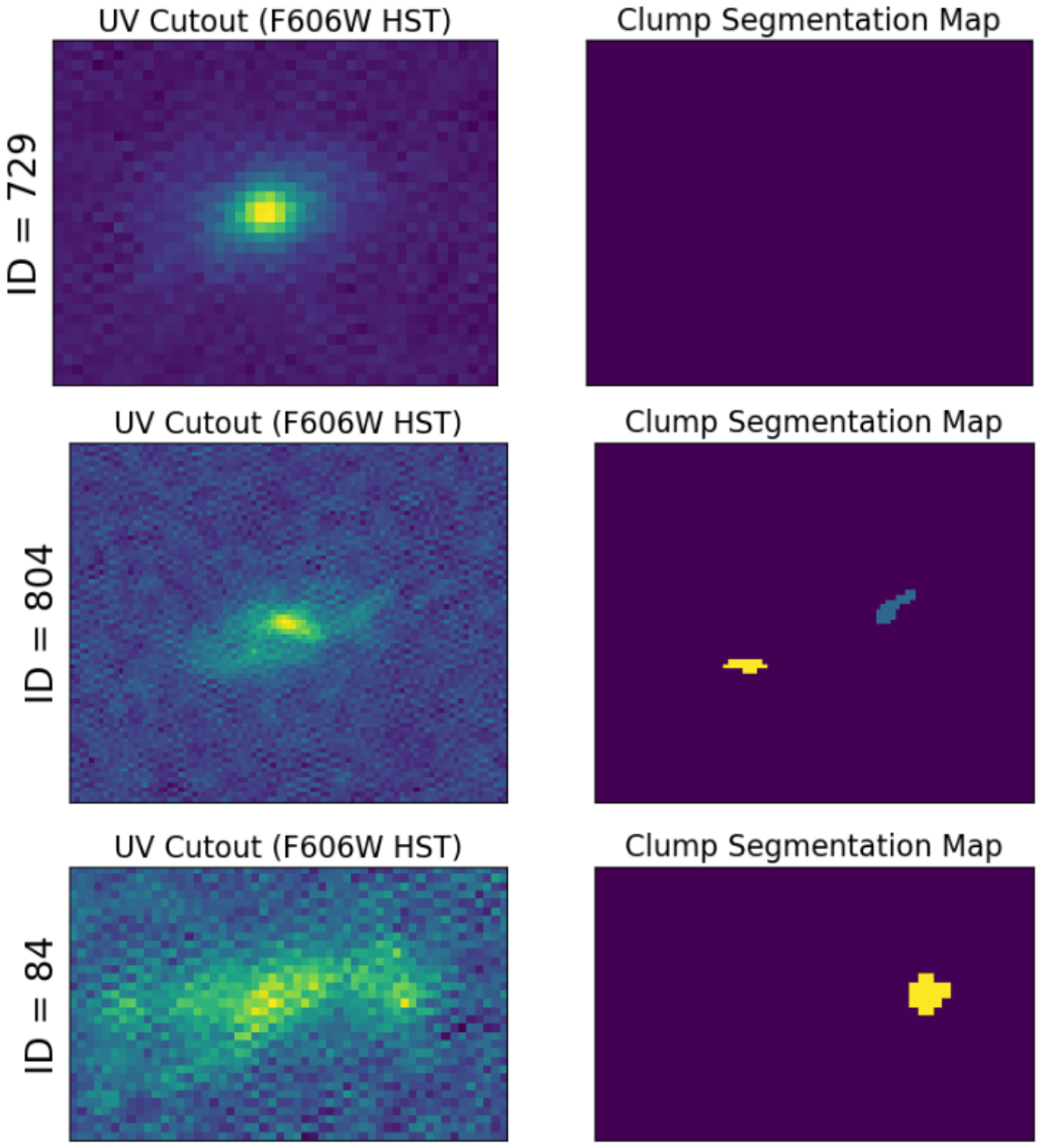
UV Cutout (F606W HST)
Clump Segmentation Map
ID = 729
UV Cutout (F606W HST)
Clump Segmentation Map
ID = 804
UV Cutout (F606W HST)
Clump Segmentation Map
ID = 84

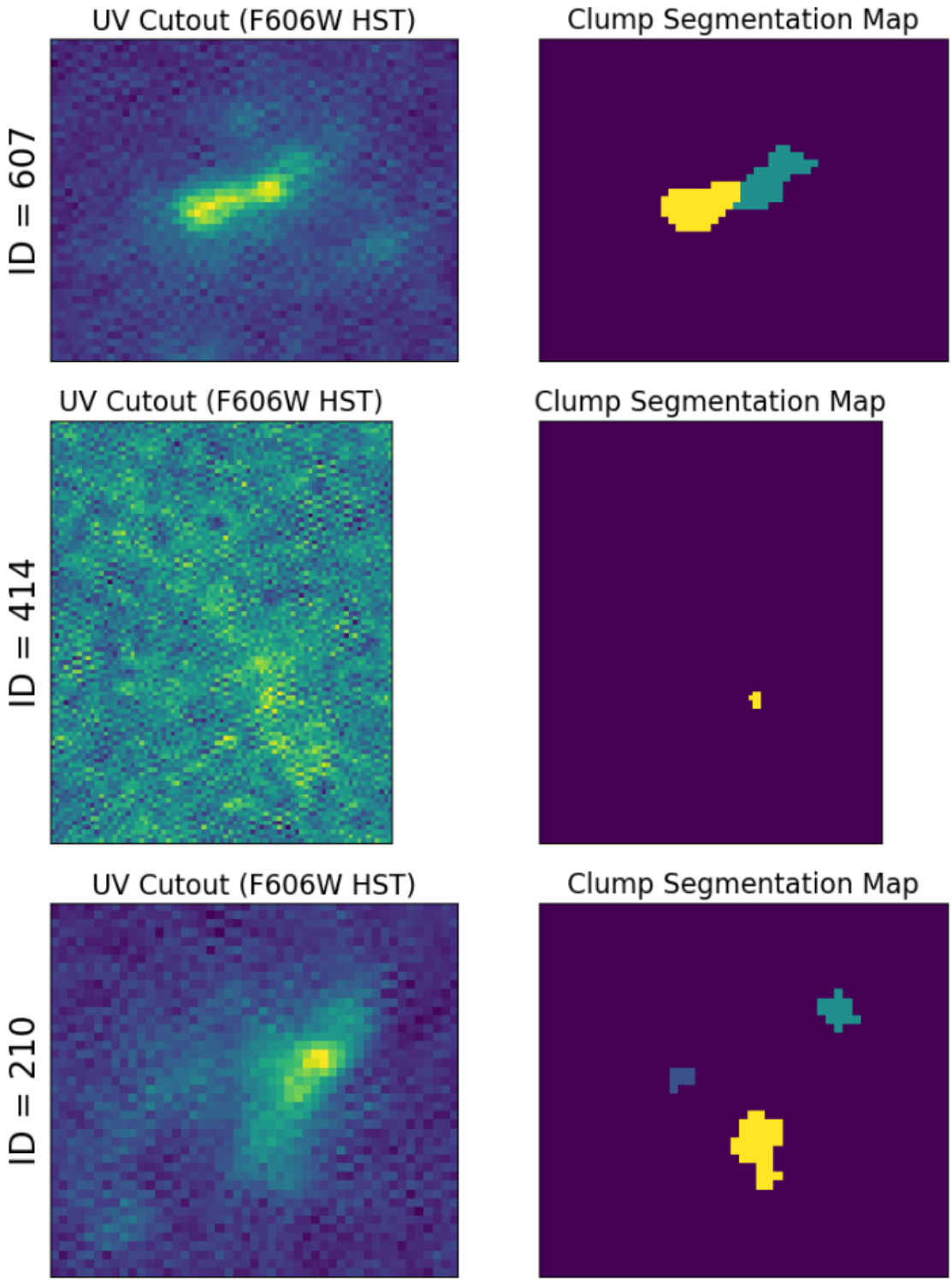
UV Cutout (F606W HST)
Clump Segmentation Map
ID = 607
UV Cutout (F606W HST)
Clump Segmentation Map
ID = 414
UV Cutout (F606W HST)
Clump Segmentation Map
ID = 210

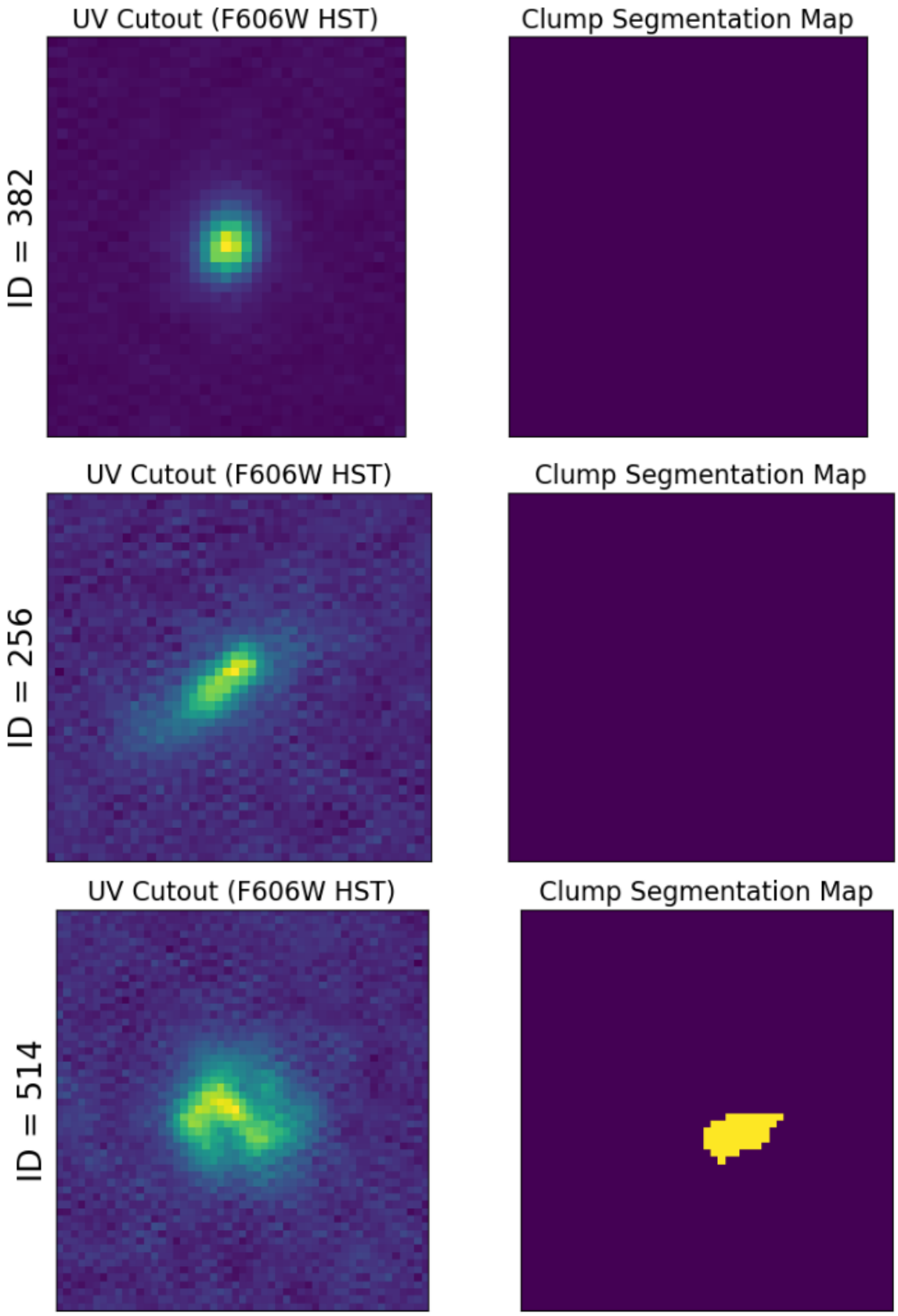
UV Cutout (F606W HST)
Clump Segmentation Map
ID = 382
UV Cutout (F606W HST)
Clump Segmentation Map
ID = 256
UV Cutout (F606W HST)
Clump Segmentation Map
ID = 514

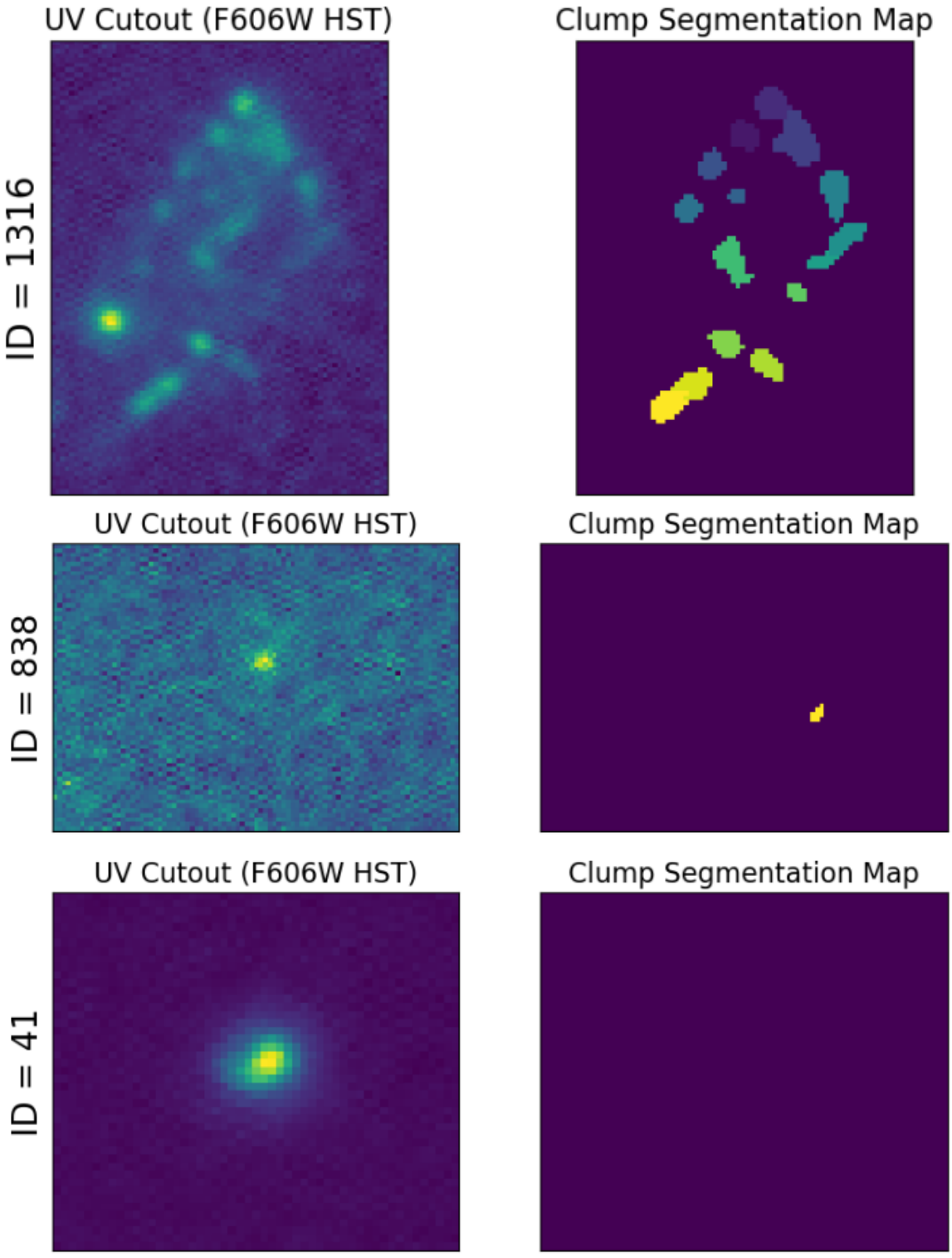
UV Cutout (F606W HST)
Clump Segmentation Map
ID = 1316
UV Cutout (F606W HST)
Clump Segmentation Map
ID = 838
UV Cutout (F606W HST)
Clump Segmentation Map
ID = 41

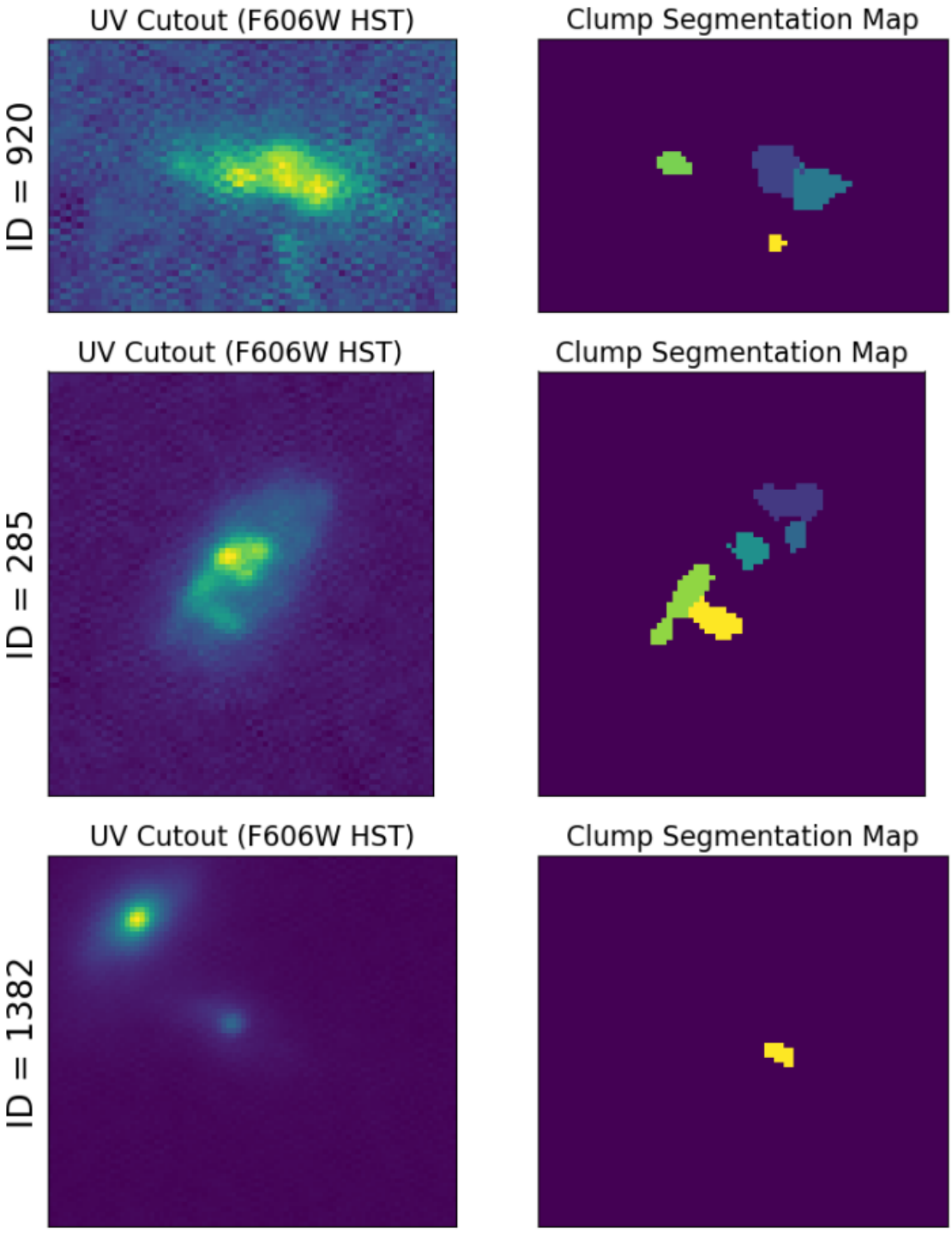
UV Cutout (F606W HST)
Clump Segmentation Map
ID = 920
UV Cutout (F606W HST)
Clump Segmentation Map
ID = 285
UV Cutout (F606W HST)
Clump Segmentation Map
ID = 1382

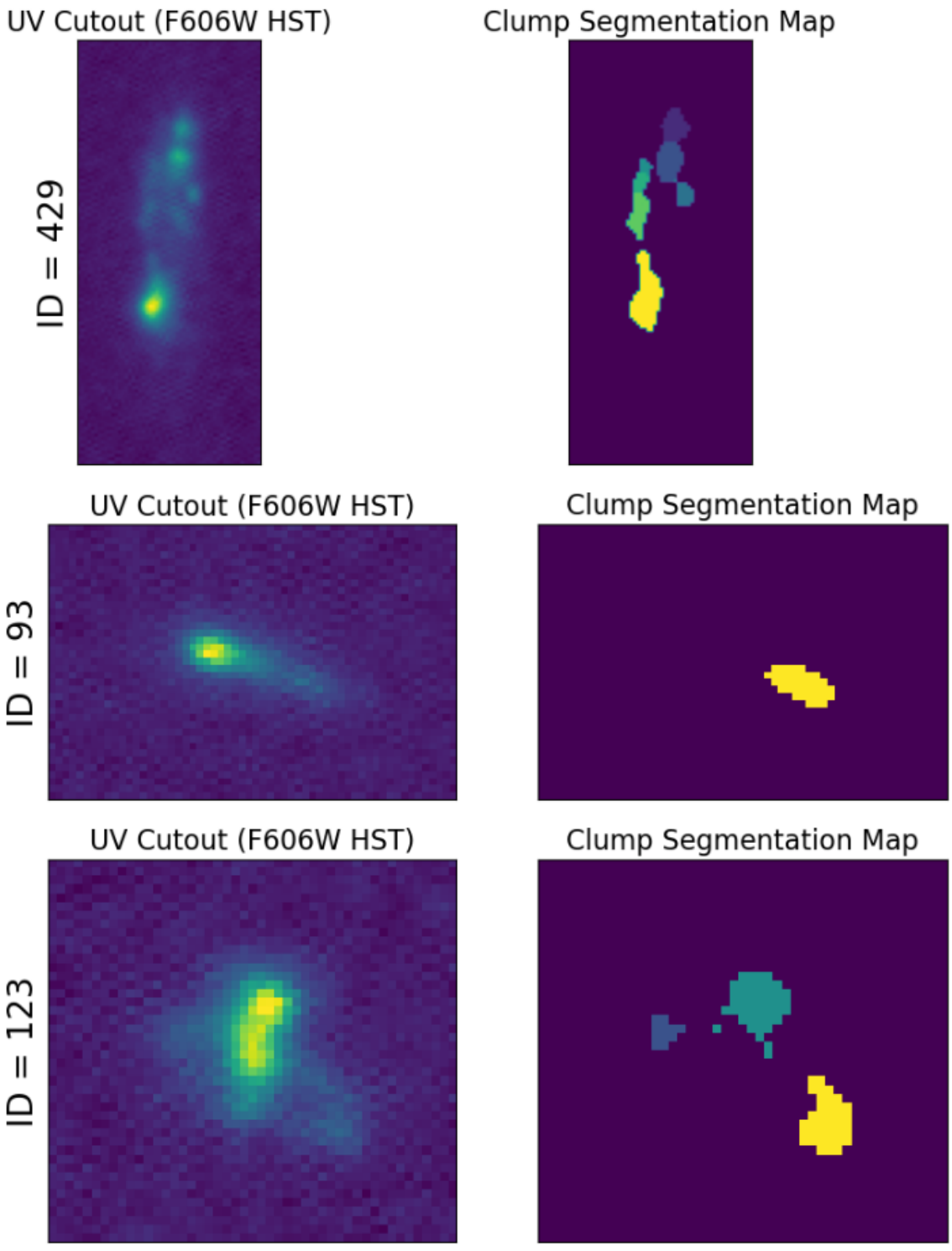
UV Cutout (F606W HST)
Clump Segmentation Map
ID = 429
UV Cutout (F606W HST)
Clump Segmentation Map
ID = 93
UV Cutout (F606W HST)
Clump Segmentation Map
ID = 123

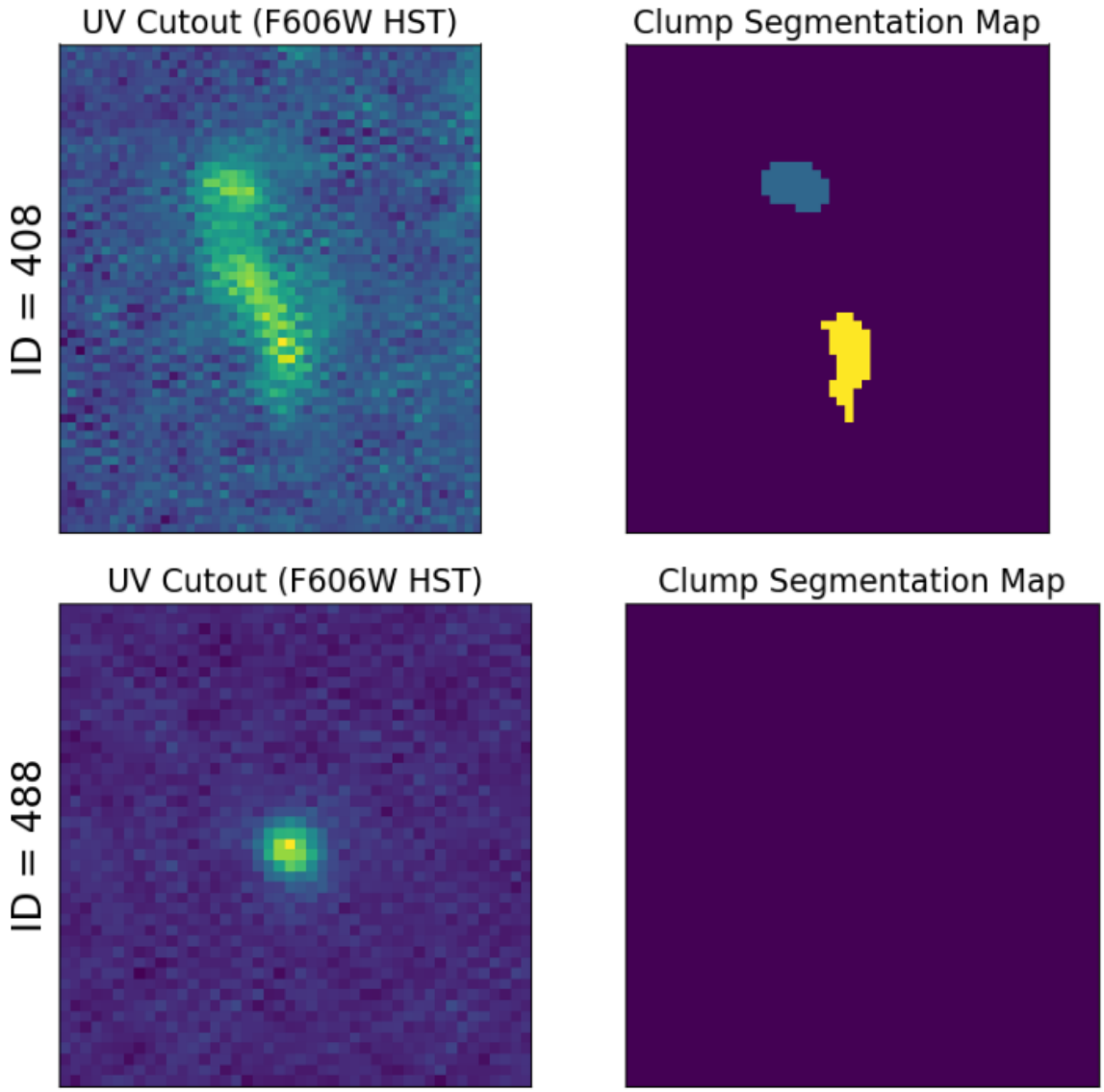
UV Cutout (F606W HST)
Clump Segmentation Map
ID = 408
UV Cutout (F606W HST)
Clump Segmentation Map
ID = 488

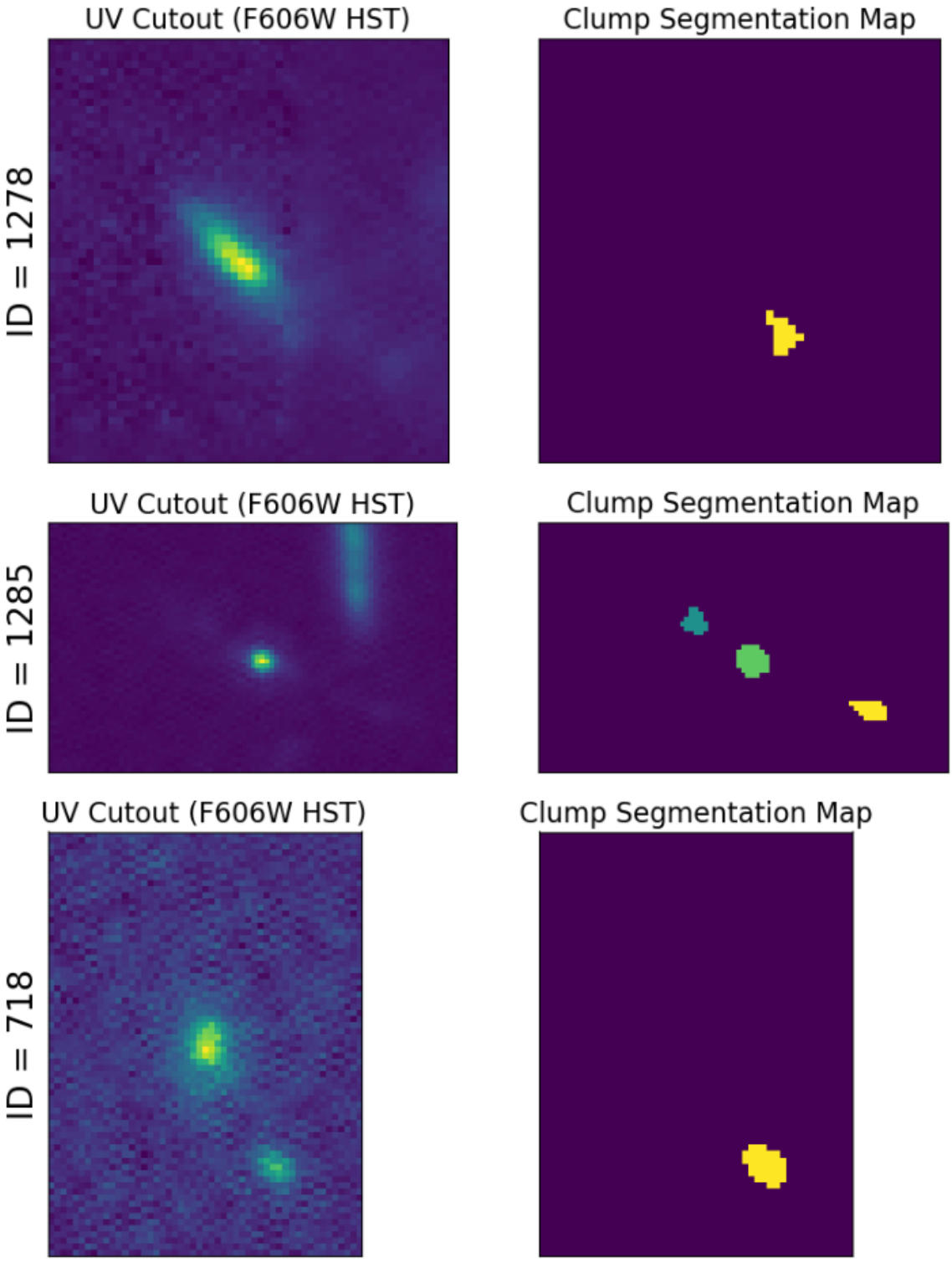
UV Cutout (F606W HST)
Clump Segmentation Map
ID = 1278
UV Cutout (F606W HST)
Clump Segmentation Map
ID = 1285
UV Cutout (F606W HST)
Clump Segmentation Map
ID = 718

Bibliography

Yoshihisa Asada et al. Bursty star formation and galaxy-galaxy interactions in low-mass galaxies 1 gyr after the big bang, 2024.

Astropy Collaboration. The Astropy Project: Sustaining and Growing a Community-oriented Open-source Project and the Latest Major Release (v5.0) of the Core Package. *APJ*, 935(2):167, August 2022.

K. Barbary. SExtractor: Software for source extraction., 2016.

E. Bertin and S. Arnouts. SExtractor: Software for source extraction. *AAPS*, 117: 393–404, June 1996.

Gabriel B. Brammer, Pieter G. van Dokkum, and Paolo Coppi. EAZY: A Fast, Public Photometric Redshift Code. Astrophysics Source Code Library, record ascl:1010.052, October 2010.

Daniela Calzetti. The Dust Opacity of Star-forming Galaxies. *PASP*, 113(790): 1449–1485, December 2001.

J. J. Condon and A. M. Matthews. ΛCDM Cosmology for Astronomers. *PASP*, 130 (989):073001, July 2018.

Charlie Conroy. Modeling the Panchromatic Spectral Energy Distributions of Galaxies. *ARAA*, 51(1):393–455, August 2013.

Emma Curtis-Lake et al. Spectroscopic confirmation of four metal-poor galaxies at z=10.3–13.2. *Nature Astronomy*, 2023.

L. Divan. Interstellar reddening law and spectral classification. *AAP*, 12:76, April 1971.

René Doyon et al. The Near Infrared Imager and Slitless Spectrograph for the James Webb Space Telescope. I. Instrument Overview and In-flight Performance. , 135(1051):098001, September 2023.

Sara L. Ellison et al. Galaxy pairs in the sloan digital sky survey. i. star formation, active galactic nucleus fraction, and the luminosity/mass–metallicity relation. *The Astronomical Journal*, 2008.

Bruce G. Elmegreen and Debra M. Elmegreen. Stellar Populations in 10 Clump-Cluster Galaxies of the Hubble Ultra Deep Field. *AJ*, pages 627–632, 2005.

V. Estrada-Carpenter et al. When, where, and how star formation happens in a galaxy pair at cosmic noon using canucs jwst/niriss grism spectroscopy. *Submitted to Monthly Notices of the Royal Astronomical Society*, 2023.

Vicente Estrada-Carpenter. Clump metallicites from grism spectroscopy. *In preparation*, 2024.

Vicente Estrada-Carpenter et al. Clear. i. ages and metallicities of quiescent galaxies at 1.0 lt; z lt; 1.8 derived from deep hubble space telescope grism data. *The Astrophysical Journal*, 870(2):133, jan 2019.

Jonathan P. Gardner et al. The James Webb Space Telescope Mission. , 135(1048): 068001, June 2023.

Rachel Gledhill et al. Canucs: An updated mass and magnification model of abell 370 with jwst, 2024.

Y. Guo et al. Clumpy galaxies in CANDELS. I. The definition of UV clumps and the fraction of clumpy galaxies at $0.5 < z < 3$. *APJ*, 800(1):39, February 2015.

Yicheng Guo et al. The bursty star formation histories of low-mass galaxies at 0.4 lt; z lt; 1 revealed by star formation rates measured from h and fuv. *The Astrophysical Journal*, 833(1):37, dec 2016.

J. Iglesias-Páramo et al. Tracing the star formation history of cluster galaxies using the h/uv flux ratio*. *AA*, 421(3):887–897, 2004.

Shuichiro Inutsuka, Tsuyoshi Inoue, Kazunari Iwasaki, and Takashi Hosokawa. The formation and destruction of molecular clouds and galactic star formation - an origin for the cloud mass function and star formation efficiency. *AA*, 580:A49, 2015.

Kartheik G. Iyer et al. Nonparametric star formation history reconstruction with gaussian processes. i. counting major episodes of star formation. *The Astrophysical Journal*, 879(2):116, jul 2019.

Mark H. Jones, Robert J.A. Lambourne, and Stephen Serjeant. *An Introduction to Galaxies and Cosmology*. Cambridge University Press, 2nd edition edition, 2015.

Boris S. Kalita et al. A Rest-frame Near-IR Study of Clumps in Galaxies at $1 < z < 2$ Using JWST/NIRCam: Connection to Galaxy Bulges. *APJ*, 960(1):25, January 2024.

Robert C. Kennicutt. The global schmidt law in star-forming galaxies. *The Astrophysical Journal*, 498:541 – 552, 1998.

Robert C. Kennicutt et al. The Effects of Interactions on Spiral Galaxies. II. Disk Star Formation Rates. *AJ*, 93:1011, May 1987.

John Kormendy and Luis C. Ho. Coevolution (or not) of supermassive black holes and host galaxies. *Annual Review of Astronomy and Astrophysics*, 51(1):511–653, 2013.

John Kormendy and Douglas Richstone. Inward Bound—The Search For Supermassive Black Holes In Galactic Nuclei. *ARAA*, 33:581, January 1995.

Richard G. Kron. Photometry of a complete sample of faint galaxies. *The Astrophysical Journal Supplement Series*, 1980.

Guillaume Mahler et al. Relics: Strong lensing analysis of macs j0417.5–1154 and predictions for observing the magnified high-redshift universe with jwst. *The Astrophysical Journal*, 873(1):96, mar 2019.

Nir Mandelker, Avishai Dekel, Daniel Ceverino, Dylan Tweed, Christopher E. Moody, and Joel Primack. The population of giant clumps in simulated high-z galaxies: in situ and ex situ migration and survival. *Monthly Notices of the Royal Astronomical Society*, 443(4):3675–3702, August 2014.

Nicholas S. Martis et al. Modelling and Subtracting Diffuse Cluster Light in JWST Images: A Relation between the Spatial Distribution of Globular Clusters, Dwarf Galaxies, and Intracluster Light in the Lensing Cluster SMACS 0723. *arXiv e-prints*, page arXiv:2401.01945, January 2024.

Jasleen Matharu et al. A first look at spatially resolved balmer decrements at 1.0 lt; z lt; 2.4 from jwst niriss slitless spectroscopy. *The Astrophysical Journal Letters*, 949(1):L11, may 2023.

E. Merlin et al. Red and dead CANDELS: massive passive galaxies at the dawn of the Universe. , 490(3):3309–3328, December 2019.

Matteo Messa et al. Multiply lensed star forming clumps in the a521-sys1 galaxy at redshift 1. *Monthly Notices of the Royal Astronomical Society*, 2022.

Ekta A. Shah et al. Investigating the effect of galaxy interactions on star formation at 0.5 lt; z lt; 3.0. *The Astrophysical Journal*, 940(1):4, November 2022.

Iskra Strateva et al. Color separation of galaxy types in the sloan digital sky survey imaging data. *The Astronomical Journal*, 122(4):1861, oct 2001.

Pieter G. van Dokkum, Gabriel Brammer, et al. First results from the 3d-hst survey: The striking diversity of massive galaxies at z gt; 1. *The Astrophysical Journal Letters*, 743(1):L15, Nov 2011.

Devin Williams, Marcin Sawicki, Ivana Damjanov, and Harrison Souchereau. Investigating galaxy assembly through the buildup of stellar haloes since z = 1.1. *In preparation*, 2024.

Chris J. Willott, René Doyon, et al. The near-infrared imager and slitless spectrograph for the james webb space telescope. ii. wide field slitless spectroscopy. *Publications of the Astronomical Society of the Pacific*, 2022.

Deborah Freedman Woods and Margaret J. Geller. Minor galaxy interactions: Star formation rates and galaxy properties. *The Astronomical Journal*, 134(2):527, jun 2007.